# Rotation Curve of the Milky Way and the Phase-Space Structure of its Dark Matter Halo: Implications for Direct Detection of Weakly Interacting Massive Particle candidates of Dark Matter

By

SOUMINI CHAUDHURY

Enrolment No. : PHYS05200704003

Saha Institute of Nuclear Physics, Kolkata

*A thesis submitted to the*

*Board of Studies in Physical Sciences*

*In partial fulfillment of requirements*

*for the Degree of*

DOCTOR OF PHILOSOPHY

*of*

HOMI BHABHA NATIONAL INSTITUTE

August, 2014

# STATEMENT BY AUTHOR



**SOUMINI CHAUDHURY**

# DECLARATION

I, hereby declare that the investigation presented in the thesis has been carried out by me. The work is original and has not been submitted earlier as a whole or in part for a degree / diploma at this or any other Institution / University.

**SOUMINI CHAUDHURY**

# LIST OF PUBLICATIONS

1. **Critical properties and stability of stationary solutions in multi-transonic pseudo - schwarzschild accretion.*****

   Soumini Chaudhury, Arnab Kumar Ray and Tapas Kumar Das

   *Monthly Notices of the Royal Astronomical Society*, **2006**, *373*, 146-156

2. **Direct Detection of WIMPs: Implications of a self-consistent truncated Isothermal model of the Milky Ways Dark Matter halo.***

   Soumini Chaudhury, Pijushpani Bhattacharjee and Ramanath Cowsik

   *Journal of Cosmology and Astroparticle Physics*, **2010**, *09*, 020

3. **Deriving the velocity distribution of Galactic dark matter particles from the rotation curve data.*****

   Pijushpani Bhattacharjee, Soumini Chaudhury, Susmita Kundu and Subhabrata Majumdar

   *Physical Review D*, **2013**, *87*, 083525

4. **Rotation Curve of the Milky Way out to $\sim$ 200 kpc.****

   Pijushpani Bhattacharjee, Soumini Chaudhury and Susmita Kundu

   *The Astrophysical Journal*, **2014**, *785*, 63

5. **Local Dark Matter Density in the Light of Rotation Curve Data of Our Galaxy.***

Pijushpani Bhattacharjee, Soumini Chaudhury and Susmita Kundu

Draft Under Preparation.

6. **Dark Matter velocity anisotropy in our Galaxy from Rotation Curve data.***

Soumini Chaudhury and Pijushpani Bhattacharjee

Draft Under Preparation.

---

* :- **Included in this thesis.**

** :- **Partially included in this thesis.**

*** :- **Not included in this thesis.**

Journal References are in order: Journal name, **Year**, Volume, Starting Page Number

**SOUMINI CHAUDHURY**

*To my loved ones..*

# ACKNOWLEDGEMENTS

I take this opportunity to express my utmost gratitude to my advisor Prof. Pijushpani Bhattacharjee for his overall guidance and encouragement throughout my tenure in Saha Institute Of Nuclear Physics (SINP), Kolkata. He has inspired my way of independent thinking and his attitude towards academia has been of great influence to me as a whole. I am grateful to him for allowing me the freedom of working hours and being positive and persistent throughout.

My heartfelt thanks to fellow colleague Susmita for her invaluable academic as well as emotional help all through my tenure. This journey would not been so enriching and fulfilling without our academic discussions, short outings, traveling experiences - the memories of which I will continue to cherish throughout my life.

I consider myself truly blessed to have such a nice association of fellow students, faculties and administrative staffs at SINP. I am thankful to Prof. Milan Sanyal for granting the approval and funds to attend various national and international events. I thank Prof. Palash B. Pal for introducing me to LaTex without which writing this thesis would have been difficult. I am grateful to Prof. Rupak Mahapatra for providing me an invaluable opportunity for a summer internship at Texas A & M university, USA to gather the experience of working in a high-tech laboratory facility. I extend my thanks to International Centre for Theoretical Physics, Trieste, Italy for several travel and hospitality grants, Prof. Subir Sarkar to make an unforgettable visit to Oxford University possible, Gran Sasso Underground facility in Italy for hosting my laboratory visit, Korean Institute for Advanced Studies in Seoul for providing me with travel grant and hospitality for attending 'Particle Physics and Cosmology, 2012'. I am thankful to Prof. Tapas K. Das for being always there as my philosopher and guide. I am obliged and grateful to the SINP housing facility, my neighbors, supporting staffs, security, canteen cooks and transport persons for their sincere cooperation for contributing to a warm and yet spacious environment for me.

Looking back, I will ever be obliged to my University and School teachers for motivating me to pursue academics as a career. I feel blessed to have come across friends like Satarupa, Soumi, Anindya, Sarbani, Shreyoshi in different stages of my career. Thanks to my childhood friends, Poulomi, Ritobrata, Anumita, Salma and Debika, for being always there to lean upon and to confide in any sort of crisis.

Finally, it's my parents' and parent-in-laws' encouragement and passion that has driven me althrough. My husband and sister's role as my emotional anchor to boost my moral has kept me going through the tenure. I take this opportunity to express my love and respect for all of them and thank them for keeping faith in me.

*There is no wealth like knowledge,*

*and*

*no poverty like ignorance.*

*- Gautama Buddha*

# Contents

# SYNOPSIS

A large number of astronomical observations indicate that more than 25 % of the energy budget of the universe exists in the form of non-luminous gravitating material called Dark Matter (DM). Luminous matter in the form of stars, galaxies, and clusters accounts for $< 5\%$, and some unknown form of energy often called Dark Energy, responsible for the present day acceleration of the universe, constitutes the remaining $\sim 70$ % of the energy content of our universe [1]. The DM thus contributes to more than 80 % of the total gravitating mass in the universe. DM is present on mass scales ranging from those of dwarf spheroidals to the largest superclusters. In large spiral galaxies, such as our own Milky Way, the most compelling evidence for the presence of DM comes from the behavior of their rotation curve (RC), i.e., the circular velocity of a test particle as a function of the galactocentric distance. The observed "flat" RC of spiral galaxies out to distance of several tens of kpc from the galactic center can be explained naturally under the hypothesis that the luminous matter component is embedded in a roughly spherical, DM halo. However, the composition, the extents and phase space characteristics of the such halos of galaxies are not known with certainty.

Currently the most favored candidate for the DM belongs to a class of particles known as Weakly Interacting Massive Particles (WIMPs) that are predicted in many beyond-Standard-Model theories like those involving supersymmetry and large extra dimensions. WIMPs in the mass range $\sim$ few GeV to few hundreds of TeV can naturally account for the DM cosmological relic density [2]. Several experiments worldwide are currently trying to detect these hypothetical WIMPs, thought to constitute the dark halo of our Galaxy. *Direct detection* (DD) search experiments like DAMA, COGENT, CRESST, XENON, CDMS [3] and so on search for nuclear recoil events due to scattering of WIMPs off nuclei of suitably chosen detector materials in low background underground facilities. The WIMPs are also being searched for indirectly through detection of their self-annihilation products like antiprotons, gamma rays, positrons, neutrinos etc. [4]. Such annihilations can happen in likely high WIMP density regions such as in the core of the sun, Galactic centre, dwarf spheroidal galaxies and so on. In addition there are accelerator searches trying to detect missing momentum and energy attributable to WIMPs produced in collider experiments like LHC [5]. Although several projects have claimed tentative positive signals, no confirmed detection of WIMPs have so far been reported.

Two crucial astrophysical inputs required for a proper analysis of the results of any DD experiment are the local (i.e., the solar neighborhood) density of DM , $\rho_{DM,\odot}$, and the local velocity distribution function (VDF) of the DM particles, $f_{DM,\odot}(v)$, in the Galaxy. These are a priori unknown. Customarily, the Standard Halo Model (SHM) [6] is adopted as a description of the Galactic DM halo. However, this model suffers from several limitations as discussed in one of the chapters in this thesis. In this thesis, I study the phase space characteristics of the DM halo of our Galaxy with a view to providing a more realistic and physically acceptable description of the phase space distribution of the DM particles in the Galaxy and study their implications for the interpretation of the results of DD experiments. In doing this, I use the RC data for the Galaxy as the primary observational input for deriving the parameters of the possible phase space distribution function (PSDF) of the WIMP particles hypothesized to constitute the DM halo of the Galaxy. In particular, I study the effect of self-consistent gravitational influence of the visible matter (VM) which dominates the dynamics of the Galaxy within the solar circle, on the phase space structure of the DM halo. Since the RC plays a major role in my work described in this thesis, I also present our new results on the construction of the RC of the Galaxy and it's dependence on the Galactic Constants (GC), ($r_0$,$v_0$), i.e. the sun's distance from and circular rotation speed of the Local Standard of Rest around the Galactic center, respectively.

This thesis is arranged as follows. In **Chapter 1**, I present a broad overview of the evidences for DM and the arguments for WIMPs being a probable DM candidate. Also, I discuss the phenomenology of DD of DM, search strategies of different DD experiments, analysis methods etc. with emphasis on the role of astrophysical inputs and prevailing uncertainties thereof [2, 6, 7, 8].

In **Chapter 2**, I describe the conventionally used SHM specified by a velocity dispersion of 270 $\mathrm{km\,s^{-1}}$ and $\rho_{DM,\odot}$ set at $\sim 0.3$ $\mathrm{GeV\,cm^{-3}}$. The implications of the SHM for DD experiments considering both WIMP-nucleon elastic and inelastic scattering cases are also discussed here. In the SHM, the PSDF of the WIMPs is described by the Isothermal Distribution Function (IDF) [9], which is a stationary solution of the collisionless Boltzmann equation. This IDF is a function of energy ($\mathcal{E}$) only which implies that the velocity space is isotropic. The VDF of this model follows a standard Maxwellian distribution, truncated at some chosen value of the local escape speed for practical purposes. I determine the parameters of the IDF by fitting the theoretically calculated RC with an observed set of RC data [10] for our Galaxy. In this exercise, I include the gravitational influence of the observed VM [11] on the DM in a self-consistent manner and find that the resulting additional gravitational potential of the VM - neglected in earlier studies - can support significantly higher velocity dispersions than usually considered in the

DM-only SHM fits. I then study the implications of these results for several DD experiments and compare them with those obtained using the SHM.

In **Chapter 3**, I discuss the shortcomings of the SHM and motivate the study of a more physically acceptable PSDF of a finite size DM halo of the Galaxy. In particular, I use the King model [9], a PSDF with isotropic VDF describing a finite extent and spherically symmetric cored system of collisionless particles. The relevant parameters of the model are determined by fitting the theoretically predicted RC profile with the available RC data set for the Galaxy [10, 12], including self-consistent gravitational coupling between the VM and DM components [8]. Unlike in SHM, the isotropic VDF of the DM particles in this model deviates significantly from the Maxwellian form as indicated by recent simulations as well [13], and has a natural cut-off at a finite velocity determined by the model itself. Interestingly, it is found that the VM "pulls in" the DM towards the center as well as towards the disk of the Galaxy, thereby increasing the DM densities in those regions compared to the densities that one would obtain in absence of the VM. I then discuss the implications of the best fit King model for the results of DD experiments for the cases of both spin-independent and spin-dependent WIMP-nucleon scattering. These results [8] are shown to strengthen the possibility of low-mass ($\leq 10$ GeV) WIMPs being a candidate for DM, as indicated by several recent experiments.

The RC plays a major role - indeed the main observational anchor - in my approach to the problem of deriving information on the phase space structure of the DM halo of the Galaxy. It is a direct observational probe of the total gravitational potential and hence mass distribution in the Galaxy. In **Chapter 4**, I present the results of my work pertaining to constructing the RC of the Galaxy from a Galactocentric distance of 0.2 kpc up to about 20 kpc without assuming any theoretical models of the mass components of the Galaxy. The RC of the Galaxy, is, of course, not a directly measured object and has to be derived from the kinematical as well as positional data on a variety of tracer objects moving in the gravitational field of the Galaxy. I study the sensitivity of the RC on the choice of GC set. It is found that the RC of the Galaxy in the disk region depends significantly on the value of GC adopted.

**Chapter 5** deals with a study of the sensitivity of $\rho_{DM,\odot}$ on the GC set chosen for constructing the RC data as discussed in Chapter 4. I perform the analysis for the Einasto profile, the DM density form, which provides a good description of the density profiles obtained by cosmological simulations [14]. I obtained the most likely DM and VM parameters and their 68 % CL bounds using an extensive Markov Chain Monte Carlo analysis, using our RC data for three separate GC sets. It is seen that the best fit value of $\rho_{DM,\odot}$ depends significantly on the value of $v_0$ used in the analysis. In particular, $\rho_{DM,\odot}$ decreases from $\sim 0.56\ \mathrm{GeV\,cm^{-3}}$ to $\sim 0.19\ \mathrm{GeV\,cm^{-3}}$ as $v_0$ is varied from $244\ \mathrm{km\,s^{-1}}$ to $200\ \mathrm{km\,s^{-1}}$. This is shown to be the case for other assumed DM profiles as well.

In **Chapter 6**, I study the possible nature of the full phase space structure of the DM halo corresponding to the best-fit Einasto DM density profile described in the previous Chapter. In doing this, I considered the possible anisotropic VDF of DM particles, as indicated by recent high resolution cosmological simulations [15]. Unlike in Chapter 3, here I adopt an alternative approach to constructing the PSDF.

Specifically, I “invert” the best-fit Einasto density profile discussed in Chapter 5 to obtain the anisotropic VDF of the DM particles by the Osipkov Merritt (OM) method [9, 16] by including the gravitational influence of the VM on the DM particles in a self-consistent manner. The resulting VDFs for the three velocity components are seen to be of non-Maxwellian nature. I also determine the anisotropy radius and the consequent radial profile of the velocity anisotropy parameter, $\beta(r)$, of the DM particles in the halo. I also discuss how the inclusion of the gravitational influence of the VM significantly changes the VDF for all the velocity components.

Finally, **Chapter 7** contains a summary of the main results presented in this thesis and concludes by mentioning future works in this direction.

# Bibliography


[1] N. Jarosik, et al. [WMAP Collaboration], ApJS. **192** (2011) 14;
P. A. R. Ade, et al. [Planck Collaboration], Astron. Astrophys. **571** (2014) A16

[2] G. Jungman, M. Kamionkowski, & K. Griest, Phys. Rep. **267** (1996) 195;
G. Bertone, D. Hooper & Joseph Silk, Phys. Rep. **405** (2005) 279;
L. E. Strigari, Phys. Rep. **531** (2013) 1

[3] R. Bernabei, et al. [DAMA Collaboration and LIBRA Collaboration], Eur. Phys. J. C **67** (2010) 39;
C. E. Aalseth, et al. [CoGeNT Collaboration], PRL **106** (2011) 131301;
G. Angloher, et al. [CRESST Collaboration] , Eur. Phys. J. C **72** (2012) 1971;
E. Aprile, et al. [XENON100 Collaboration], PRL **109** (2012) 181301;
R. Agnese, et al. [CDMS-II Collaboration], PRL **111** (2013) 251301

[4] O. Adriani, et al. [PAMELA Collaboration], PRL **105** (2010) 121101;
M. Ackermann, et al. [Fermi Collaboration], PRD **88** (2013) 082002;
M. Aguilar, et al. [AMS Collaboration], PRL **110** (2013) 141102;
J. Hosaka, et al., PRD **73** (2006) 112001

[5] Mads T. Frandsen, et al., JHEP **1207** (2012) 123;
G. Aad, et al., JHEP. **1304** (2013) 075

[6] For a review see: A. M. Green, Mod. Phys. Lett. **A27** (2012) 1230004

[7] S. Yellin, **arXiv**:0709.2701;

J. D. Lewin & R. F. Smith, Astropart. Phys. **6** (1996) 87;

F. Petriello & K. M. Zurek, JHEP **09** (2008) 047;

C. Savage, et al., JCAP **04** (2009) 010

[8] S. Chaudhury, P. Bhattacharjee & R. Cowsik, JCAP. **09** (2010) 020

[9] J. Binney and S. Tremaine, Galactic Dynamics, 2nd Edition (Princeton University Press, Princeton, 2008).

[10] M. Honma & Y. Sofue, PASJ **49** (1997) 453

[11] J. Caldwell & J. Ostriker, ApJ **251** (1981) 61;

K. Kuijken & G. Gilmore, MNRAS **239** (1989) 571; **239** (1989) 605; **239** (1989) 651;

Astrophys. J. Lett. **367** (1991) L9

[12] Xue, X. X., et al., ApJ. **684** (2008) 1143

[13] M. Vogelsberger, et al., MNRAS **395** (2009) 797;

M. Kuhlen, et al., JCAP. **02** (2010) 030

[14] J. F. Navarro, et al., MNRAS **349** (2004) 1039;

A. W. Graham, et. al., Astron. J. **132** (2006) 2701

[15] F. S. Ling, E. Nezri, E. Athanassoula, & R. Teyssier, JCAP. **02** (2010) 012

[16] L. P. Osipkov, Pisma Astron. Zh. **5** (1979) 77;

L. P. Osipkov, Soviet Astron. Lett. **5** (1979) 42;

D. Merritt, Astron. J. **90** (1985) 1027

# List of Figures

# List of Tables

# Chapter 1

# Introduction

## 1.1 Overview

A variety of astronomical and cosmological observations involving measurements of the anisotropies of the cosmic microwave background radiation [1], weak and strong gravitational lensing [2], inner dynamics of dwarf spheroidal galaxies [3] rotation curves (RC) of large spiral galaxies [4]-[8], merger of Bullet cluster [9], and so forth (see [10] for a review), indicate that more than 80 % of the total gravitating matter density in the Universe is attributable to some non-baryonic and stable (with life time at least as large as the age of the Universe) form of matter, which emits no detectable electromagnetic radiation of any kind, and is, therefore, called 'Dark Matter' (DM). The baryonic matter in the form of stars and gas in galaxies, clusters etc. constitutes less than 20 % of the gravitating matter content of the Universe. In terms of total energy density, the baryonic matter constitutes less than 5 % whereas the non-baryonic DM constitutes $\sim$ 26 % to the total energy density in the Universe. The rest, $\sim$ 69 %, constituting the dominant component in terms of energy density exists in a form called 'Dark Energy' (DE) that seems to exhibit "repulsive gravity" and is thought to be responsible for the observed accelerated expansion of the Universe today [1]. See Figure 1.1 for a pie chart representation of the energy density distribution of various components of the Universe, as it stands today, reported by Planck satellite mission [1].

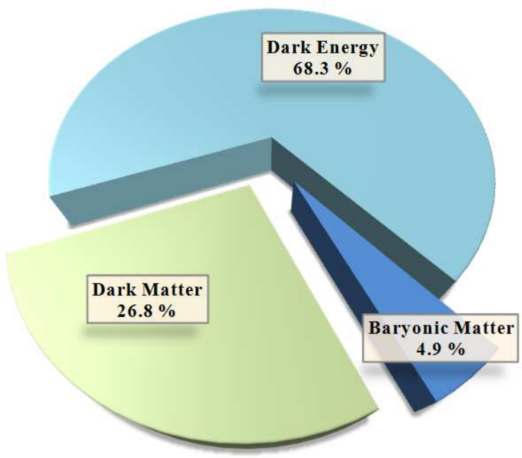


Figure 1.1: Pie chart for energy density budget of the different components of the Universe [1].

The nature and composition of both DE and DM are currently unknown. In this thesis, we will not discuss DE any further, but rather focus on DM.

Currently, one of the most favored candidates for DM are the so - called Weakly Interacting Massive Particles or WIMPs (denoted by $\chi$ henceforth) with masses which may lie anywhere between a few GeV to several hundreds of TeV [11, 12]. Such particles naturally arise in well-motivated extensions of the Standard Model (SM), such as those involving supersymmetry (SUSY) [13] and/or large extra dimensions [14]. The attractive feature of the WIMPs is that, owing to their weak interactions, they can "freeze out" sufficiently early in the Universe so that their relic abundance in the present epoch can be sufficient to naturally explain the measured cosmological density of DM in the Universe - a fact well known as the 'WIMP Miracle' [15, 16]. For a comprehensive review on possible candidates of DM, one can refer to [10, 17], for example.

On the scale of galaxies, such as our Galaxy (the Milky Way), the observed non-declining nature of the RC beyond the visible edge can be naturally explained under the hypothesis that the observed visible matter (VM) of the galaxies are embedded in roughly spherical halos of DM (schematically represented in Figure 1.2), extending to large galactocentric distances (perhaps to few hundreds of kpc). However, the true extents and phase space characteristics of the DM halos around galaxies are still unknown.

An alternative explanation of the nature of the rotation curve was first suggested by M. Milgrom in 1983 [18] and subsequently studied in further detail by various authors. This involves modifying Newtonian gravitational dynamics to interpret observations without introducing any invisible dark matter. The resulting theory is called Modified Newtonian Dynamics (MOND). It has also been suggested as an alternative to DM on larger scales. However, there are several issues that remain to be understood. See [19] for a comprehensive review and the references therein. In this thesis we will not discuss MOND any further and rather concentrate on the DM interpretation of RC behavior in our Galaxy.

In 1985, Goodman and Witten [20] pointed out that the WIMPs, by virtue of their weak interaction with SM particles, may scatter from nuclei of ordinary VM, thus


Figure 1.2: A schematic diagram of visible matter for a typical spiral galaxy (comprising of a central bulge, disk, and stellar halo) embedded in a dark matter halo.

offering a way of directly detecting the WIMPs in a laboratory set up. Following this suggestion, several experiments worldwide are currently engaged in attempts to directly detect the WIMPs through observing signals like scintillation, phonon, charge deposition etc. attributable to nuclear recoil events arising from WIMP scatterings off nuclei of suitably chosen detector materials. To avoid cosmic ray backgrounds, these experiments are typically performed in deep underground laboratories. Attempts are also being made to detect WIMPs indirectly through their self annihilation products like antiprotons, positrons, gamma rays, neutrinos etc. likely to originate from high DM density regions such as in the core of the Sun, Galactic center, dwarf spheroidal galaxies, and so on. Experiments like PAMELA, FERMI, AMS, Super-Kamionkande, Icecube etc. are some promising projects in this category [21]. In addition, there are accelerator searches, looking for missing momentum/energy attributable to WIMPs produced in collider experiments like LHC [22]. Till date, though some experiments have reported claims of detection, no confirmed detection has been reported so far; see, e.g., Ref. [23] for an recent review. Henceforth, in this thesis, we shall concentrate only on DD of WIMPs.

Two crucial astrophysical inputs, namely, the local (i.e., the Solar neighborhood) density of DM, $\rho_{\rm DM,\odot}$, and the local velocity distribution function (VDF) of the DM particles (assumed to be WIMPs throughout this thesis) populating the Galactic halo, are required for the analysis and interpretation of the results of the DD experiments for WIMPs. There is currently considerable amount of uncertainty in these astrophysical quantities. In this thesis, we shall attempt to derive the value of $\rho_{\rm DM,\odot}$ as well as the nature of local VDF from observational data pertaining to our Galaxy.

There have been several attempts to derive the value of $\rho_{\rm DM,\odot}$ [24]-[34] based on varied observational data, with values as small as close to zero to as high as 1.32 $\mathrm{GeV\,cm^{-3}}$ being quoted in literature. In contrast, not much knowledge directly based on observational data is available on the likely form of VDF of the DM particles constituting the Galactic halo. It is a standard practice to assume the VDF to be of Maxwell Boltzmann form. However, some recent cosmological simulations [35]-[39] and proposed forms [40, 41, 42] seem to indicate significant departure of the VDF from typical Maxwellian nature. In addition, some of them (for example, [38, 40]) even indicate an anisotropic behavior of the VDF.

In this thesis, we shall derive the values for $\rho_{\rm DM,\odot}$ and the possible forms of VDF of the DM particles populating the Galactic halo using the observational data corresponding to the Milky Way itself. We attempt to throw light on the possible forms of the phase space distribution function (PSDF), $f(\mathbf{x}(t), \mathbf{v}(t))$, as a description of our Galactic DM halo. Owing to their weak interaction, the WIMPs are assumed to satisfy the collisionless Boltzmann equation (CBE) [43], the stationary solutions of which can represent possible PSDFs for the DM constituting the Galactic halo. Customarily, the 'standard halo' model (SHM) [44]-[47], which is based on the 'isothermal sphere' (IS) solution of the steady state CBE, is widely used in the analysis of DD experiment results. The SHM is defined by a particular choice of $\rho_{\mathrm{DM},\odot} \simeq 0.3\ \mathrm{GeV\,cm^{-3}}$ and VDF as a Maxwellian distribution with velocity dispersion $\langle v^2 \rangle^{1/2} \simeq 270\ \mathrm{km\,s^{-1}}$.

However, the IS model of the Galactic halo (adopted in SHM) suffers from some serious shortcomings, namely, it has a divergent total mass as the halo radius $r \to \infty$ and hence is unsuitable for representing a halo of a finite size and mass like our Milky Way. In addition, the significant gravitational influence of the VM on the spatial as well as velocity distribution of the DM particles, especially in the inner regions of the Galaxy, is not taken into account in the customarily adopted "isolated" SHM.

We shall therefore, consider self-consistent models of PSDF that are stationary solutions to CBE representing a DM halo of finite mass. Towards this end, we consider two approaches in constructing the models of the PSDF. In the first approach, we start with an ansatz for the PSDF for a finite sized halo of the Galaxy endowed with an isotropic VDF. We use the RC data of the Galaxy, which is the circular velocity of a test particle as a function of Galactic radius, as the primary observational input for deriving the parameters of the PSDF of the WIMP particles hypothesized to constitute the DM halo of the Galaxy and study their implications for the interpretation of the results of DD experiments. In doing this, we include the effect of the gravitational influence of the VM, which dominates the dynamics of the Galaxy within the Solar circle on the phase space structure of the DM halo in a self-consistent manner, using the formalism described in earlier works [48, 49]. In the second approach, we start with a density model defining the Galactic halo, motivated by the results of numerical simulations and determine the parameters of the model by fit to the RC of the Galaxy. Thereafter, we use the Osipkov-Merritt (OM) technique [50], a formalism which allows the determination of the PSDF characterized by an anisotropic VDF by "inverting" an assumed form of a spherically symmetric density profile. In this exercise, we again include the gravitational effect of VM on the PSDF of DM particles constituting our Galactic halo in a self-consistent manner.

In both of the above mentioned approaches, the RC of the Galaxy plays a central role in determining the parameters of the models. In this thesis, we also devote a chapter, where we discuss the construction of RC data particularly in the disk region and its dependence on Galactic Constants (GCs), $\left[\frac{R_0}{\mathrm{kpc}}, \frac{V_0}{\mathrm{km\,s^{-1}}}\right]$, where $R_0$ and $V_0$ are the distance of the Sun from the Galactic center and circular rotation speed of the local standard of rest frame around the Galactic center, respectively. We also study the implications of the RC data for determination of $\rho_{\mathrm{DM},\odot}$ and VDF of the DM particles constituting the Galactic halo, and thus determine the astrophysical inputs required for the analysis and interpretation of DD experiments.

The following section presents the organization of the rest of the thesis.

## 1.2 Layout of the Thesis

In the next chapter (**Chapter 2**), we begin with a brief introduction to DD search phenomenology. Then, we present a summary of the detection methods being used in currently operating detectors. We summarize the current status of different ongoing DD experiments running worldwide.

In **Chapter 3**, we describe the SHM and its fit to the RC data of the Galaxy. We also study the effect of the gravitational influence of the VM on DM and the resultant modification of SHM parameters in the context of an IS model for the Galactic DM halo. Finally, we study the implications of our results for the analysis of different DD experiments.

In **Chapter 4**, motivated by the shortcomings of the IS (describing an SHM), we adopt a PSDF namely the 'King' model or 'truncated isothermal' model [43] representing a finite sized DM halo of the Galaxy, which is a also steady state solution to CBE like IS model discussed earlier. The velocity distributions of this model is isotropic but of non-Maxwellian form unlike SHM and has a finite cut off self-consistently determined by the model itself. We fix the parameters of the model by fitting to the RC data of the Galaxy in a self-consistent manner considering the the gravitational influence of the underlying VM distribution. The gravitational effect of VM on the DM halo density profiles is explicitly demonstrated for this halo. Finally, with the values of the parameter set adopted to be those giving best fit to the RC data, we study the implications of the King model for the analysis of DD experiments. A comparison is drawn with the results obtained with SHM, for the sake of completeness.

In **Chapter 5**, we perform the exercise of constructing the RC of the Galaxy in the disk region considering a variety of disk tracers moving in the gravitational potential of our Galaxy, in a manner independent of any models for the VM or DM components of the Galaxy and study the sensitivity of the RC data on the assumed sets of GCs.

In **Chapter 6**, we attempt to derive the value of $\rho_{\mathrm{DM},\odot}$ using the RC data [8] of our Galaxy extending to large galactocentric distance of $\sim 200$ kpc and scaled to different GC sets. We consider various DM halo density models motivated by N-body simulations and determine the values of $\rho_{\mathrm{DM},\odot}$ and their dependence on the chosen GC set. We also derive the values for some physically relevant quantities like total mass, halo virial radius, maximum local velocity, etc., and present the best fit RC-, mass-, density-, and maximum velocity profiles for the various DM models considered.

In **Chapter 7**, we derive the PSDF of the DM halo of our Galaxy by using the OM formalism. The so obtained PSDF satisfies the steady state CBE and is also characterized by an anisotropic VDF. In doing this, we again include the gravitational effect of VM on the PSDF of DM particles constituting our Galactic halo in a self-consistent manner. The parameters of the DM (taken to be the Einasto density profile) as well as of the VM density profiles, have been determined by fit to the RC data of our Galaxy extending to $\sim 200$ kpc. We also calculate the normalized total, radial, and transverse VDF at different locations of the Galaxy. We discuss the effect of VM on the so obtained anisotropic velocity distribution and their variation with galactic radii. In addition, we also present a list of the best fit values of some of the most relevant physical quantities of interest associated with the Galaxy, like, mass within various radial distances, local values of escape velocity, circular velocity, velocity dispersion ($\langle v^2\rangle^{1/2}$), bounds on the anisotropy parameter $\beta(r) = [1 - \frac{\sigma_t^2(r)}{2\sigma_r^2(r)}]$ (based on the non-negativity condition of the PSDF) etc., where, $\sigma_t$ and $\sigma_r$ are the velocity dispersions in tangential and radial directions, respectively, with, $< v^2 >= \sigma_r^2 + \sigma_t^2$.

Finally, in **Chapter 8**, we summarize the main results of this thesis.

# Chapter 2

# Direct Detection of Dark Matter

---

In this chapter, first we will present a description of the phenomenology of direct detection (DD) of dark matter (DM). Thereafter, we will briefly review the process of detection of nuclear recoil signals in DD setup and mention the current status of several DD experiments searching for the Weakly Interacting Massive Particle (WIMP) candidates of DM.

## 2.1 Detection Phenomenology

The basic idea of DD for detecting the WIMP candidates constituting the Galactic DM halo is to look for nuclear recoil events due to scatterings of the Galactic WIMPs off nuclei of the detector material, as first suggested by Goodman and Witten in 1985 [20].

Let us consider a WIMP, $\chi$, of mass $m_\chi$ scattering elastically from a nucleus, N, of mass M. Since the typical velocity of a DM particle in the Galaxy is $\sim$ few 100 km s$^{-1}$, the scattering process can be treated as non-relativistic. Using energy and momentum conservation equations, it is easily seen that the nucleus receives a recoil kinetic energy,

$$E_R = q^2/(2M) = (\mu^2 u^2/M)(1 - \cos\theta^*), \tag{2.1}$$

where $\theta^*$ is the scattering angle in the center of momentum frame, $q$ is the momentum transferred to the recoiling nucleus, $\mu = m_\chi M/(m_\chi + M)$ is the WIMP-nucleus reduced mass and $u = |\mathbf{u}|$ is the speed of the WIMP relative to the nucleus assumed to be at rest on earth. The minimum WIMP speed that can produce a recoil energy $E_R$ of the nucleus is, therefore,

$$u_{\min}(E_R) = \left(\frac{ME_R}{2\mu^2}\right)^{1/2} . \tag{2.2}$$

It is also possible that the WIMPs may scatter inelastically, as $\chi N \to \chi_f N$, where $\chi_f$ is the DM particle after scattering. In this case, the minimum WIMP speed that can deposit a recoil energy $E_R$ to the nucleus is again obtained by considering mass-energy and momentum conservation equations, giving, in the non-relativistic limit,

$$u_{\min}(E_R) = \sqrt{\frac{1}{2ME_R}}\left(\frac{ME_R}{\mu} + \delta\right), \tag{2.3}$$

where $\delta \equiv m_{\chi_f} - m_\chi$ is the inelasticity parameter. It should be noted that $\delta$ may take both positive and negative values. For a given WIMP mass, nuclear mass and recoil energy, a chosen value of $\delta$ is allowed only if $u_{\min} \geq 0$. Note that Equation

(2.3) reduces to Equation (2.2) for $\delta = 0$. Figure 2.1 shows a schematic diagram of the scattering process.

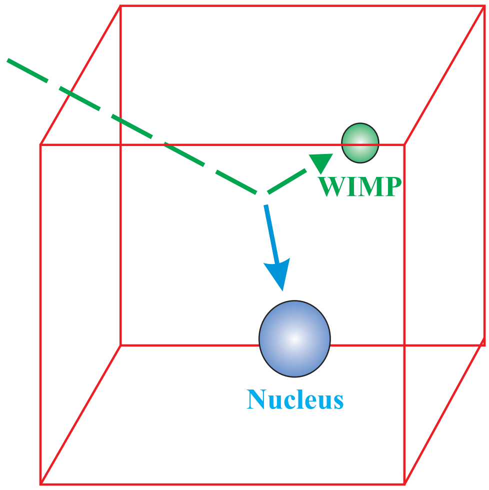


Figure 2.1: A schematic diagram of scattering of a Weakly Interacting Massive Particle (WIMP) from a target nucleus in a dark matter direct detection experiment.

The differential event rate per unit detector mass (typically measured in counts/day/kg/keV) can be written as [15, 51],

$$\frac{d\mathcal{R}}{dE_R}(E_R, t) = \frac{\sigma(q)}{2m_\chi \mu^2}\rho_\chi \xi(E_R, t)\,, \tag{2.4}$$

where $\rho_\chi \equiv \rho_{\rm DM,\odot}$ is the density of WIMPs in the Solar neighborhood, $\sigma(q)$ is the WIMP-nucleus effective interaction cross section, and

$$\xi(E_R, t) = \int_{u > u_{\rm min}(E_R)} d^3\mathbf{u} \frac{\tilde{f}(\mathbf{u}, t)}{u}\,. \tag{2.5}$$

Here $\tilde{f}(\mathbf{u}, t)$ is the normalized time-dependent velocity distribution function (VDF) of the WIMPs in the Solar neighborhood *relative to the detector at rest on earth.* Since the interaction is weak, the expected event rates are low and typically $\lesssim 0.1$ events per day per kg of detector material. The recoil energy deposited by the non-relativistic WIMPs can be as low as few tens to hundreds of keV, which requires highly precise sensors with low energy threshold to detect such recoil events. The right hand side of Equation (2.4) can be clearly factored into two parts: the factor $\frac{\sigma(q)}{2m_\chi\mu^2}$ carries all the particle physics information about WIMPs and detector nuclei, whereas, the factor $\rho_\chi\xi(E_R,t)$ carries the astrophysical information of the Galactic DM halo considered for the analysis.

Given a steady state phase space distribution function (PSDF) of the DM particles, $f(\mathbf{x},\mathbf{v})$, in the rest frame of the halo, the time dependence of the VDF, $\tilde{f}(\mathbf{u},t)$, arises from the motion of the earth with respect to the Galactic rest frame. The two distribution functions are simply related as,

$$\tilde{f}(\mathbf{u},t) = \frac{1}{\rho_\chi} f\left(\mathbf{x}=\mathbf{x}_\odot, \mathbf{v}=\mathbf{u}+\mathbf{v}_{\mathrm{E}}(t)\right) , \tag{2.6}$$

where $\mathbf{x}_\odot$ represents the Sun's position ($R=R_0, z=0$) and $\mathbf{v}_{\mathrm{E}}(t)$ is the earth's velocity vector *in the Galaxy's rest frame*. If the DF $f(\mathbf{x},\mathbf{v})$ vanishes or is truncated at some finite speed $v=v_{\max}(\mathbf{x})$, then using Equation (2.6), Equation (2.5) can be explicitly written as,

$$\xi(E_R,t) = \frac{2\pi}{\rho_{\mathrm{DM},\odot}} \int_{-1}^{1} d(\cos\theta)\ \Theta\left(u_{\max}-u_{\min}\right) \int_{u_{\min}(E_R)}^{u_{\max}(\cos\theta)} u f\left(\mathbf{x}=\mathbf{x}_\odot, \mathbf{v}=\mathbf{u}+\mathbf{v}_{\mathrm{E}}(t)\right) du. \tag{2.7}$$

Here, $u_{\max}$ is the positive root of the equation,

$$v_{\max}^2 = u_{\max}^2 + v_{\mathrm{E}}^2 + 2u_{\max}v_{\mathrm{E}}\cos\theta\,, \tag{2.8}$$

and is given by,

$$u_{\max} = -v_{\mathrm{E}}\cos\theta + \sqrt{v_{\max}^2 - v_{\mathrm{E}}^2\sin^2\theta}, \tag{2.9}$$

with $v_{\max} \equiv v_{\max}(\mathbf{x}_{\odot})$, and $v_{\rm E} = |\mathbf{v}_{\rm E}|$ given by [52]

$$v_{\rm E}(t) = V_{c,\odot} + v_{\rm E,orb} \cos\gamma \cos\left[\omega(t - t_0)\right]. \tag{2.10}$$

In Equation (2.10), $V_{c,\odot} \approx V_0 + v_{pec}$, is the magnitude of the dominant component of Sun's total velocity vector, with $V_0$ being the circular velocity of the local standard of rest (LSR) around the Galactic center and $v_{pec}$ being the component of Sun's "peculiar" velocity in the LSR rest frame along the direction of $V_0$. Here, $v_{\rm E,orb} \approx 30\,{\rm km\,s^{-1}}$ is the average orbital speed of the earth around the Sun and $\gamma \approx 60^\circ$ is the angle subtended by earth's orbital plane with the Galactic plane (see Figure 2.2). Here, $\omega = 2\pi/365$ and $t_0 = 152.5$, corresponding to 2nd June when the earth's speed with respect to the Galactic rest frame is maximum, $t$ being counted in days. The periodic variation of $v_{\rm E}$ in Equation (2.10) is expected to give rise to an annual modulation of the event rates in a DD experiment. Such an annual modulation has been claimed to have been detected by DAMA [53] and CoGeNT [54] collaborations, although, other non-DM explanations of the claimed signal exist in literature as well [55]. For the purpose of analysis of DD experiments in the following two chapters, the IAU recommended values of the Galactic Constants (defined in Chapter 1), $\left[\frac{R_0}{\rm kpc}, \frac{V_0}{\rm km\,s^{-1}}\right] = [8.5,\, 220]$, have been adopted and $v_{pec}$ has been set equal to $12\,{\rm km\,s^{-1}}$ [56].

Using Equation (2.2) and (2.10), it can be deduced that for a given recoil energy detection threshold, $E_{\rm th}$, of an experiment, there is a lowest WIMP mass, $m_{\chi,\rm min}$, that can be probed by the experiment is given by,

$$m_{\chi,\rm min} = M\left[\left(2M(v_{\max} + v_{\rm E}(t=t_0))^2/E_{\rm th}\right)^{1/2} - 1\right]^{-1}. \tag{2.11}$$

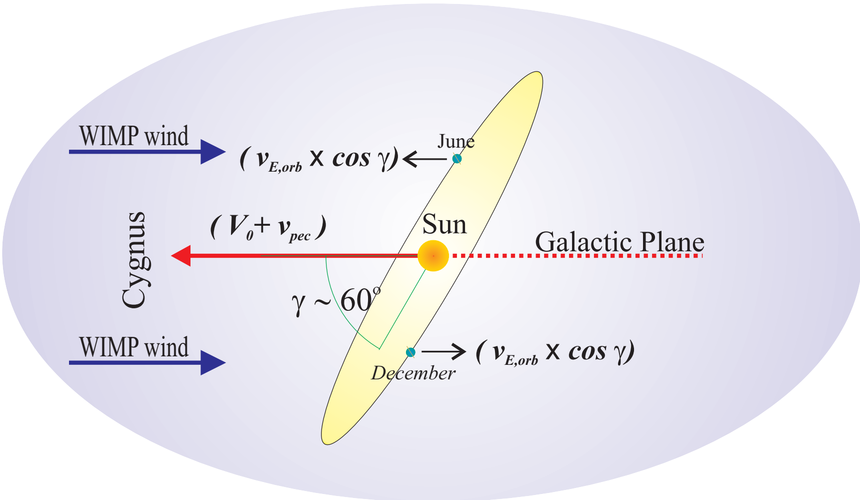


Figure 2.2: A schematic diagram of motion of earth around Sun in the Galactic rest frame.

For detectors composed of more than one kind of elements, the total differential nuclear recoil event rate is,

$$\left(\frac{d\mathcal{R}}{dE_R}\right)_{\rm tot} = \sum_i f_i \left(\frac{d\mathcal{R}}{dE_R}\right)_i , \tag{2.12}$$

where $f_i$ is the mass fraction of, and $\left(\frac{d\mathcal{R}}{dE_R}\right)_i$ the differential event rate [Equation (2.4)] for, the nuclear species $i$.

The number of nuclear recoil events in a recoil energy range between $E_R^1$ and $E_R^2$ is

$$N_R(E_R^1, E_R^2) = \sum_i \int_{E_R^1}^{E_R^2} dE_R \left(\frac{d\mathcal{R}}{dE_R}\right)_i \mathcal{K}_i(E_R) , \tag{2.13}$$

where $\mathcal{K}_i = \mathcal{M}_i T \epsilon(E_R)$ is the total exposure of the detector, $\mathcal{M}_i$ being the total fiducial mass of the species $i$ in the detector, $T$ the total effective exposure time, and $\epsilon(E_R)$ the energy-dependent detector efficiency.

The WIMP-nucleus interaction cross-section, $\sigma(q)$, can be derived from first principles given a particle physics model of the WIMPs and their fundamental interactions with the quarks constituting the nucleons in the nucleus. It has been shown [15] that in the non-relativistic limit, the WIMP-nucleus total effective scattering cross section, $\sigma(q)$, can be written as a sum of two contributions arising from spin-independent and spin-dependent effective couplings of the WIMP to the target nucleus,

$$\sigma(q) = \sigma^{\rm SI}(q) + \sigma^{\rm SD}(q)\,. \qquad (2.14)$$

*Spin-independent* (SI) (or *Coherent*) Scattering : In this case the WIMP interacts coherently with the nucleus as a whole. The $\sigma^{\rm SI}$ is generally written as [15, 51],

$$\sigma^{\rm SI}(q) = \sigma_0^{\rm SI}|F(q)|^2, \qquad (2.15)$$

where $\sigma_0^{\rm SI}$ is the "zero-momentum" WIMP-nucleus scattering cross section and F(q) (normalized to F(0)=1) is a momentum dependent form factor that takes into account the loss of coherence due to the finite size of the nucleus. The loss of coherence results in a suppression of the scattering cross-section at large momentum transfers.

We use the conventional Helm form for the nuclear form factor [57] :

$$F(q) = 3\frac{j_1(qr_0)}{qr_0}e^{-(qs)^2/2}, \qquad (2.16)$$

where $qr_0$ or $qs$ are scaled by $\hbar$, hence are dimensionless, $j_1(z) = \frac{\sin(z)}{z^2} - \frac{\cos(z)}{z}$ is the spherical Bessel function of order 1, $s = 0.9\,$fm is the nuclear skin thickness, and $r_0 = 1.14A^{1/3}$ fm is the effective nuclear radius [51].

The zero-momentum cross-section, $\sigma_0^{\rm SI}$, can be written, in the non-relativistic limit as [15],

$$\sigma_0^{\rm SI}(q) = \left[f_p Z + f_n(A-Z)\right]^2 \frac{4\mu^2}{\pi} \tag{2.17}$$

where A and Z are the mass number and atomic number of the target nucleus respectively. Here $f_n$ and $f_p$ are the WIMP couplings to protons and neutrons, respectively. Since many types of target nuclei may be involved in detection experiments, it is convenient to express the WIMP-nucleus cross-section in terms of WIMP-proton or WIMP-neutron cross-section. In most instances, $f_n \approx f_p$, so one can write the WIMP-nucleon cross-section as

$$\sigma_0^{\rm SI} = \left(\frac{\mu}{\mu_{\chi-nucleon}}\right)^2 A^2 \sigma^{\rm SI}_{\chi-nucleon}, \tag{2.18}$$

where $\mu_{\chi-nucleon}$ is the WIMP-nucleon reduced mass. The coherent nature of the interaction is evident since $\sigma_0^{\rm SI}$ scales with the square of the atomic mass number $A$ (number of protons plus neutrons) of the nucleus. Hence, massive nuclei are appropriate targets for SI scatterings.

*Spin-dependent* (SD) Scattering : In this case the WIMP couples to the total angular momentum, $J$, of the nucleus which has contributions from the spins of the individual protons and neutrons within the nucleus. The shell model of the nucleus provides a framework for calculating $J$ from proton and nuclear spins, although it can be calculated in other nuclear models as well such as the single particle model, odd group model etc. [15, 51]. In the non relativistic limit, the $\sigma^{\rm SD}(q)$ can be written as [58]

$$\sigma^{\rm SD}(q) = \sigma_0^{\rm SD}\frac{S(q)}{S(0)}, \tag{2.19}$$

with

$$\sigma_0^{\rm SD} = 32 G_F^2 \frac{\mu^2 \Lambda^2 J(J+1)]}{\pi}, \tag{2.20}$$

where $G_F$ is the Fermi constant, $\Lambda = (1/J)[a_n < S_n > +a_p < S_p >]$, where $a_p$ and $a_n$ are the WIMP-proton and WIMP-neutron couplings, respectively, and $< S_p >\ , < S_n >$ are respectively the expectation values of the spin content of the protons and neutrons in the nucleus [59]-[61]. The factor '$\Lambda^2 J(J+1)$' is sometimes called the 'spin enhancement factor' since it carries all the spin content information of the target nucleus [1]. Here, $\frac{S(q)}{S(0)}$ behaves as the form factor with $S(q) = a_p^2 S_{pp}(q) + a_p a_n S_{pn}(q) + a_n^2 S_{nn}(q)$ as the nuclear structure function and $S(0) = \frac{2J+1}{\pi} \Lambda^2 J(J+1)$. The forms for $S_{pp}(q)$, $S_{nn}(q)$ and $S_{pn}(q)$, which are in general polynomials in $q$, for various nuclei are available in literature. Table 2.1 summaries the relevant parameters for some nuclei of our interest relevant for calculation of SD cross-sections in this thesis.

| $^A$Nucleus$_Z$ | J | odd nucleon | $< S_p >$ | $< S_n >$ |
|---|---|---|---|---|
| $^{73}Ge_{32}$ [62] | 9/2 | n | 0.030 | 0.378 |
| $^{29}Si_{14}$ [63] | 1/2 | n | -0.002 | 0.13 |
| $^{27}Al_{13}$ [64] | 5/2 | p | 0.030 | 0.343 |
| $^{23}Na_{11}$ [65] | 3/2 | p | 0.2477 | 0.0198 |
| $^{127}I_{53}$ [65] | 5/2 | p | 0.354 | 0.064 |
| $^{129}Xe_{54}$ [65] | 1/2 | n | 0.028 | 0.359 |
| $^{131}Xe_{54}$ [65] | 3/2 | n | -0.009 | -0.227 |

Table 2.1: Values of the total nuclear angular momentum (J) and the expectation values of the proton and neutron spins within the nucleus, $< S_{p(n)} >$, for various nuclei with odd numbers of protons or neutrons as indicated.

[1]Fluorine has a high spin enhancement factor and hence considered as a suitable target for studying SD interactions with WIMPs in DD experiments like PICASSO [66], COUPP [67] etc.

In this paper, following the standard practice, we study the situations when the WIMP couples to either proton (i.e. $a_n = 0$) or to neutron (i.e. $a_p = 0$); the relevant effective cross section in the two cases will be denoted by $\sigma^{\rm SD}_{\chi-p}$ and $\sigma^{\rm SD}_{\chi-n}$, respectively which are related to $\sigma^{\rm SD}_0(q)$ as,

$$\sigma^{\rm SD}_0(q) = \frac{\mu^2}{\mu^2_{\chi p(n)}}\frac{4}{3}\Lambda^2 J(J+1)\sigma^{\rm SD}_{\chi-p(n)}, \tag{2.21}$$

which can be obtained by constructing $\sigma^{\rm SD}_{\chi-p(n)}$ from Equation (2.20) for a single proton (neutron) for which $J_{p(n)}$ and $< S_p(n) >$ take the value 0.5 and $\mu \longrightarrow \mu_{\chi p(n)}$. In general both $a_n$ and $a_p$ can be non-zero, but we will not consider this case here.

## 2.2 Detection Methods and Present status of Direct Detection Experiments

DD detectors are designed to detect different types of signals generated due to WIMP scattering events depending on the detector material. The recoil energy is measured using scintillation, phonon or ionization techniques. Various experiments employ one or more of the three basic strategies for detecting nuclear recoils, as discussed below.

A recoiling nucleus may transfer energy to a nucleus in the crystal lattice and thus generates lattice vibrations (phonons). If the crystal is cryogenically cooled, the resulting phonon signal can be collected to give a measure of the original energy of the recoiling nucleus. A bolometer, which is basically a resistor, is thermally isolated and exposed to the incident phonons. As the bolometer absorbs the incident energy, its temperature change leads to change in resistance of the device.

This change in electrical resistance is amplified first by a SQUID circuit placed within the cryostat with the detector itself and then by a sophisticated series of amplifiers kept at room temperature. This amplified change in resistance generates an electric pulse which is measured to calculate the phonon energy.

A recoiling nucleus can also often ionize nearby atoms as it loses energy. This free charge is directed by a drift electric field and collected at the electrodes as the ionization signal. The recoil energy of nucleus is sometimes taken up by electrons in the target material to reach a bound excited state. It subsequently radiates to attain a lower energy state through scintillation, which can be detected by photo multiplier tubes (PMT). The ratio of the ionization or scintillation to phonon energy (called yield) allows discrimination of the nuclear-recoil signal from more abundant electron-recoil backgrounds on an event-by-event basis. Figure 2.3 schematically summarizes the basic detection methods used by some of the currently operating detectors.

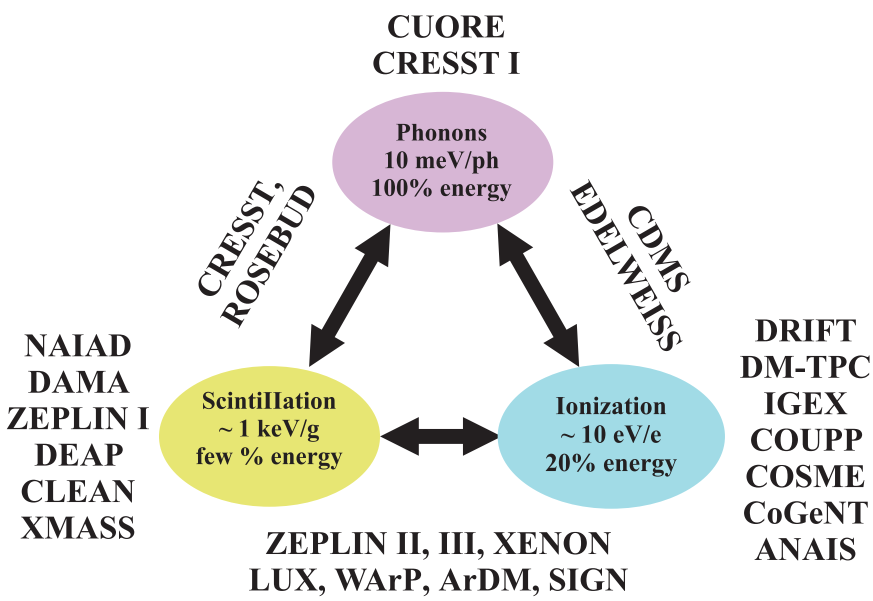


Figure 2.3: Different direct detection experiments for weakly interacting massive particle candidates for dark matter and their strategies for detection.

DD experiments are mostly performed in underground locations such as in deep mines or under heavy rock overburden to cut off backgrounds due to cosmic rays. However, there are local backgrounds like radioactive decay from surrounding rocks which are cut off by proper shielding of the detector material. Unfortunately, sometimes the shielding material, the supporting clamps or the internal contamination in the target material itself can act as a source of background. Though electron recoils can be discriminated from nuclear ones based on ionization or scintillation yield, it's the neutrons (mostly cosmic ray muon-induced) undergoing nuclear recoils that mimic WIMP-like signals. However, a 1-2 km of rock overburden aids suppressing the atmospheric muon flux by 5-7 orders of magnitude. Neutron recoils are mostly eliminated on the basis of multiple scattering or fiducialization (considering a certain inner core part of the target for event analysis to disregard surface events). Hence, a set up with proper shielding of high-Z materials such as lead or copper, plus polyethylene to moderate the neutron and alpha particles, plastic scintillator as muon veto, ultra pure targets etc. are necessary to suppress most of the background induced scattering events to facilitate the identification of actual WIMP-nucleus scattering events.

There are several ongoing experiments aiming for detection of WIMPs via direct DM searches. However, there have been no confirmed detection of DM till date. Although some experiments claim to have detected a positive signal, many others have claimed no events or have ascribed events to backgrounds after data analysis. In the case of positive results from a DD experiment, the observed events are compared to the expected number using Equation (2.4) with an assumed astrophysical model for the halo. Hence, a region in the parameter space of WIMP mass vs WIMP-nucleon cross-section can be identified at a certain confidence level enclosing the most likely values of mass and cross-section. In the case of null events, or in the case of tentatively positive signals that can be also ascribed to the background, the results are generally expressed as an 'exclusion plot' in the WIMP mass vs WIMP-nucleon cross-section parameter space such that, for any given WIMP mass, the cross-section larger than a certain upper limit are excluded at a given confidence level. The compatibility of several DM experiments can hence be studied in this two dimensional plane.

Below we give a brief review of the present status of some of the major DD experiments. The **DA**rk **MA**tter (DAMA) experiment set up at Gran Sasso underground facility has claimed detection of annual modulation of the event rates and ascribed them to DM particles [2]. Both DAMA/NaI and DAMA/LIBRA projects which are part of the DAMA collaboration, use ultra-pure sodium iodide [NaI(Tl)] crystal as the target material which are connected to several PMTs for detection of scintillation signals. The threshold of each PMT is set at single photoelectron level. Using a target mass of 250 kg NaI, DAMA/LIBRA [68] has claimed non zero values for modulation amplitude with an exposure of 0.53 ton-yr from data collected for 4 annual cycles. Combining with data from former DAMA/NaI [69] for 7 annual cycles, with a mass of 100 kg and a total exposure of 0.29 ton-yr, and thus with a total exposure of 0.82 ton-yr, the presence of DM particles in the Galactic halo is claimed at 8.2 $\sigma$ C.L. in 2-6 keV recoil energy window. Recently, based on 14 year data with 1.33 ton-yr exposure, DAMA/LIBRA [53] has reported detection of annual modulation at 9.3 $\sigma$ C. L. However, it has claimed null results on diurnal variation of event rates limited by their present level of sensitivity [70].

[2] Though several non-DM explanations also exist in literature; see [55].

Located in Soudan Underground Laboratory in Minnesota, the **Co**herent **Ge**rmanium **N**eutrino **T**echnology (CoGeNT) [54] collaboration, employing p-type point contact Germanium detector cooled to liquid nitrogen temperatures, has showed an excess of events above the expected background that are potentially compatible with a DM signal. The first data set was obtained with 56 days of operation with 330 g of fiducial mass in a ionization signal window $\sim$ 0.4-3.2 keV. The results of the experiment were claimed to be compatible with a DM mass of $\sim$ 7-11 GeV for SI WIMP-nucleon cross-section in the range $(3-10)\times 10^{-41}\mathrm{cm}^2$. A later analysis of an accumulated data set spanning over 15 months has showed a 2.8 $\sigma$ significance modulation of the monthly low energy event rates in the ionization window of 0.5-3.0 keV which has been considered as an evidence compatible with a DM interpretation.

**Cr**yogenic **R**are **E**vent **S**earch with **S**uperconducting **T**hermometers (CRESST)-II, installed in Gran Sasso Laboratory, uses Calcium Tungstate ($CaWO_4$) crystals as target material and measures simultaneous light and phonon signals under cryogenic condition. Sixty-seven events were found in the signal region of 10-140 keV with an exposure of 730 kg-days. Background contributions from leakage of e/$\gamma$-events, neutrons, $\alpha$-particles, recoiling nuclei in $\alpha$-decays etc. were claimed to be not sufficient to explain all the observed events [71]. The excess above the background expectation of $\sim$ 40 events could be explained by a WIMP signal with a WIMP mass, $m_\chi \sim 11.6$ GeV at WIMP-nucleon SI cross-section, $\sigma^{\mathrm{SI}}_{\chi-nucleon}$=$3.7\times 10^{-41}\mathrm{cm}^2$ or $\sim$ 25.3 GeV at $\sigma^{\mathrm{SI}}_{\chi-nucleon}$=$1.6\times 10^{-42}\mathrm{cm}^2$.

**C**ryogenic **D**ark **M**atter **S**earch or (CDMS-II) experiment, using ultra cold Germanium/Silicon detectors, measures both the ionization and phonon energy deposited by each particle interaction. The setup is installed at the Soudan

Underground Laboratory under cryogenic condition. In 2013, this collaboration using Silicon detector, has reported three DM candidate events with a raw exposure of 140.2 kg-days [72]. A profile likelihood ratio test gave a 0.19% probability for the known-background-only hypothesis when tested against the alternative WIMP + background hypothesis and claimed 8.6 GeV to be the most likely DM mass with a WIMP-nucleon SI cross section of $1.9 \times 10^{-41}\text{cm}^2$. However, the collaboration has reported negative result on annual modulation [73].

ZEPLIN-III [74], installed at the Boulby Underground Laboratory, employs a two phase 12 kg mass Xenon detector and measures both scintillation and ionization energy deposited by particle interactions. A raw fiducial exposure of 1,344 kg-days was accrued over 319 days of continuous operation in the second science run and a total of eight events were observed in the signal acceptance region in the nuclear recoil energy range of 7-29 keV, which is compatible with background expectations. This allows the exclusion of the SI WIMP-nucleon cross-section with minimum at $\sim 4.8 \times 10^{-44}\text{cm}^2$ near $m_\chi \sim 50$ GeV cm$^{-3}$ at 90% C.L. Combined with data from the first run [75], this result improves the WIMP-nucleon cross-section (under SI interactions) to $\sim 3.9 \times 10^{-44}\text{cm}^2$. The corresponding WIMP-neutron SD cross-section 90% C.L. upper limit was found to be $8.0 \times 10^{-39}\text{cm}^2$ only.

XENON-100, operating at Gran Sasso Laboratory since 2009 is a dual-phase (liquid and gas) time projection chamber where the detector material is ultra-pure liquid Xenon (LXe). A nuclear recoil from particle scattering is inferred from the simultaneous measurements of scintillation light and ionization electrons, together with the arrival direction. It has a resolution of $\leq 1\,\text{keV}$ at 1 keV and $\sim 3$ keV at 30 keV. Based on 225 livedays $\times$ 34 kg of exposure, the experiment yielded no evidence for DM interactions in the 6-30.5 keV window [76]. The collaboration has published a WIMP-nucleon SI elastic scattering cross section upper limit with minimum of $2 \times 10^{-45}\text{cm}^2$ for $m_\chi \sim 55$ GeV at 90 % CL which is more stronger than those set by by EDELWEISS-II [77], ZEPLIN-III [74], SIMPLE [78] (for $m_\chi > 6\,\text{GeV}$) and incompatible with positive results from CoGeNT [54], CRESST-II [71], DAMA/LIBRA [68] and CDMS-Si [72]. Also, in the SD case, XENON- 100 [79] has set the stringent upper limit on WIMP- neutron cross sections for $m_\chi > 6\,\text{GeV}$ with a minimum at $3.5 \times 10^{-40}\text{cm}^2$ at $m_\chi \sim 45$ GeV at 90 % C.L. which is almost two orders of magnitude stronger than the SD WIMP-proton minimum cross section.

The Large Underground Xenon (LUX) experiment, located in the Homestake mine in South Dakota, records scintillation and ionization signals under cryogenic condition from a dual-phase time-projection chamber employing LXe target. With 118 kg of fiducial volume and data taking for 85.3 live days, the collaboration [80] has reported the so far strongest exclusion limits of $\sigma^{\text{SI}}_{\chi-nucleon} = 7.6 \times 10^{-46}\text{cm}^2$ at 33 GeV of WIMP mass at 90 % C.L. and disagreement over the low WIMP mass scenarios hinted at by several other experiments. The LUX results are incompatible with the results from EDELWEISS-II [77], CDMS-II [81], ZEPLIN -III [74], SIMPLE [78], XENON-100 [76], CDMS-Si [72] and CRESST-II [71] and are also incompatible with the positive claims of annual modulation by CoGeNT [54] and DAMA/LIBRA [68].

The **P**roject **i**n **Ca**nada to **S**earch for **S**upersymmetric **O**bjects (PICASSO) experiment [66], located at SNOLAB, uses droplets of superheated liquid $C_4F_{10}$ embedded in polymerized water saturated acrylamide. The phase transition of the droplets from liquid to vapour phase due to energy deposition by recoiling nuclei leads to an acoustic signal detected by piezoelectric crystals. The resetting of the energy threshold to a low value of $\sim 1.7$ keV combined with the light $^{19}$F target nuclei, gives PICASSO a good sensitivity to WIMPs with $m_\chi < 10\,\mathrm{GeV}$. The experiment has used a total target mass of 0.72 kg and an exposure of 114 kg-days. By tuning the operating conditions, these detectors can be made insensitive to gamma and beta backgrounds, while nuclear recoil interactions (from WIMPs or neutrons) and alphas can inject enough energy into the droplets to cause a phase transition. In this type of detectors, particularly alpha particles pose a serious background. However, the pulse characteristics of the acoustic signals of the bubble formation can be used to effectively to distinguish them from nuclear recoil events. The specific spin-structure of $^{19}$F makes it very sensitive to proton-only couplings ($a_n = 0$). It has reported null results so far, with upper limit on SD WIMP-proton cross-section as, $\sigma^{\mathrm{SD}}_{\chi-p}$ of $3.2 \times 10^{-38}\mathrm{cm}^2$ at $m_\chi \sim 20$ GeV at 90 % C.L. There are other experiments too employing similar detection technology and sensitive to SD cross-sections, viz., SIMPLE [78] and COUPP [67].

We close this chapter by noting and emphasizing that, as clear from the discussions in Section 2.1 [see in particular Equation 2.4)], interpretation of the results of DD experiments depend on two essential astrophysical inputs, namely, the local (i.e., the Solar neighborhood) density of DM ($\rho_{\mathrm{DM},\odot}$) and the local velocity distribution function of the WIMPs, in the rest frame of Galaxy. In this thesis, we shall attempt to derive these quantities from a physically acceptable steady state PSDF, $f(\mathbf{x}(t), \mathbf{v}(t))$, describing the Galactic halo populated by WIMP candidates of DM. It is worth mentioning that all the results from various DD experiments mentioned above are all based on standard assumptions for the PSDF of the DM halo embodied in the so called ‘standard halo’ model (SHM) [44]-[47]. A major theme of the present thesis is to highlight the limitations of the SHM as a model of the Galactic DM halo and study possible models beyond SHM that can better represent the DM halo of the Galaxy based on observational data on the rotation curve (RC) of our Galaxy.

To set the stage, though, in the next chapter, we will focus SHM first and fit the parameters of the model to the observed RC data of the Galaxy to examine how the model fares in fitting the RC data of the Galaxy in addition to visible matter (VM) contribution. We shall study the modifications of the 'isothermal sphere' (IS) distribution function, the PSDF representing the SHM, in fitting the RC data by including the effect of gravitational influence of VM on the DM particles in a self-consistent manner. Finally, we shall study the implications of a self-consistent IS describing the DM halo of our Galaxy for the analysis of several DD experiments and compare the results with those within the context of the customarily used 'isolated' SHM, i.e., halo description without including the VM effect on the phase space structure.

# Chapter 3

# The Isothermal Halo Model for the Milky Way's Dark Matter Halo

## 3.1 Introduction

The WIMPs, hypothesized to constitute the dark matter (DM) halo of the Galaxy, can, for all practical purposes be considered as essentially collisionless and dissipationless particles. As such, the phase space distribution function (PSDF), $f(\mathbf{x}(t), \mathbf{v}(t))$, of the WIMPs can be considered to be a steady-state solution of the collisionless Boltzmann equation (CBE) or Vlasov Equation [43]:

$$\frac{\delta f}{\delta t} + \Sigma_{i=1}^{3}\left[\frac{\delta}{\delta x_i}(f\dot{x}_i) + \frac{\delta}{\delta v_i}(f\dot{v}_i)\right] = 0. \tag{3.1}$$

The CBE essentially expresses the fact that the local phase space density remains constant for an observer moving along a particle trajectory. In general, there can be many steady state solutions of the CBE and the actual PSDF of the WIMPs constituting the halo of the Galaxy is a priori unknown. One approach is to make a suitable ansatz for the PSDF that would be a solution of the steady state CBE. In doing this, one is guided by the Jeans Theorem, which states,

**JEANS THEOREM [43]:** *Any steady state solution of the collisionless Boltzmann Equation depends on the phase space co-ordinates only through integrals of motion in the given potential, and any function of the integrals yields a steady state solution of the collisionless Boltzmann Equation.*

Therefore, mathematically any function, $f(\mathbf{x}(t), \mathbf{v}(t)) = f(I_1, I_2 ... I_i)$, of the integral(s) of motion, $I_i(\mathbf{x}(t), \mathbf{v}(t))$, should satisfy the time independent CBE. For a spherically symmetric DM halo of the Galaxy the simplest ansatz is to choose $f(\mathbf{x}(t), \mathbf{v}(t)) = f(E)$, where $E = \Phi(\mathbf{x}) + \frac{1}{2}v^2$ is the total energy (per unit mass) of the system, $\Phi(\mathbf{x})$ being the gravitational potential and $v = |\mathbf{v}|$ denotes the speed of a DM particle. Such a system is characterized by an isotropic velocity distribution function (VDF). In choosing a specific form of $f(E)$, a particularly popular case is $f(E) \propto e^{-E/\sigma^2}$. This describes a system of collisionless particles constituting a so called "isothermal sphere" (IS) [43]. The corresponding halo PSDF, consisting of WIMP candidates of DM, can be written as,

$$f(\mathbf{x}, \mathbf{v}) = f(E) = \frac{\rho_0}{(2\pi\sigma^2)^{\frac{3}{2}}} e^{-E/\sigma^2}, \tag{3.2}$$

which is characterized by a density parameter, $\rho_0$, and velocity parameter, $\sigma$.

The density of DM at any point $\mathbf{x}$ is,

$$\rho(\mathbf{x}) = \int f(\mathbf{x}, \mathbf{v}) d^3\mathbf{v} = \rho_0 e^{\left[-\Phi(\mathbf{x})/\sigma^2\right]}. \tag{3.3}$$

Clearly, with center of the IS chosen to be at the origin, and boundary condition chosen as $\Phi(0) = 0$ implies that $\rho_0$ is the central density of the IS. The solution for the isothermal density profile can be obtained by using the Poisson's equation given by,

$$\nabla^2\Phi(\mathbf{x}) = 4\pi G\rho(\mathbf{x}). \tag{3.4}$$

Assuming spherical symmetry we replace $\rho(\mathbf{x})$ in the above equation by using Equation (3.3) to obtain,

$$\frac{1}{r^2}\frac{d}{dr}\left(r^2\frac{d\Phi}{dr}\right) = 4\pi G\rho_0 e^{\left[-\Phi/\sigma^2\right]}. \tag{3.5}$$

Again in terms of density, we have,

$$\frac{1}{r^2}\frac{d}{dr}\left(r^2\frac{d}{dr}(\ln\rho)\right) = -\frac{4\pi G}{\sigma^2}\rho. \tag{3.6}$$

This equation has a trivial solution as, $\rho(r) = \frac{\sigma^2}{2\pi G r^2}$, with infinite density at r=0 is known is the "Singular Isothermal Sphere". A well behaved non-singular IS solution can be obtained by imposing appropriate boundary condition on the gravitational potential. Using, $\phi = \sigma^2\zeta$ and $r = \alpha\eta$ where $\alpha^2 = \frac{\sigma^2}{4\pi G\rho_0}$ we get,

$$\frac{d^2\zeta}{d\eta^2} + \frac{2}{\eta}\frac{d\zeta}{d\eta} = e^{-\zeta}. \tag{3.7}$$

Under the boundary condition, $\zeta = \zeta' = 0$ at $\eta = 0$, the above equation provides a non-singular solution to IS. Near the centre $\zeta \propto \eta^2$ and therefore, $\rho = \rho_0 e^{-\zeta}$ behaves as $\rho_0(1+\frac{\eta^2}{\eta_0^2})^{-1}$. In terms of actual radial distance, the density profile for the non-singular solution appears as $\rho_0(1+\frac{r^2}{r_0^2})^{-1}$ with $r_0 = \sqrt{\frac{9\sigma^2}{4\pi G\rho_0}}$, where, G is the universal gravitational constant. This clearly represents a cored density profile that falls off as $1/r^2$ for $r \ll r_0$ and characterized by a core radius $r_0$. At $r = r_0$, the projected surface density falls to $\sim$ half of its central value.

The VDF of the DM particles constituting the system is defined as,

$$f_{\mathbf{x}}(\mathbf{v}) = \frac{1}{\rho(\mathbf{x})} f(\mathbf{x}, \mathbf{v}). \tag{3.8}$$

The nomenclature 'isothermal sphere' arises from the fact that the VDF is of Maxwell-Boltzmann form describing an isothermal gas whose velocity dispersion, $\langle v^2 \rangle^{1/2}$, is independent of position $\mathbf{x}$, which is easily obtained by substituting Equations (3.3) and (3.2) in Equation (3.8) as,

$$f(\mathbf{v}) = \frac{1}{(2\pi\sigma^2)^{3/2}} e^{-\frac{v^2}{2\sigma^2}}, \tag{3.9}$$

independent of $\mathbf{x}$.

In the Maxwellian distribution, the parameter, $\sigma$, is related to the velocity dispersion as $\langle v^2 \rangle^{1/2} = \sqrt{3}\sigma$.

At a basic level, the justification for adopting this PSDF as a description of the DM halo of the Galaxy, comes from the work of Lynden-Bell [82], who argued that evolution of systems of collisionless particles under gravitational collapse is governed by the process of "violent relaxation" whereby the observationally relevant 'coarse-grained' PSDF of the system rapidly relaxes, due to collective effects, to a quasi-Maxwellian stationary state [1]. However, one must keep in mind that the actual PSDF of the DM halo is not known and the IS is only a simple and convenient model and the real PSDF may be rather different from this.

An important property of a self-gravitating IS is that, the radial profile of the circular speed, $V_c$, of a test particle in the gravitating field of the system, in other words, the rotation curve (RC), given by $V_c(r) = \sqrt{G\frac{M(r)}{r}}$, where M(r) is the mass interior to r, is asymptotically flat, with circular velocity at $r \to \infty$ related to the velocity dispersion, $\langle v^2 \rangle^{1/2}$, as [43],

$$V_c(r \to \infty) = \sqrt{2}\sigma = \sqrt{\frac{2}{3}}\langle v^2 \rangle^{1/2}. \tag{3.10}$$

In the 'standard halo' model (SHM), the DM halo is an IS with specific choice of parameters. Assuming that the RC of the Milky Way is "flat" at all distances from the Solar location all the way up to $r \to \infty$, we can put $V_c(\infty) \approx V_c(R_0)$= 220 $\mathrm{km\,s^{-1}}$ for the choice of $V_c(R_0) = V_0 = 8.5$ kpc according to the GCs: $\left[\frac{R_0}{\mathrm{kpc}}, \frac{V_0}{\mathrm{km\,s^{-1}}}\right] = [8.5, 220]$ afixed by the adopted RC data set [83]. Hence, from Equation (3.10), one can calculate the DM velocity dispersion parameter [2], $\langle v^2 \rangle^{1/2} = \sqrt{3}\sigma \simeq 270\,\mathrm{km\,s^{-1}}$. To fix the other remaining parameter, $\rho_0$, it is convenient to consider the value of the DM density at the Solar location, $\rho_{\mathrm{DM},\odot}$, which is currently unknown, but can in principle be estimated from dynamics of stars in the Solar neighborhood or by mass modeling of the Galaxy considering dynamical constraints like RC data, motion of high velocity stars etc. giving a wide range of values [see details in Chapter 6]. In the SHM, the local DM density is chosen as $\rho_{\mathrm{DM},\odot} \simeq 0.3\ \mathrm{GeV\,cm^{-3}}$. The SHM is generally taken as a sort of

[1] The 'fine-grained' DF may, however, never reach equilibrium.

[2] A recent study suggests a somewhat higher value of $V_{c,\odot} = 244\,\mathrm{km\,s^{-1}}$ [84], which would imply a correspondingly higher value of $\langle v^2 \rangle^{1/2} \approx 299\,\mathrm{km\,s^{-1}}$.

benchmark model of the DM halo of the Galaxy, and the results of various DM search experiments are mostly analyzed within the context of this model.

In the following sections, we first discuss how the SHM fares as a description of the RC data for the Galaxy and then study the RC fit to the halo described by an IS including the gravitational influence of the observed visible matter (VM) (since, it's the VM that dominates the gravitational potential especially in the inner regions of the Galaxy) on the DM particles in a self-consistent manner. Thereafter, we study the implications of the IS model of the Galaxy's DM Halo for the analysis of the results of several DM direct detection experiments for WIMPs, considering elastic and inelastic scattering of WIMPs under spin-independent (SI) interactions and summarize at the end.

## 3.2 Fit to Rotation Curve

The circular rotation speed, $V_c(R)$, as a function of the galactocentric distance $R$, is calculated as,

$$V_c^2(R) = R\frac{\partial}{\partial R}\Big[\Phi_{\rm DM}(R, z=0) + \Phi_{\rm VM}(R, z=0)\Big], \tag{3.11}$$

where $z$ is the distance normal to the equatorial plane.

The gravitational potentials for VM, $\Phi_{\rm VM}(\mathbf{x})$, and DM ,$\Phi_{\rm DM}(\mathbf{x})$, can be calculated by numerically solving the respective Poisson's equations given the respective densities ($\rho_{\rm VM}(\mathbf{x})$ and $\rho_{\rm DM}(\mathbf{x})$). The Poisson's equations are,

$$\nabla^2\Phi_{\rm VM}(\mathbf{x}) = 4\pi G\rho_{\rm VM}(\mathbf{x})\,, \quad \text{and} \;\; \nabla^2\Phi_{\rm DM}(\mathbf{x}) = 4\pi G\rho_{\rm DM}(\mathbf{x})\,, \tag{3.12}$$

with appropriate boundary conditions,

$$\Phi_{\rm VM}(0) = \Phi_{\rm DM}(0) = 0\,, \quad \text{and} \quad (\nabla\Phi_{\rm VM})_{|\mathbf{x}|=0} = (\nabla\Phi_{\rm DM})_{|\mathbf{x}|=0} = 0. \tag{3.13}$$

To calculate the theoretical RC for our Galaxy, we require forms of the density distribution of DM halo and VM in the Galaxy. We assume that the density distribution of the VM can be effectively described by a spheroidal bulge superposed on an axisymmetric disk [85]. The density distributions of these components are given, respectively, by,

$$\rho_b(r) = \rho_{b0}\left(1 + \frac{r^2}{r_b^2}\right)^{-3/2}\,, \tag{3.14}$$

and

$$\rho_d(R,z) = \frac{\Sigma_\odot}{2z_h} e^{-(R-R_0)/R_d} \;\; e^{-|z|/z_h}\,, \tag{3.15}$$

where $r = (R^2 + z^2)^{1/2}$. Typical parameter values are [85, 86], for bulge central density: $\rho_b(0) = 4.2 \times 10^2\, M_\odot\,{\rm pc}^{-3}$, bulge scale length: $r_b = 0.103\,{\rm kpc}$, disk scale length: $R_d = 3\,{\rm kpc}$, disk scale height: $z_h = 0.3\,{\rm kpc}$ and the surface density of the disk at the Solar location: $\Sigma_\odot \approx 48\, M_\odot\,{\rm pc}^{-2}$, with $R_0 = 8.5\,{\rm kpc}$ as the Solar galactocentric distance. The total VM density is, therefore,

$$\rho_{\rm VM}(\mathbf{x}) = \rho_b(r) + \rho_d(R,z), \tag{3.16}$$

which can be plugged in the RHS of the Poisson's equation for VM [Equation

(3.12)] to solve for $\Phi_{\mathrm{VM}}(\mathbf{x})$ using a numerical procedure. The Poisson solver code used here has been verified with known analytic solutions for several known $\rho(\mathbf{x}) - \Phi(\mathbf{x})$ pairs available in literature [43].

There exist more detailed models of the mass distribution of the VM in the Galaxy than those adopted above, involving a possible stellar "thick" disk (with a scale height of $\sim 1\,\mathrm{kpc}$) and contribution by the Galaxy's interstellar medium in addition to the stellar spheroid plus the bulge and "thin" disk described by Equations (3.14) and (3.15). However, there are also large uncertainties in the values of the parameters that characterize these various components, as is clear from the values of the parameters of the two representative models summarized, for example, in Table 2.3 of Ref. [43]. We find, as shown below, that the typical values of the various VM parameters chosen above give a reasonably good fit to the RC data in the inner Galaxy region, $R \lesssim R_0$, where the effect of the DM is subdominant. As such, this "minimal" model of the distribution of the VM of the Galaxy adopted above is, we believe, good enough for the purpose of illustrating the general nature of the effect of the DM halo on the RC of the Galaxy.

To solve for $\Phi_{\mathrm{DM}}(\mathbf{x})$, we plug in the isothermal density profile given by Equation (3.3) as $\rho_{\mathrm{DM}}(\mathbf{x})$ to the RHS of the Poisson's equation for DM [Equation (3.12)]. It is important to note that, in the presence of VM, a DM particle responds to the sum of gravitational potentials due to both DM and VM components. The methodology to account for this is adopted along the lines described in earlier works [48, 49] which included the effects of the gravitation of the VM on the DM in a self-consistent manner. Therefore, the $\Phi(\mathbf{x})$ term appearing in the right hand side of Equation (3.3) is actually,

$$\Phi(\mathbf{x}) \equiv \Phi_{\rm tot}(\mathbf{x}) = \Phi_{\rm DM}(\mathbf{x}) + \Phi_{\rm VM}(\mathbf{x}), \tag{3.17}$$

giving,

$$\rho_{\rm DM}(\mathbf{x}) = \rho_0 e^{[-\Phi_{\rm DM}(\mathbf{x}) + \Phi_{\rm VM}(\mathbf{x})]/\sigma^2}. \tag{3.18}$$

Consequently, the Poisson's equation for DM is modified to,

$$\nabla^2 \Phi_{\rm DM}(\mathbf{x}) = 4\pi G \rho_0 e^{[-\Phi_{\rm DM}(\mathbf{x}) + \Phi_{\rm VM}(\mathbf{x})]/\sigma^2}. \tag{3.19}$$

The Poisson's equation for DM (Equation 3.19) is thus a coupled non linear equation which can be solved to generate self-consistent solutions of $\Phi_{\rm DM}(\mathbf{x})$ and $\rho_{\rm DM}(\mathbf{x})$ through an iterative procedure. The procedure is as follows: for the first iteration, we set $\Phi_{\rm DM}(\mathbf{x}) = 0$ on the RHS of Equation (3.19) and numerically solve for $\Phi_{\rm DM}$. Then, we use this new $\Phi_{\rm DM}$ to recalculate the new $\rho_{\rm DM}$ from Equation (3.18) and this process is continued until convergence is reached.

To asses the degree of fit of the theoretically calculated RC to the actual data, the $\chi^2$ - test statistic has been used. It is defined as,

$$\chi^2 \equiv \sum_{i=1}^{i=N} \left( \frac{V^i_{\rm c,obs} - V^i_{\rm c,th}}{V^i_{\rm c,error}} \right)^2, \tag{3.20}$$

where $V^i_{\rm c,obs}$ and $V^i_{\rm c,error}$ are, respectively, the observational value of the circular rotation speed and its error at the $i$-th value of the galactocentric distance, and $V^i_{\rm c,th}$ is the corresponding theoretically calculated circular rotation speed.

In the customary mass modeling approach, the DM halo is often represented as a isolated or single component SHM, where the density is simply

$$\rho_{\rm DM}(\mathbf{x}) = \rho_0 e^{\left[-\Phi_{\rm DM}(\mathbf{x})/\sigma^2\right]}. \tag{3.21}$$

For the single component SHM, the potential, $\Phi_{\rm DM}(\mathbf{x})$, obtained by solving the Poisson's equation for DM given by Equation (3.12) with $\rho_{\rm DM}(\mathbf{x})$ given by Equation (3.21) (rather than Equation 3.18), is simply added to the VM potential, $\Phi_{\rm VM}(\mathbf{x})$, to calculate the $V_c^2$ using Equation (3.11).

Figure 3.1 shows the resulting fit of the theoretical $V_c$ profile to the RC data given by Honma and Sofue by analysis of Galactic H1 survey results [83] in both linear and logarithmic scales with the single component SHM, i.e., without including the gravitational influence of VM on DM (henceforth referred to as the *uncoupled* case). It is seen that, reasonably good fit to the RC data is obtained out to a galactocentric distance of $\sim 10$ kpc beyond which the fit quality is considerably poorer. Note that, the dominant contribution to the RC within the Solar circle (i.e., R $\leq 8.5$ kpc) comes from VM. The DM starts dominating the contribution to RC only at R $\geq 15$ kpc and indeed the RC asymptotically approaches the expected value $V_c(\infty) = \sqrt{2/3}\,\langle v^2\rangle^{1/2} \simeq 220\,{\rm km\,s^{-1}}$ value. Thus, it is clear that the VM dominates the gravitational dynamics in the inner regions of the Galaxy up to the Solar distance $\sim 8.5$ kpc, and the DM controls the gravitational dynamics of the Galaxy only at larger galactocentric distances. However, as seen from Figure 3.1, the single component halo model assumed in the SHM with the standard values of its parameters (namely, $\rho_{\rm DM,\odot} \simeq 0.3$ GeV cm$^{-3}$ and $\langle v^2\rangle^{1/2} \simeq$ 270 km s$^{-1}$) does not seem to be good fit to the RC data at large galactocentric distances either. The $\chi^2$ (scaled by the degree of freedom (dof) i.e., number of

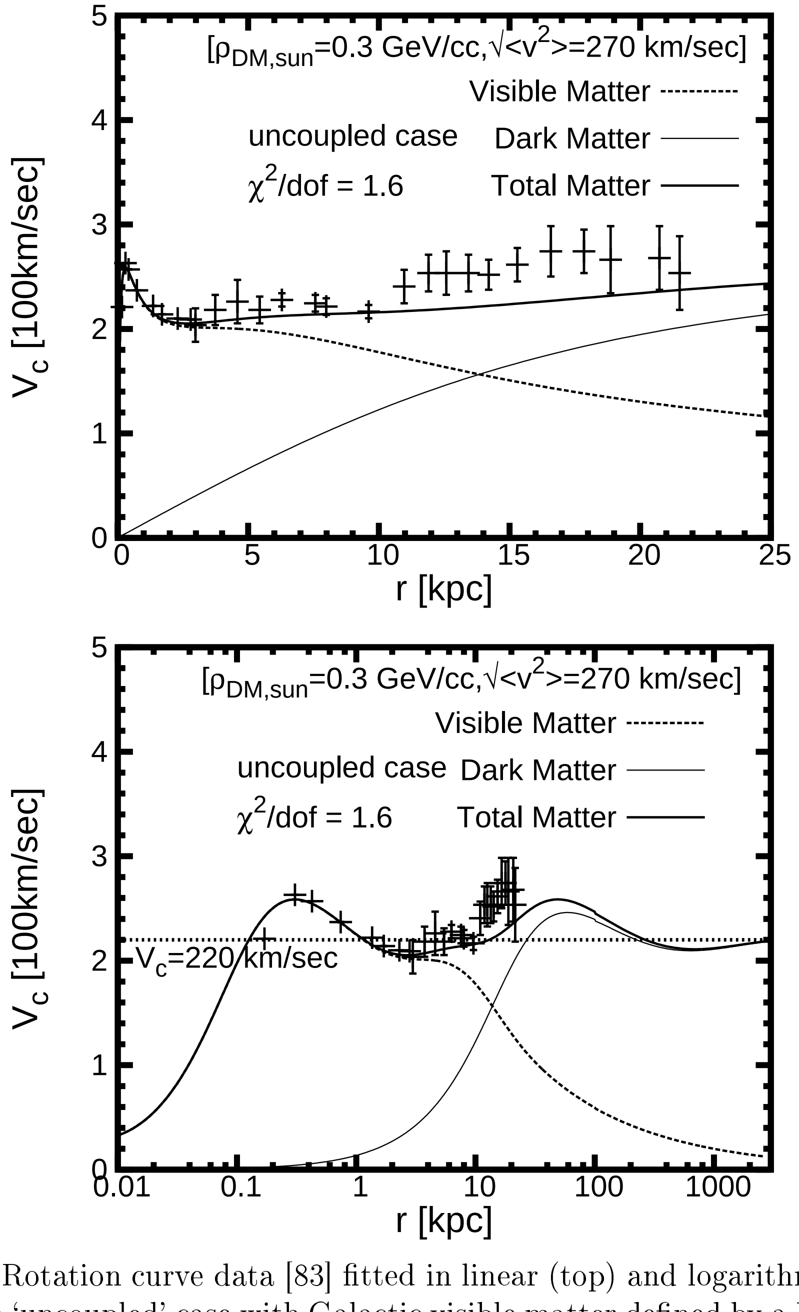


Figure 3.1: Rotation curve data [83] fitted in linear (top) and logarithmic (bottom) scale for the 'uncoupled' case with Galactic visible matter defined by a Bulge + Disk [see Equations (3.14) and (3.15)] and the dark matter halo described by a single component standard halo model with dark matter velocity dispersion, $\langle v^2\rangle^{1/2} \simeq 270$ $\mathrm{km\,s^{-1}}$ and a local dark matter density, $\rho_{\mathrm{DM},\odot} \simeq 0.3\ \mathrm{GeV\,cm^{-3}}$. The dotted line for circular velocity value 220 $\mathrm{km\,s^{-1}}$ denotes the asymptotic value of the SHM rotation curve profile for $\langle v^2\rangle^{1/2} \simeq 270\ \mathrm{km\,s^{-1}}$.

rotation curve data points) indicated in the inset is measure of the fit. Motivated by these considerations, we next consider the more realistic *coupled* case, in which we include the gravitational influence of the VM on the phase space structure of the IS that represents the DM halo, in a self-consistent manner through Equations (3.18) and (3.19). The iterative procedure used to solve these two equations has already been discussed above.

Inclusion of the gravitational influence of the VM on the DM particles has two related effects: (a) The additional gravitational pull of the VM draws the DM particles towards the central region, thereby, increasing the central density of the DM particles there. However, this is accompanied by, (b) a decrease of the core radius of the density profile of the DM, since, as mentioned earlier, the core radius ($r_0$) of the IS is $\propto \sqrt{\frac{\sigma^2}{\rho_0}}$, where $\sigma = \frac{\langle v^2\rangle^{1/2}}{\sqrt{3}}$, where $\langle v^2\rangle^{1/2}$ is the velocity dispersion and $\rho_0$ is the central density of the DM particles. The net result is that the halo DM density profile becomes too centrally concentrated and the core radius becomes too small to be consistent with the DM density of $\rho_{\rm DM,\odot} \simeq 0.3\;\,{\rm GeV\,cm^{-3}}$ at the Solar location required for a good fit to the observed RC data, *unless the velocity dispersion, $\langle v^2\rangle^{1/2}$, is correspondingly increased*. Indeed, from our numerical calculations we find that, for the given set of the observed VM parameters, a value of DM $\langle v^2\rangle^{1/2} \simeq 270\;\,{\rm km\,s^{-1}}$ (as assumed in the SHM), can only support a maximum value of $\rho_{\rm DM,\odot} \simeq 0.03\;\,{\rm GeV\,cm^{-3}}$, an order of magnitude smaller than the standard value of $\rho_{\rm DM,\odot} = 0.3\;\,{\rm GeV\,cm^{-3}}$. These values of the $\langle v^2\rangle^{1/2}$ and $\rho_{\rm DM,\odot}$, however, provide a rather poor fit to the RC data indicated by the $\chi^2$ value (scaled by the dof) as seen from the upper panel of Figure 3.2. The obvious solution is to require higher values of the $\langle v^2\rangle^{1/2}$ of the DM particles. In fact we find that, to support a value of $\rho_{\rm DM,\odot} = 0.3\;\,{\rm GeV\,cm^{-3}}$, we need a minimum

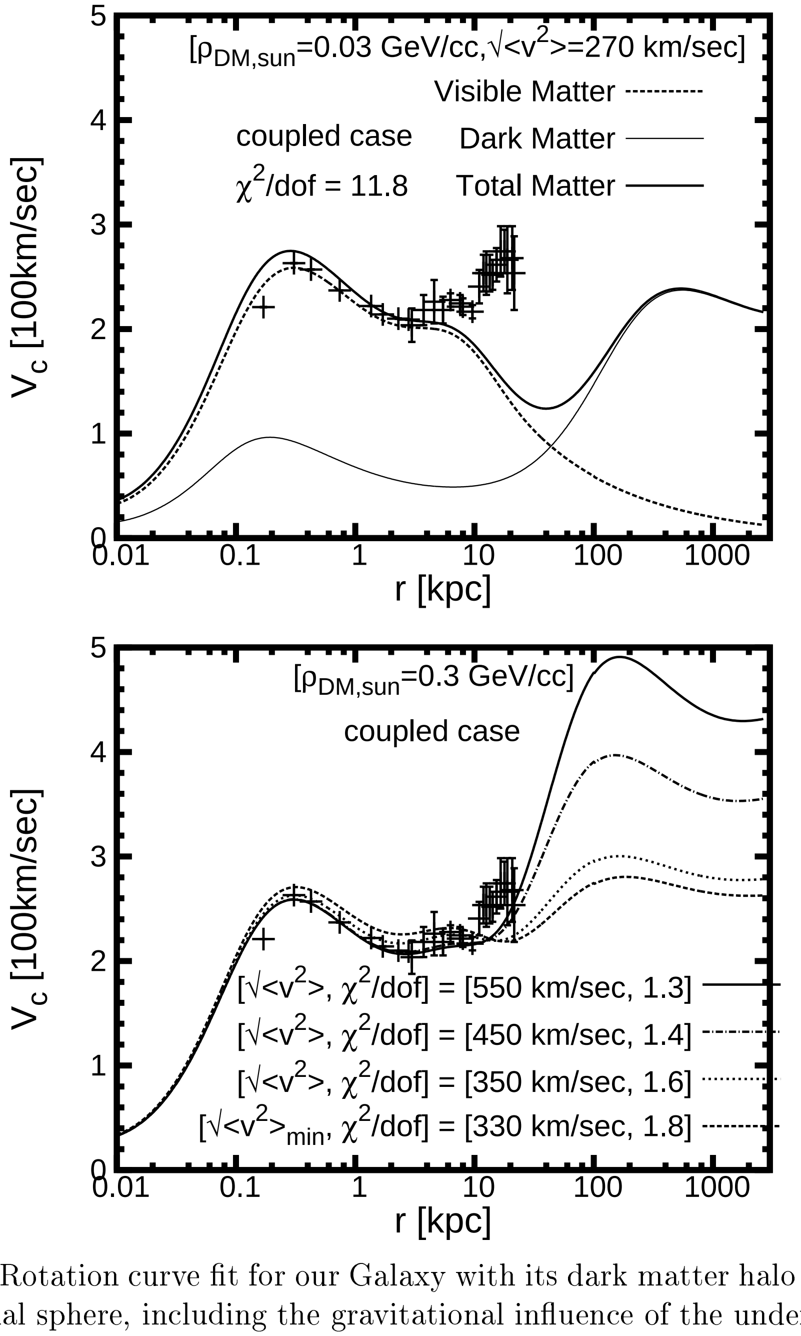


Figure 3.2: Rotation curve fit for our Galaxy with its dark matter halo described by an isothermal sphere, including the gravitational influence of the underlying visible matter on the dark halo, fitted with RC data [83]. The top panel shows the fit with dark matter velocity dispersion, $\langle v^2\rangle^{1/2} = 270\ \mathrm{km\,s^{-1}}$ and value of local dark matter density, $\rho_{\mathrm{DM},\odot} \simeq 0.03\ \mathrm{GeV\,cm^{-3}}$, which is the maximum value allowed for 'coupled' case but leads to a poor fit indicated by the $\chi^2$ value (scaled by the degree of freedom (dof) i.e., number of rotation curve data points). The bottom panel shows the fits with $\rho_{\mathrm{DM},\odot} = 0.3\ \mathrm{GeV\,cm^{-3}}$ for various values of $\langle v^2\rangle^{1/2} \geq \langle v^2\rangle^{1/2}_{min} \simeq 330\,\mathrm{km\,s^{-1}}$ for the 'coupled' case. Higher velocity dispersions values are increasingly preferred yielding lesser $\chi^2$ values indicated along with.

value of $\langle v^2 \rangle_{min}^{1/2} \simeq 330\ \mathrm{km\,s^{-1}}$. Fits to the RC data for various values of $\langle v^2 \rangle^{1/2} \geq 330\ \mathrm{km\,s^{-1}}$ (with $\rho_{\mathrm{DM},\odot}$ fixed at $0.3\ \mathrm{GeV\,cm^{-3}}$), are shown in the lower panel of Figure 3.2 along with the corresponding $\chi^2/\mathrm{dof}$ values of the fits. It is seen that reasonably good fits to the RC data would require $\langle v^2 \rangle^{1/2}\ ge\ 450\ \mathrm{km\,s^{-1}}$ or so.

## 3.3 Implications of the Isothermal Halo model of the Galaxy's Dark Matter Halo for the Analysis of Direct Detection Experiments

To calculate the expected DD rates following Equation (2.4), we first need to calculate the velocity integral in Equation (2.5) in the context of the IS halo. The VDF of the IS is Maxwellian in nature extending to $v \to \infty$. For a finite system like our Galactic halo with a finite mass, it is customary for the purpose of calculating the DD event rates to truncate the VDF for the IS system at a chosen value of the local escape speed, $v_{\mathrm{esc}}$. However, then the final PSDF no longer remains a self-consistent solution of the CBE. Here, for simplicity we take the upper limit of the velocity integral in Equation (2.5) as infinity but restrict the minimum velocity required for transferring a kinetic energy ($E_R$) to a recoiling nucleus in the earth's rest frame, $u_{\mathrm{min}}(E_R)$, to be limited to $v_{\mathrm{esc}}$ by using a step function. Under these conditions, the velocity integral, Equation (2.5), has a closed form given by [52],

$$\xi(E_R, t) = \frac{\mathrm{erf}(\mathrm{x_{min}} + \eta) - \mathrm{erf}(\mathrm{x_{min}} - \eta)}{\eta} \times \Theta(v_{\mathrm{esc}} - u_{\mathrm{min}}(E_R)), \tag{3.22}$$

where $x_{\rm min} = \frac{u_{\rm min}}{\sqrt{2}\sigma}$ and $\eta = \frac{v_{\rm E}(t)}{\sqrt{2}\sigma}$ with $u_{\rm min}$ and $v_{\rm E}(t)$ given by Equations (2.3) and (2.10), respectively.

We note here that, for exact calculations, the velocity integral in Equation (2.5) can be considered as a double integral as in Equation (2.7) where the limits on $u_{\rm max}(\cos\theta)$, the maximum WIMP velocity in earth's rest frame, is given by the positive roots of Equation (2.8). However, since we have $v_{\rm max} \to \infty$, this implies $u_{\rm max} \to \infty$ in Equation (2.7) as well. At the same time, the $\Theta$ function in Equation (3.22) restricts the largest allowed value of the lower limit of integration to the finite value of $v_{\rm esc}$. This approximation is reasonable since the tail of the Maxwellian VDF makes only a relatively small contribution to the quantity $\xi(E_R, t)$. With $\xi(E_R, t)$ as given by Equation (3.22), we can calculate the expected event rates using Equation (2.4) by averaging over time in the context of an isothermal DM halo for the Galaxy.

Below we shall analyze several DD experiments considering SI interaction of WIMPs with the nuclei in the context of Galactic DM halo described by an isothermal distribution function. The exact value of DM velocity dispersion, $\langle v^2\rangle^{1/2}$, appearing in the Maxwellian VDF of the IS is not known. From our studies in the previous section, we have seen that good fits to the RC data prefer values of $\langle v^2\rangle^{1/2} \geq 330\ \,{\rm km\,s^{-1}}$ with larger values preferred for better fits. At the same time, the value of $v_{\rm esc}$ is also not precisely known. The RAVE survey [87] has reported values of $v_{\rm esc}$ in the range 498-608 $\,{\rm km\,s^{-1}}$ (at 90 % C.L.), with a mean value of 544 $\,{\rm km\,s^{-1}}$. Given these uncertainties, we shall study the variation of our DD analysis results for different values of $\langle v^2\rangle^{1/2}$ and $v_{\rm esc}$ within the broad range of their values mentioned above. We shall also study the variation of our results with different values of the inelasticity parameter, $\delta$, for the case of inelastic WIMP-nucleus scattering [Equation (2.3)].

### 3.3.1 Direct Detection Experiments Considered

Here we discuss the implications of the isothermal halo model for the results of three "null" experiments namely, CDMS-II [88, 81], CRESST-I [89] and XENON-10 [90, 91], in addition to results reported by DAMA collaboration [68] which has claimed the detection of an annual modulation of the recoil event rates attributable to the WIMPs [3]. In particular we study the compatibility of the DAMA's annual modulation results with the null results of other experiments. This question of compatibility of the DAMA results [68] has also been the subject of several earlier studies including those that take into account the effect of "ion channeling" on the analysis [92, 52, 46] (see below). For simplicity, we shall here consider only the SI case.

*DAMA/NaI and DAMA/LIBRA* :
The DAMA/NaI [69] and DAMA/LIBRA [68] experiments (hereafter together simply referred to as the "DAMA" collaboration) has long been claiming an annual modulation of their event rate based on detection of scintillation signals with radio-pure Sodium Iodide ($^{23}\mathrm{Na}^{127}\mathrm{I}$) target and interpreting the same as an evidence for WIMPs. The DAMA collaboration [69, 68] has reported a non-zero annual modulation amplitude out of the detected recoil event rates over a period of eleven annual cycles [see Figure 3.3], with a total exposure of 0.82 ton-year at a confidence level of 8.2 $\sigma$.

[3] There have been more recent updated results published by the collaborations. However, the analyses presented here with the old versions of the experimental results, should, we believe, be good enough for the purpose of illustrating the effects of the variations of the relevant astrophysical parameters on the results of the various DD experiments.

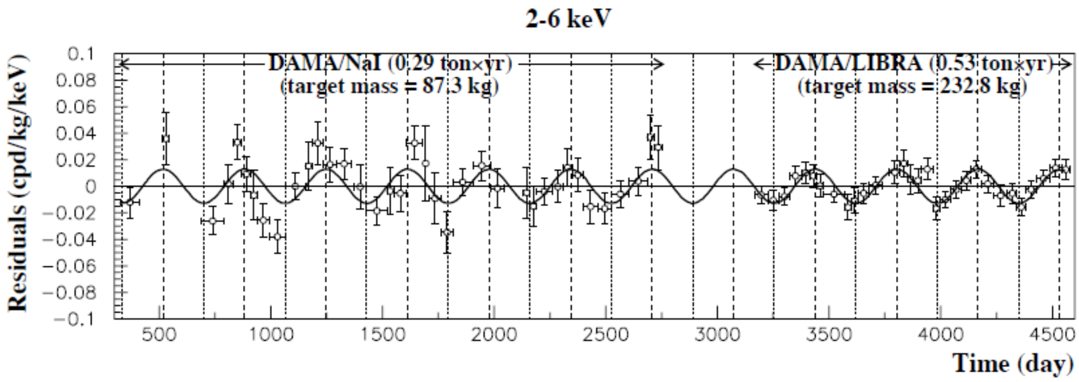


Figure 3.3: The DAMA modulation signal reported for 11 annual cycles with a total exposure of 0.82 ton-year at a confidence level of 8.2 $\sigma$ [68, 69].

This annual modulation is attributed to the periodic variation of Earth's velocity in the Galactic rest frame, $v_{\rm E}$ [see Equation (2.10)], which also results in a periodic variation of the recoil event rates (calculated in the context of the chosen DM halo of the Galaxy) that can be approximately written as [46, 44, 45],

$$\frac{d\mathcal{R}}{dE_R}(E_R, t) \approx S_0(E_R) + S_m(E_R)\cos\omega(t - t_0)\,, \tag{3.23}$$

where $S_0$ is the average recoil rate over a year and $S_m$ is the "modulation amplitude" defined as,

$$S_m(E_R) = \frac{1}{2}\left[\frac{d\mathcal{R}}{dE_R}(E_R,\ \text{June 2}) - \frac{d\mathcal{R}}{dE_R}(E_R,\ \text{Dec 2})\right]. \tag{3.24}$$

A nonzero value of $S_m$ is taken to be a signal for WIMP-induced nuclear recoils.

To compare with experimental data given in specific recoil energy bins, the average value of $S_m$ over a given energy range is calculated as:

$$S_m^{E_1 - E_2} = \frac{1}{E_2 - E_1}\int_{E_1}^{E_2} S_m(E_R)dE_R\,. \tag{3.25}$$

Now, for detectors like DAMA only a part of the recoil energy is detected via the scintillation signal and the rest is lost as phonons. In this case, the actual energy of the recoil nucleus $E_R$ is related to the detectable energy, $E_D$ — often called the "electron-equivalent energy" and denoted by "keVee" – through the relation $E_D = QE_R$, where the "quenching factor" $Q(< 1)$ depends on the nuclear material and characteristics of the detector. For the NaI target, the quenching factors are $Q_{\rm Na} \approx 0.3$ and $Q_{\rm I} \approx 0.09$.

However, as first pointed out by E. M. Drobyshevski [93] and studied in detail in the context of the scintillating NaI material of DAMA detector in [94], for certain energies and incidence angles of the particle (for example, along the crystal axis), the recoiling nucleus transfers energy almost entirely to the electrons (rather than to other nuclei) of the scintillator material. In such a case, called "channeling", one has $Q \approx 1$. We shall use the following simple parametrizations [95], of the fractions of "channeled" events for recoiling Sodium and Iodine nuclei in the DAMA experiment:

$$f_{\rm Na} \simeq \frac{1}{1 + 1.14 E_R(\,{\rm keV})}\,, \quad f_{\rm I} \simeq \frac{1}{1 + 0.75 E_R(\,{\rm keV})}\,. \tag{3.26}$$

Note that the use of 'keVee' is only a bookkeeping device to distinguish the measured energy by the detector from the true recoil energy; the actual unit is still keV.

To take into account the finite energy resolution of the detector, the actually measured energies $E_D$ are usually taken to be normally distributed about the true detectable energy $E'_D$ (i.e., the energy that would be measured if the detector had 100% energy resolution) with a standard deviation $\sigma(E'_D)$. Thus, the measured differential rate is obtained by convolving $\frac{d\mathcal{R}}{dE'_D}$ with a normalized Gaussian with a given standard deviation as,

$$\frac{d\mathcal{R}}{dE_D}(E_D,t) = \frac{1}{\sqrt{2\pi}}\int \frac{dE'_D}{\sigma}\frac{d\mathcal{R}}{dE'_D}e^{-(E_D-E'_D)^2/2\sigma^2}. \tag{3.27}$$

For DAMA, we have the form [96], $\sigma(E'_D) = (0.448\,\mathrm{keV})\sqrt{E'_D/\,\mathrm{keV}} + 0.0091E'_D$ . Thus, the expected modulation amplitude is obtained by convolving Equation (3.24) (after changing the integration variable to $E_D = QE_R$) with a normalized Gaussian with the above standard deviation. The theoretical modulation amplitude over a given interval of measured energy between $E_{D1}$ and $E_{D2}$ is then calculated from Equation (3.25) after the above convolution. The efficiency of the DAMA detector is taken to be unity.

For the analysis of the annual modulation results, we consider the 2-bin data set given by the DAMA collaboration [68], namely, the low-energy bin spanning 2-6 keVee within which a non-zero modulation amplitude is measured and the high energy bin spanning 6-14 keVee in which the modulation amplitude is consistent with zero. Table 3.1 gives the modulation amplitudes ($S_m$) measured by DAMA in these two energy bins.

| Energy ($E_D$ in keVee) | Modulation Amplitude ($S_m$) (counts/day/kg/keVee) |
|---|---|
| 2 - 6 | 0.0131 $\pm$ 0.0016 |
| 6 - 14 | 0.0009 $\pm$ 0.0011 |

Table 3.1: DAMA modulation amplitude data reported from event rates collected for 11 annual cycles [68].

With the theoretically expected modulation amplitude in the $k$-th energy bin, $S^{\rm th}_{m,k}$, calculated as described above, a $\chi^2$ fit to the corresponding experimental modulation amplitude data given in Table 3.1 is calculated as

$$\chi^2 \equiv \sum_k \left( \frac{S_{m,k} - S^{\rm th}_{m,k}}{\sigma_k} \right)^2 , \tag{3.28}$$

where $S_{m,k}$ is the experimentally measured modulation amplitude in the $k$-th energy bin and $\sigma_k$ the corresponding error in the experimental value. In this simple analysis procedure, there are only two free parameters in the problem, namely, the WIMP mass ($m_\chi$) and the relevant WIMP-nucleon cross section ($\sigma_{\chi-nucleon}$) [4]. For a given value of $m_\chi$, we find $\chi^2_{\rm min}$ (the minimum value of $\chi^2$) by scanning over the values of $\sigma_{\chi-nucleon}$. The 90% C.L. allowed region of the relevant cross section, for the given value of $m_\chi$, is then found by accepting those values of $\sigma_{\chi-nucleon}$ for which $\chi^2 - \chi^2_{\rm min} \leq 2.71$, with $\chi^2_{\rm min} < 2$.

*Experiments giving null results* :

These experiments can be divided into two classes: those which report no events at all (after all the relevant cuts are employed), and those which report events (after analysis cuts) but ascribe them to background. In both cases, we follow the simple analysis procedure outlined in Ref. [52].

For experiments reporting zero events after relevant analysis cuts, we calculate a 90% C.L. one sided upper limit for $\sigma_{\chi-nucleon}$ for a given $m_\chi$ by using Poisson statistics. We demand that the theoretically predicted number of events, $N$, over the entire energy range of interest be such as to allow a Poisson probability of

[4] Here, we are only considering SI WIMP-nucleus interactions, therefore, $\sigma_{\chi-nucleon} \equiv \sigma^{SI}_{\chi-nucleon}$

observing j(= zero) events as bad as 10% but not worse. This corresponds to the Poissonian probability,

$$\frac{N^j}{j!}\exp(-N) = 0.1, \tag{3.29}$$

which is solved to get $N(m_\chi, \sigma_{\chi-nucleon}) = 2.3$.

For experiments that report non-zero events after analysis cuts but attribute those events to background, a simplified version of Yellin's [97] optimum interval method [52] is used. Here, we again calculate, for a given mass $m_\chi$, and for all contiguous combination of energy bins, the 90% C.L. upper limit allowed theoretically expected number of events $N(m_\chi, \sigma_{\chi-nucleon})$ corresponding to the observed number of events $n$ dictated by Poisson statistics as,

$$\sum_{j=0}^{j=n} \frac{N^j}{j!}\exp(-N) = 0.1. \tag{3.30}$$

We then choose the most stringent (i.e., the lowest) value of $\sigma_{\chi-nucleon}$ so obtained by comparing the values from all the bins. A reference table for the mean value, $N$, for a Poisson variable $n$ is given in [98].

In both the above mentioned cases, the procedure discussed above allows us to generate the exclusion plot in the $m_\chi$-$\sigma_{\chi-nucleon}$ parameter space, such that regions above the exclusion curves are disallowed for WIMPs.

The experiments considered for analysis are as follows:-

CDMS-II (Ge) [81] :

The CDMS-II collaboration [81] had reported two candidate events at recoil energies 12.3 keV and 15.5 keV after applying all cuts in the 10-100 keV window of their "signal region" with an estimated probability of $\sim$ 23% of observing 2 or more background events in that region, for the estimated level of the background. With such a high value of the estimated background probability, these events were ascribed to background. The total effective exposure, for CDMS-II experiment used in our calculations below, includes the spectrum-averaged equivalent exposure of $\approx 194.1$ kg-days (for a WIMP mass of $\sim 60\,\mathrm{GeV\,cm^{-3}}$) [81] combined with that of CDMS-II collaboration's previous published paper [99] of $\sim 110.4$ kg-days (after reduction of the figure quoted in [99] by a factor of $\sim 9\%$ due to improved estimate of their detector mass [81]). The above figures include the approximately constant (in energy) detector efficiency of $\sim 30\%$ [81] already folded in. We obtain 90% C.L. upper limits on the relevant WIMP cross section as a function of WIMP mass using the simplified version of Yellin's optimum interval method [97] described above. In this analysis we have used a minimum recoil energy bin width of 5 keV.

CDMS-II (Si) [88] :

This experiment employs high purity silicon crystals as the detector material. No events passed all the data analysis cuts. We derive 90% C.L. upper limit on the relevant cross section as a function of the WIMP mass by using Poisson statistics discussed above, i.e., by demanding that, for a given WIMP mass $m_\chi$, the upper limit of the cross section yields 2.3 expected events.

CRESST-I [89] :

The Phase I of the CRESST experiment employed sapphire ($Al_2O_3$) detectors with an exposure of 1.51 kg-days over an energy range of 0.6-20 keV. After all the relevant analysis cuts, all the observed events were finally ascribed to background. We take into account the energy resolution of the detector described by a Gaussian distribution of the measured energies around the true value with a standard deviation $\sigma(E_R) = \sqrt{(0.220\,\mathrm{keV})^2 + (0.017 E_R)^2)}$ [89] [5]. Upper limits were obtained similar to CDMS-II (Ge) analysis with a smallest allowed energy-interval width of 1.2 keV [89].

XENON-10 [90, 91] :
XENON-10 is a dual phase time projection chamber employing liquid Xenon as target material and uses the ratio of ionization to scintillation yield for discriminating between the dominant electron recoil background and searched for nuclear recoil WIMP signal over a nuclear recoil energy range of $\sim$ 6.1-36.5 keV. A total of 10 events were recorded in the WIMP signal region for a total effective exposure of about 136 kg-days after analysis cuts. We obtain 90 % C.L. upper limits on the relevant WIMP cross section as a function of WIMP mass using the simplified version of Yellin's optimum interval method described earlier.

Table 3.2 summarizes the relevant features of the experiments considered above. Further details of each experiment can be found in the cited References.

| Experiment | Target | Mass no (A) | Effective exposure (kg-days) | Threshold ( keV) |
|---|---|---|---|---|
| CDMS-II [81] | Ge | 73 | 304.5 | 10 |
| CDMS-II [88] | Si | 28 | 12.1 | 7 |
| CRESST-I [89] | $Al_2O_3$ | 27 (Al) & 16 (O) | 1.51 | 0.6 |
| XENON-10 [90, 91] | Xe | 131 | 136 | 6.1 |

Table 3.2: Relevant features of the experiments (exposures relevant for spin-independent WIMP-nucleus interactions only) considered for generating exclusion plots in the WIMP mass vs WIMP-nucleon cross section plane.

[5] Reference [89] actually quotes their energy resolution in terms of the FWHM, $\Delta E_R{}^{\mathrm{FWHM}}$, which is related to the standard deviation $\sigma$ by $\Delta E_R{}^{\mathrm{FWHM}} \approx 2.354\sigma$.

### 3.3.2 Implications for the WIMP parameters

We now present the results of our analyses of the DD experiments discussed above considering SI interaction of WIMPs with the nuclei in the context of the isothermal Galactic DM halo model described in Section 3.1.

Figure 3.4 shows exclusion curves in the $m_\chi - \sigma_{\chi-nucleon}$ plane derived from the null results of different DD experiments considered above with $\rho_{\rm DM,\odot} = 0.3$ $\mathrm{GeV\,cm^{-3}}$ under elastic SI scattering ($\delta = 0$) cases with four different values of the DM velocity dispersion [6], $\langle v^2 \rangle^{1/2}$ along with the closed parameter space in the same plane implied by the annual modulation of the event rates seen by the DAMA experiment. The value of local $v_{\rm esc}$ has been taken to be 544 $\mathrm{km\,s^{-1}}$, the mean value as reported by the RAVE Survey [87]. It is seen that the region in the $m_\chi - \sigma_{\chi-nucleon}$ plane, where the DAMA results are compatible with the null results of other experiments (the “DAMA compatible” regions) shrinks with higher values of $\langle v^2 \rangle^{1/2}$. Particularly, for the SHM case (see top-left panel of Figure 3.4), it is found that there exists a region of the parameter space bounded by, $2.8 \lesssim m_\chi \lesssim 11.8\,\mathrm{GeV}$ and $7.3 \times 10^{-6} \lesssim \sigma_{\chi-nucleon} \lesssim 4.8 \times 10^{-3}$ pb, within which DAMA’s claimed modulation signal is compatible with the parameter space allowed by the other experiments under SI elastic scattering. Simply by changing the velocity dispersion to a value of 550 $\mathrm{km\,s^{-1}}$ (keeping other parameters same), for example, the DAMA compatible region (see bottom-right panel of Figure 3.4) changes to $5.2 \lesssim m_\chi \lesssim 6.8\,\mathrm{GeV}$ and $1.0 \times 10^{-4} \lesssim \sigma_{\chi-nucleon} \lesssim 9.8 \times 10^{-4}$ pb.

Next, in Figure 3.5, we compare the DAMA compatible regions in the $m_\chi - \sigma_{\chi-nucleon}$ plane for $v_{esc}$ spanning between 500-600 $\mathrm{km\,s^{-1}}$, covering the

[6] $\langle v^2 \rangle^{1/2} = 270$ $\mathrm{km\,s^{-1}}$ refers to the SHM case.

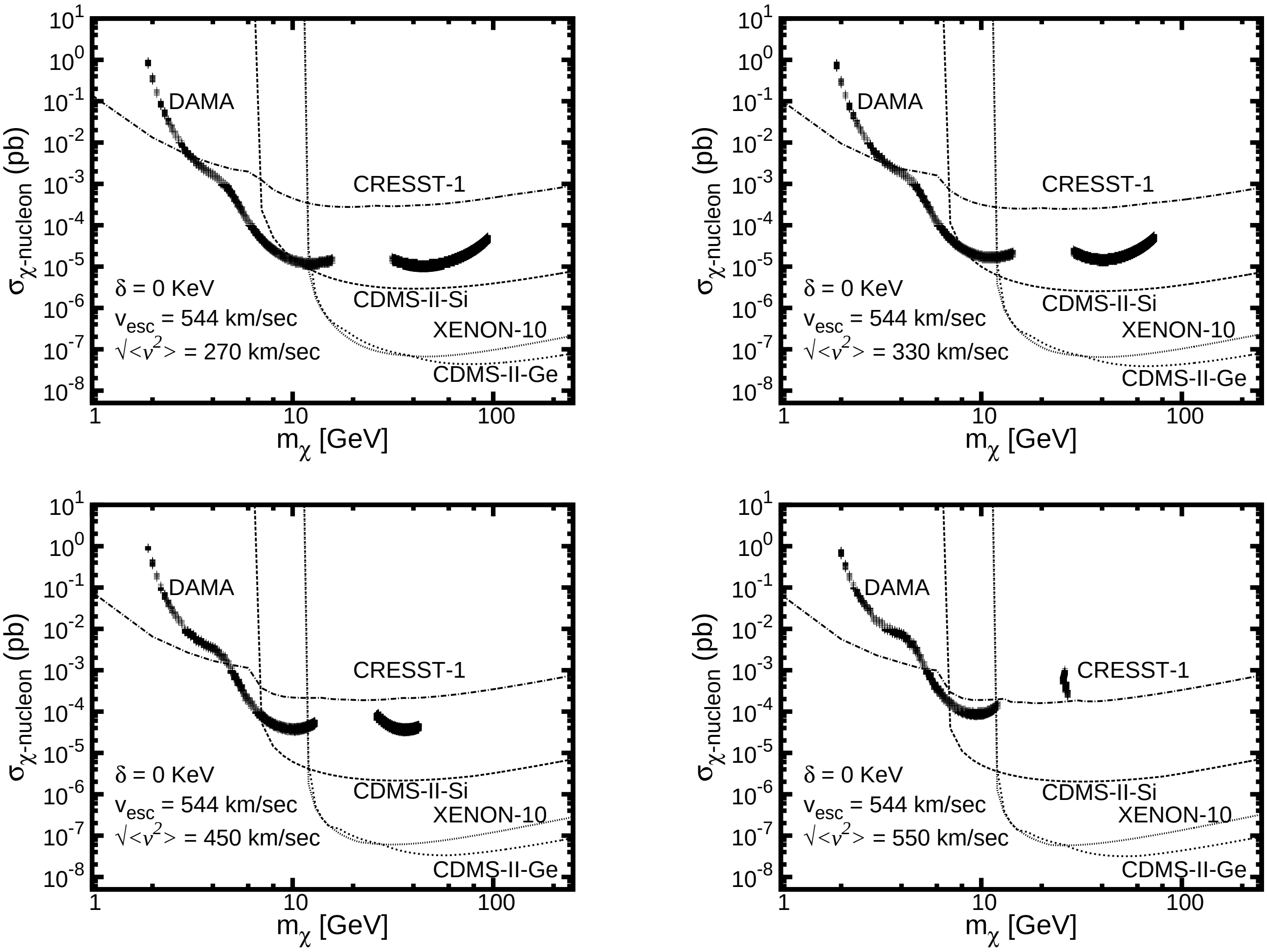


Figure 3.4: DAMA implied ranges of values of WIMP mass, $m_\chi$, and WIMP-nucleon cross-section, $\sigma_{\chi-nucleon}$ superposed on the exclusion curves from the null results of various experiments in the $m_\chi - \sigma_{\chi-nucleon}$ plane, for the case of SI elastic (inelasticity parameter, $\delta = 0$) scattering for an isothermal DM halo of our Galaxy. The four panels corresponds to four different values of DM velocity dispersions, $\langle v^2 \rangle^{1/2}$, as indicated of the isothermal halo model. The values of $\rho_{\rm DM,\odot}$ and $v_{\rm esc}$ have been kept fixed at 0.3 $\mathrm{GeV\,cm^{-3}}$ and 544 $\mathrm{km\,s^{-1}}$, respectively.

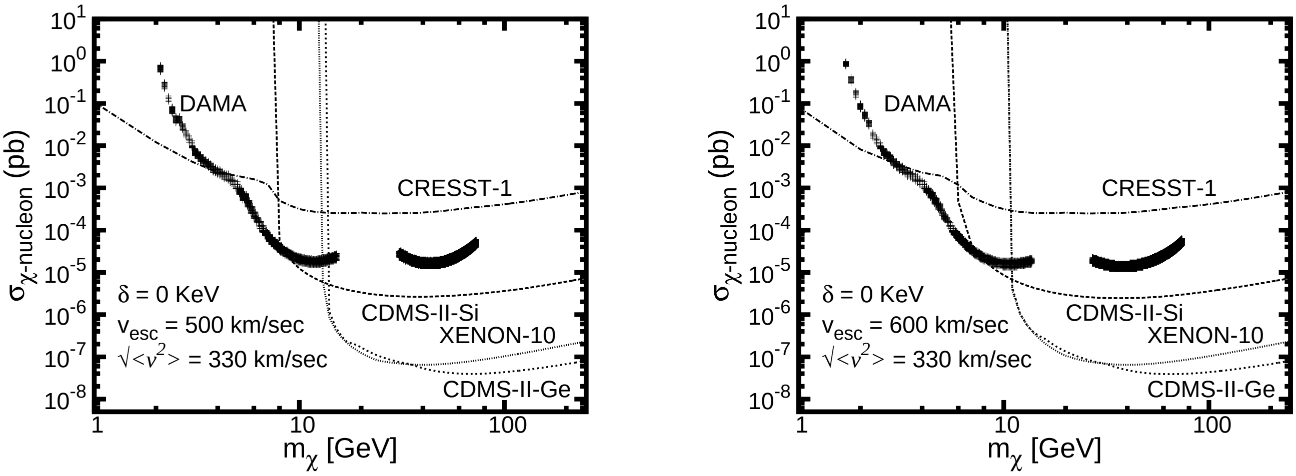


Figure 3.5: Same as top right of Figure 3.4, but for two different local escape velocity, ($v_{\rm esc}$) values as indicated.

extremities of the 90 % C.L. range of $v_{\rm esc}$ reported by the RAVE survey [87], for a DM $\langle v^2\rangle^{1/2} = 330\ \ {\rm km\,s^{-1}}$ (the lowest value allowed for the 'coupled' case; see Section 3.2) with $\rho_{\rm DM,\odot} = 0.3\ \ {\rm GeV\,cm^{-3}}$ and for elastic ($\delta = 0$) SI scattering. It is seen that the results are not strongly sensitive to the variation of $v_{esc}$ within its range of values considered.

Figure 3.6 shows the DAMA compatibility regions as in the previous two figures, but for the case of inelastic SI scattering of WIMPs with the nuclei for various values of the inelasticity parameter, $\delta$. The rest of the halo parameters taken are $\langle v^2\rangle^{1/2} = 330\ \ {\rm km\,s^{-1}}$, $\rho_{\rm DM,\odot} = 0.3\ \ {\rm GeV\,cm^{-3}}$ and $v_{esc} = 544\ \ {\rm km\,s^{-1}}$. We see that the DAMA compatible region changes significantly with values of $\delta$.

Note that, though we have not explicitly included the effect of variation of $\rho_{\rm DM,\odot}$ on the analysis results, its effect is basically an overall scaling of the cross-sections in inverse proportion manner to the value of $\rho_{\rm DM,\odot}$, except for WIMP masses $\ll$ mass of the target nuclei, as discussed further in the next chapter in the context of a more realistic finite-size model of the Galactic DM halo.

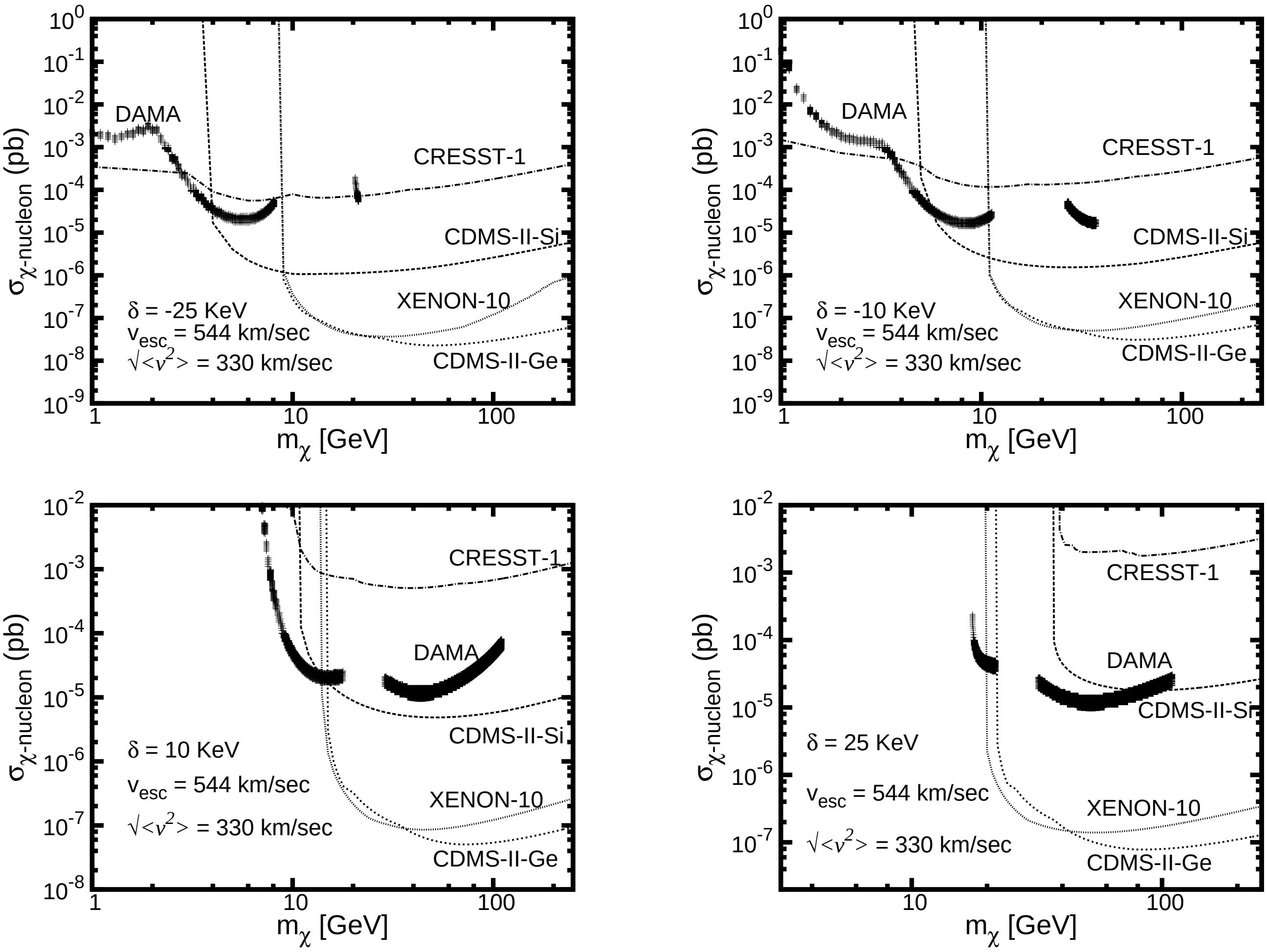


Figure 3.6: Same as top right of Figure 3.4, but for four different inelasticity parameter, $\delta$, values as indicated.

## 3.4 Summary

The VM is the dominant mass component in the inner regions of the Galaxy up to the Solar distance $\sim 8.5$ kpc. The DM controls the gravitational dynamics of the Galaxy only at larger galactocentric distances. As such, it is important to include the effect of gravitational influence of the VM on the phase space distribution of the DM particles.

In this chapter, we have studied the IS model of the Galactic DM halo including the effect of gravitational influence of the observed VM on the phase space distribution of the DM particles constituting the halo. We have studied how the resulting model fits the RC data of the Galaxy. We have seen that with the effect of the VM on DM phase space structure included in a self-consistent manner, the DM velocity dispersion $\langle v^2\rangle^{1/2} \simeq 270\ \mathrm{km\,s^{-1}}$ assumed in the SHM, is incompatible with a value of $\rho_{\mathrm{DM},\odot} = 0.3\ \mathrm{GeV\,cm^{-3}}$ and a minimum value of velocity dispersion, $\langle v^2\rangle^{1/2}_{min} \simeq 330\ \mathrm{km\,s^{-1}}$ is required to support values of $\rho_{\mathrm{DM},\odot} = 0.3\ \mathrm{GeV\,cm^{-3}}$. Indeed, we have seen that a $\langle v^2\rangle^{1/2} \geq 450\ \mathrm{km\,s^{-1}}$ is preferred for a reasonably good fit to the RC data.

We then studied the compatibility of the DAMA annual modulation data [68] with the null results of several other experiments, viz., CDMS-II (Ge and Si targets) [88, 81], CRESST-I [89] and XENON-10 [90, 91] in the context of an IS as the chosen halo model in the case of WIMP-nucleus SI interaction. The DAMA compatible region in the $m_\chi - \sigma_{\chi-nucleon}$ plane depends significantly on the value of DM velocity dispersion, $\langle v^2\rangle^{1/2}$. In particular the compatibility region shrinks as the value of $\langle v^2\rangle^{1/2}$ is made larger. In addition, the compatibility region also depends significantly on the inelasticity parameter, $\delta$. Our results underscore the important fact that a proper determination of parameters of the PSDF of the DM particles constituting the halo of the Galaxy using observational data plays a crucial role in interpreting the results of DD experiments. In addition, the nature of the WIMP-nucleus scattering process ( elastic or inelastic) is also important.

# Chapter 4

# A Self-consistent Truncated Isothermal Model for the Milky Way's Dark Matter Halo

## 4.1 Introduction

In the previous chapter, we have discussed the 'standard halo' model (SHM), which is customarily chosen as the DM halo model for analyzing the direct detection (DD) experiments searching for the Weakly Interacting Massive Particle (WIMP) candidates of dark matter (DM) . Although this model serves the purpose of analysis, it has several drawbacks. It is therefore necessary to consider improved astrophysical models for our Galactic halo.

The SHM suffers from some serious shortcomings. The basic reason is that the density varies as $r^{-2}$ at higher radii which implies that the halo mass varies as as $\sim r$ and therefore diverges as $r \to \infty$. Clearly, such a system cannot represent a realistic DM halo of finite physical size. Secondly, the maximum velocity of the Maxwellian velocity distribution of a SHM extends to infinity. However, for a Galaxy of finite mass and extent, we expect that DM particles can have velocities only up to a certain finite value in order for it to remain bound within the system. Therefore, it is a standard practice, in the context of studying the phenomenology of DD experiments, to truncate the Maxwellian speed distribution at some chosen value of the local escape speed. However, this is not a self-consistent procedure because the resulting phase space structure with a "truncated Maxwellian" speed distribution does not satisfy the steady-state collisionless Boltzmann equation (CBE). Also, the circular rotational speed ($V_c$) in the 'isothermal sphere' (IS) model of the phase space distribution function (PSDF) describing the SHM increases linearly for small $r$, has an oscillatory dependence on $r$ for intermediate $r$, and tends to a constant only asymptotically as $r \to \infty$ (see Figure 3.1). Thus, there is no particular reason why $V_c(\infty)$ should be equal to $V_c(R_0)$ as is done to fix the DM velocity dispersion $\langle v^2 \rangle^{1/2} = 270\ \mathrm{km\,s^{-1}}$ for SHM. In addition, considering the significant uncertainty in $\rho_{\mathrm{DM},\odot}$, there is no strong reason to set the value specifically at $0.3\ \mathrm{GeV\,cm^{-3}}$. Further, in the usual treatment of SHM, the gravitational influence of visible matter (VM) on DM particles is generally not taken into account and the system is assumed to be an isolated DM halo. As we have seen in the previous chapter, inclusion of the effect of VM substantially changes the values of the $\langle v^2 \rangle^{1/2}$ required to fit the rotation curve (RC) data. Indeed, we have seen there that a value of $\rho_{\mathrm{DM},\odot} \simeq 0.3\ \mathrm{GeV\,cm^{-3}}$ is inconsistent with $\langle v^2 \rangle^{1/2}$ of $270\ \mathrm{km\,s^{-1}}$ as is customarily adopted in the context of SHM description of Galactic halo.

There are indeed well understood phase space structures that allow truncation of the DM halo at a finite radius and the velocity distribution at appropriate limits in a self-consistent manner as will be studied in this chapter. Here, we adopt such a model of the phase-space structure of the WIMPs constituting the DM halo with finite-size and mass and study its implications for the analysis of the results of the same set of DD experiments as analyzed in Chapter 3 (done there in the context of the IS model for DM halo). This model is based on describing the PSDF of the WIMPs constituting a spherically symmetric DM halo of the Galaxy by the so-called “lowered” (or “truncated”) isothermal model (often called “King” model) [43]. This PSDF, again depends only on the specific energy, $E$, of the system, and is thus characterized by an isotropic velocity distribution function (VDF). By Jean's theorem (see Section 3.1), it is therefore a steady state solution of the CBE. In this model, at every location $\mathbf{x}$ within the system, a DM particle can have speeds up to a maximum finite value of $v_{\max}(\mathbf{x})$, which is self-consistently determined by the model itself. A particle of velocity $v_{\max}(\mathbf{x})$ at $\mathbf{x}$ within the system can just reach its outer boundary, generally called the truncation radius ($r_t$), where the DM density by construction vanishes. As will be seen below, the speed distribution of the particles constituting a King model can be described as “quasi-Maxwellian” by nature. When the VM density is set to zero and the truncation radius is set to infinity, this halo model reduces to a single-component IS as used for SHM described in the previous chapter.

In the following sections, first we present the basic formalism of the King model as a description of the Galactic DM halo and then obtain the best fit parameters of the model by fitting to the RC data of the Galaxy considering self-consistent gravitational coupling to the underlying VM distribution in the Galaxy. We demonstrate the effect of VM on the halo density profiles and present the mass and maximum speed profiles and local VDFs of the DM particles for the best fit halo parameters. Finally, we study the implications of the King model as the Galaxy's DM halo for the analysis of the results of several DM DD experiments considering elastic scattering of WIMPs with target nuclei under spin-independent (SI) and spin-dependent (SD) interactions with the detector nucleus and summarize at the end. A comparison is also drawn with the results obtained in the context of SHM in the previous chapter, for the sake of completeness.

## 4.2 The Basic Formalism of King Model

To describe a "nearly isothermal" system of finite size and finite total mass, one must have, in addition to the two parameters of the IS halo model, a parameter that characterizes the finite size of the system. This is accomplished in the context of a King model by taking the PSDF of the WIMPs in the Galactic halo to be of the following form [43]:

$$f(\mathbf{x},\mathbf{v}) \equiv f(\mathcal{E}) = \begin{cases} \rho_1(2\pi\sigma^2)^{-3/2}\left(e^{\mathcal{E}/\sigma^2}-1\right) & \text{for } \mathcal{E} > 0\,, \\ 0 & \text{for } \mathcal{E} \leq 0\,, \end{cases} \tag{4.1}$$

where

$$\mathcal{E}(\mathbf{x}) \equiv \mathcal{C} - \left(\frac{1}{2}v^2 + \Phi(\mathbf{x})\right) \equiv \Psi(\mathbf{x}) - \frac{1}{2}v^2\,, \tag{4.2}$$

is the so-called "relative energy" and $\Psi(\mathbf{x})\,(\equiv -\Phi(\mathbf{x}) + \mathcal{C})$ the "relative potential" [43]. The three (constant) parameters of the model are $\rho_1$ (with dimension of density), $\sigma$ (with dimension of velocity) and the new parameter $\mathcal{C}$

(with dimension of potential or squared velocity) which is related to the finite size of the system (see below) and is chosen such that $f(\mathcal{E}) > 0$ for $\mathcal{E} > 0$ and $f(\mathcal{E}) = 0$ for $\mathcal{E} \leq 0$.

The density at any position $\mathbf{x}$ is obtained by integrating $f(\mathbf{x}, \mathbf{v})$ over all velocities giving

$$\rho_{\rm DM}(\mathbf{x}) \quad = \quad \frac{\rho_1}{(2\pi\sigma^2)^{3/2}} \int_0^{\sqrt{2\Psi(\mathbf{x})}} dv\, 4\pi v^2 \left[\exp\left(\frac{\Psi(\mathbf{x}) - v^2/2}{\sigma^2}\right) - 1\right], \tag{4.3}$$

which, in closed form appears as,

$$\rho_{\rm DM}(\mathbf{x}) \quad = \quad \rho_1 \left[\exp\left(\frac{\Psi(\mathbf{x})}{\sigma^2}\right) \mathrm{erf}\left(\frac{\sqrt{\Psi(\mathbf{x})}}{\sigma}\right) - \sqrt{\frac{4\Psi(\mathbf{x})}{\pi\sigma^2}}\left(1 + \frac{2\Psi(\mathbf{x})}{3\sigma^2}\right)\right]. \tag{4.4}$$

Given the expressions for PSDF and density, the normalized (to unity) velocity distribution of the DM particles, at the given location $\mathbf{x}$ can be obtained as,

$$f_{\mathbf{x}}(v) \equiv \frac{4\pi v^2}{\rho_{\rm DM}(\mathbf{x})} f(\mathbf{x}, \mathbf{v}), \tag{4.5}$$

where $f(\mathbf{x}, \mathbf{v})$ and $\rho_{\rm DM}(\mathbf{x})$ are given by Equations (4.1) and (4.4), respectively.

For convenience, we replace the parameter $\rho_1$ in Equation (4.1) and (4.4) by the value of the DM density at the Solar location, $\rho_{{\rm DM},\odot}$, and rescale the expressions accordingly.

The King model approaches the IS solution at small radii $r = |\mathbf{x}|$, but have density profiles that fall off faster than that of the IS halo model at large radii (which makes the total mass finite). Indeed, the density vanishes at $r = r_t$, the truncation radius where $v_{\rm max} = 0$, representing the outer edge of the system. This is ensured by choosing:

$$\mathcal{C} = \Phi(r_t)\,, \quad \text{so that } \Psi(r_t) = -\Phi(r_t) + \mathcal{C} = 0\,. \tag{4.6}$$

As evident from Equation (4.6), the parameter $\mathcal{C}$ fixes the finite size, $r_t$, of the system.

Note also that, unlike in the case of the (infinite) IS halo model, the parameter $\sigma$ in the King model is *not* equal to the one-dimensional velocity dispersion of the particles constituting the system; the latter can be calculated for the DF given above and is a function of $r$ (again unlike IS halo), vanishing at $r = r_t$. In fact, unlike in the case of the Maxwellian DF, for which the velocity dispersion is linearly related to the most probable speed of the particles of the system, there is no simple relation between the velocity dispersion and the most probable speed of the particles of the system described by a skewed velocity distribution in the context of a King model type DM halo; see below.

At any location $\mathbf{x}$ the maximum speed a particle of the system can have is,

$$v_{\max}(\mathbf{x}) = \sqrt{2\Psi(\mathbf{x})}\,, \tag{4.7}$$

and for $v \geq v_{\max}$ the relative energy $\mathcal{E} \leq 0$ in Equation (4.2) and, as a consequence, the VDF in Equation (4.5) vanishes too.

The usual escape speed at any location, $v_{\rm esc}(\mathbf{x})$, which is in general larger than $v_{\max}(\mathbf{x})$, is defined as the speed required for a particle to escape from the given location out to infinity. It can be expressed as $v_{\rm esc}^2(\mathbf{x}) = 2\,[\Phi(\infty) - \Phi(\mathbf{x})]$. For a King model DM halo of finite size, it is the maximum speed (at the Solar neighborhood) and not the escape speed that is relevant in considerations of DD experiments.

It is crucial to note that, in presence of VM a test particle responds to not only the potential due to DM but it senses the sum of gravitational potentials due to both DM and VM components. The methodology to account for this 'coupled' situation has been described in the previous chapter. Therefore, the $\Psi(\mathbf{x})$ appearing in the expressions for PSDF and DM density [Equations (4.1) and (4.4)] is explicitly,

$$\Psi(\mathbf{x}) = \Phi_{\rm tot}(|\mathbf{x}| = r_t) - \Phi_{\rm tot}(\mathbf{x}), \tag{4.8}$$

where,

$$\Phi_{\rm tot}(\mathbf{x}) = \Phi_{\rm DM}(\mathbf{x}) + \Phi_{\rm VM}(\mathbf{x}). \tag{4.9}$$

## 4.3 Rotation Curve fit to King Model

To calculate the circular speed, $V_c(R)$, as a function of the galactocentric distance $R$ [see Equation (3.11)], we need to solve the Poisson's equations [see Equation (3.12)] numerically for the gravitational potentials of VM and DM from respective density profiles under boundary conditions given in Equation (3.13). The $\rho_{\rm VM}(\mathbf{x})$ is the known VM density of the Galaxy given by Equation (3.14) and (3.15) and $\rho_{\rm DM}(\mathbf{x})$ for King model has been defined already in the previous section in Equation (4.4). Therefore, the Poisson equation for the VM part is solved numerically with the given $\rho_{\rm VM}(\mathbf{x})$, whereas that for DM is a coupled non linear equation and is solved by an iterative procedure described in the previous chapter (see Section 3.2) in the context of an isothermal halo. It generates a three-parameter $(r_t\,, \sigma\,, \rho_{\rm DM,\odot})$ family of self-consistent solutions to $\Phi_{\rm DM}(\mathbf{x})$ and

$\rho_{\text{DM}}(\mathbf{x})$ under the chosen boundary conditions.

The theoretical RC is calculated for three different values of $\rho_{\text{DM},\odot}$, namely, $0.2\,, 0.3$ and $0.4$ GeV cm$^{-3}$, in each case with a wide range of values of the other two King model parameters $r_t$ and $\sigma$ and with the VM parameters fixed as before in the previous chapter. These two parameters of the model are then determined by fit to the RC data of the Galaxy.

We adopt the RC data given by Xue et al. [6], which extends up to a galactocentric distance ($R$) of $\sim 60\,\text{kpc}$ starting from $R \geq 7.5\,\text{kpc}$. This set of RC data is derived from comparison of cosmological simulations with the kinematical data of a sample of $\sim$ 2400 blue horizontal-branch (BHB) stars taken from the Sloan Digital Sky Survey (SDSS) DR6 [100] database. The RC given by Xue et al. gently falls from the adopted value at the Sun's location, $V_0 \approx 220\,\text{km}\,\text{s}^{-1}$, to $\sim 180\,\text{km}\,\text{s}^{-1}$ at $\sim 60\,\text{kpc}$. The RC data for $R < 7.5\,\text{kpc}$ are taken from Ref. [83]. To asses the degree of fit, the $\chi^2$-test statistic is used as defined in Equation (3.20).

Figure 4.1 shows our theoretically calculated RC for the Galaxy with its DM halo described by the King model DF, Equation (4.1), and including the gravitational effect of the VM distribution in a self-consistent manner, for three different sets of values of the King model parameters $(r_t, \sigma, \rho_{\text{DM},\odot})$ as indicated. The RC profiles are shown for $\rho_{\text{DM},\odot} = 0.2\,, 0.3$ and $0.4\,\text{GeV}\,\text{cm}^{-3}$, and in each case, the shown theoretical curve corresponds to the values of the other two parameters ($r_t$ and $\sigma$) and the $\chi^2$ values (scaled by the degree of freedom (dof) i.e., number of rotation curve data points) that yield best fit (giving lowest $\chi^2$/dof) to the adopted RC data of the Galaxy.

For the range of King model density parameter considered

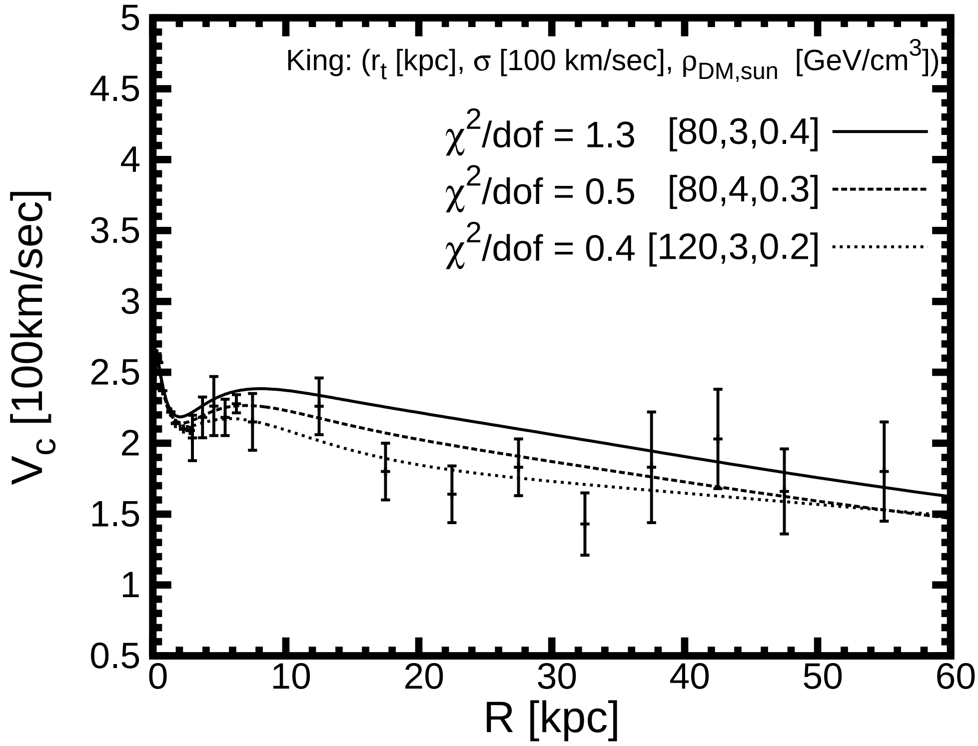


Figure 4.1: Rotation curves for the Galaxy with its dark matter halo described by the King model by including the gravitational effect of the visible matter in a self-consistent manner, for three different sets of values of the King model parameters viz. truncation radius, velocity parameter and local dark matter density, $(r_t\,, \sigma\,, \rho_{\rm DM,\odot})$, as indicated. The curves are shown for three different values of $\rho_{\rm DM,\odot}$, and in each case, the curve shown corresponds to the values of the other two parameters ($r_t$ and $\sigma$) and the corresponding $\chi^2$ values (scaled by the degree of freedom (dof) i.e., number of rotation curve data points) that yield best fit to the rotation curve data of the Galaxy [83, 6].

($0.2 \leq \rho_{\mathrm{DM},\odot} \leq 0.4\,\mathrm{GeV\,cm^{-3}}$), the "global" best fit to the RC data (giving globally lowest value of $\chi^2/\mathrm{dof}$) is obtained for the King model DM parameter set $\rho_{\mathrm{DM},\odot} = 0.2\,\mathrm{GeV\,cm^{-3}}$, $r_t = 120\,\mathrm{kpc}$ and $\sigma = 300\,\mathrm{km\,s^{-1}}$ (the dotted curve in Figure 4.1). The best fit local $V_0$ is found to be 232 $\mathrm{km\,s^{-1}}$ in the context of this model. The separate contributions of the VM and the DM components to the total RC and the total mass of the Galaxy for the "best-fit" set of parameter values are shown in Figure 4.2.

The mass of a generalized system with azimuthal symmetry with given density profile, $\rho(r,\theta)$, can be calculated as,

$$M(\leq r) = \int_{\cos\theta=-1}^{+1} \int_0^r 2\pi r'^2 dr' d(\cos\theta) \rho(r',\theta). \tag{4.10}$$

It is of interest to note that the DM halo mass for the best-fit model obtained above, $M_{\mathrm{DM}}(\leq r_t) \sim 1.3 \times 10^{11}\,M_\odot$, is only about a factor of $\sim 1.5$ times larger than the total VM mass, $M_{\mathrm{VM}}(\leq r_t) \sim 8.4 \times 10^{10}\,M_\odot$, giving a total Galaxy mass of $\sim 2.1 \times 10^{11}\,M_\odot$ within $r_t$. Actually, this is fairly independent of the exact values of the VM model parameters adopted as long as those parameters are such that the VM by itself gives the dominant contribution to the RC data at inner Galactic regions. The main reason for the relatively low DM halo mass is the *declining nature of the adopted RC data* beyond the Solar circle. Note that the values of the truncation radius and other physical quantities derived here are in the context of a specific model of the DM halo fitted to a RC data extending up to $\sim 60$ kpc only. In recent past, RC data for Galaxy extended up to several hundreds of kpc have been put forward by different groups [7, 8] and it is worth investigating the halo properties in the light of these data sets (See Chapters 6 and 7 for details).

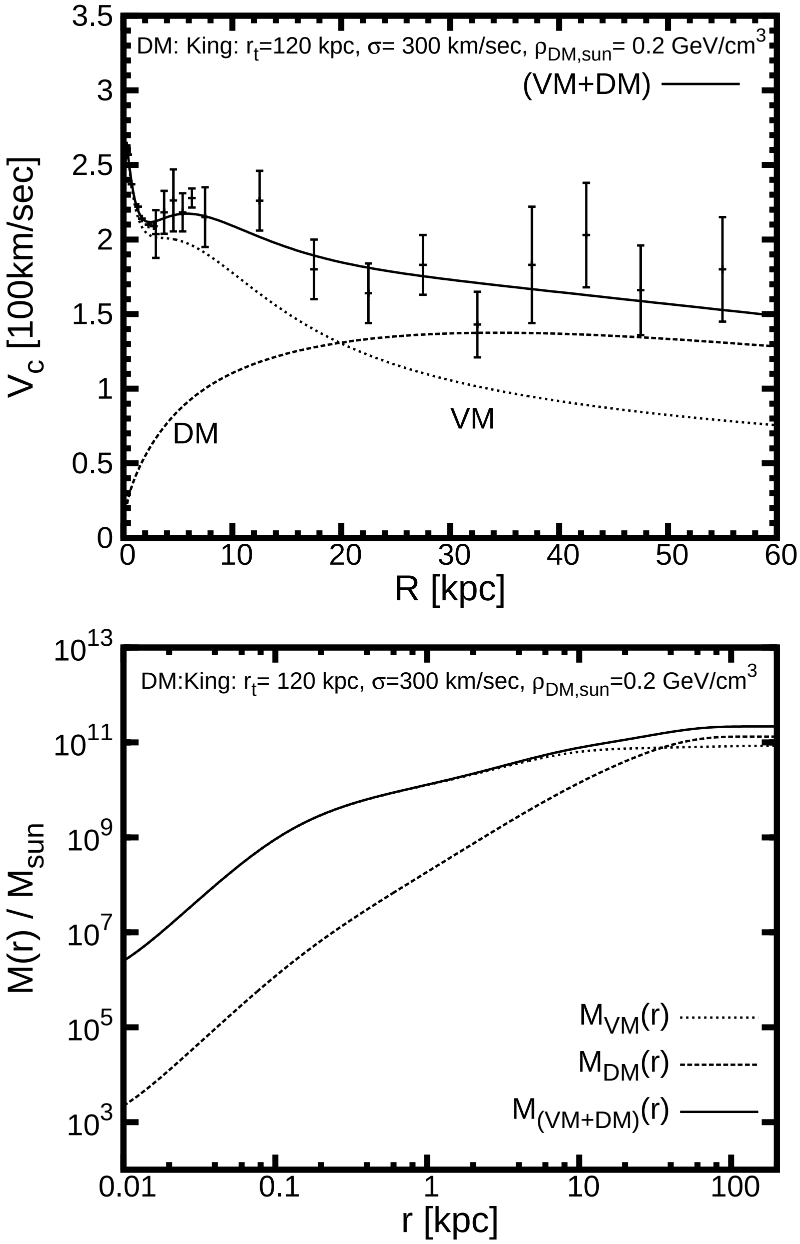


Figure 4.2: The contributions of the visible and dark matter components to the rotation curve data (top panel) and total mass (bottom panel) of the Galaxy for the best-fit King model parameters giving local dark matter density $\rho_{\rm DM,\odot} = 0.2\,{\rm GeV\,cm^{-3}}$, truncation radius $r_t = 120\,{\rm kpc}$ and velocity parameter $\sigma \simeq 300\,{\rm km\,s^{-1}}$ for the 'coupled' case are shown. The rotation curve data of the Galaxy has been adopted from Ref. [83, 6].

## 4.4 Dark Matter Density Profile

In the ‘coupled’ case, the main effect of the gravitational influence of the VM on the DM halo is to “pull in” the DM particles towards the center of the halo leading to an increased central concentration and reduced core radius of the DM density profile. Here, by core radius we refer to that of the density distribution in the plane of the Galactic disk. This is illustrated in Figure 4.3 for the equatorial density profiles and compared with those in the ‘uncoupled’ situation, in which the DM phase space distribution is determined by its own gravity alone.

Another direct effect of the VM on the DM is the relative enhancement of the DM density on the plane of the Galactic disk ($z = 0$) to that off the disk. Figure 4.4 shows that this effect, attributed to the influence of the axisymmetric disk potential, can be as large as $\sim$ 30-40 %. The spherical symmetry of DM halo density is thus broken by the axisymmetric Galactic disk. Note, however, that while the resulting density distribution of the halo becomes anisotropic, one can still assume, as done in this chapter, that the velocity distribution of the DM particles remains isotropic every where, although anisotropic (velocity) models are also possible [43] as discussed in detail in Chapter 7.

## 4.5 Maximum Speed and Speed Distribution of the particles

The self-consistently calculated maximum speeds of DM particles on the Galactic equatorial plane are shown in Figure 4.5 (top panel) for the same three sets of King model halo parameters as in Figure 4.1. The corresponding normalized speed

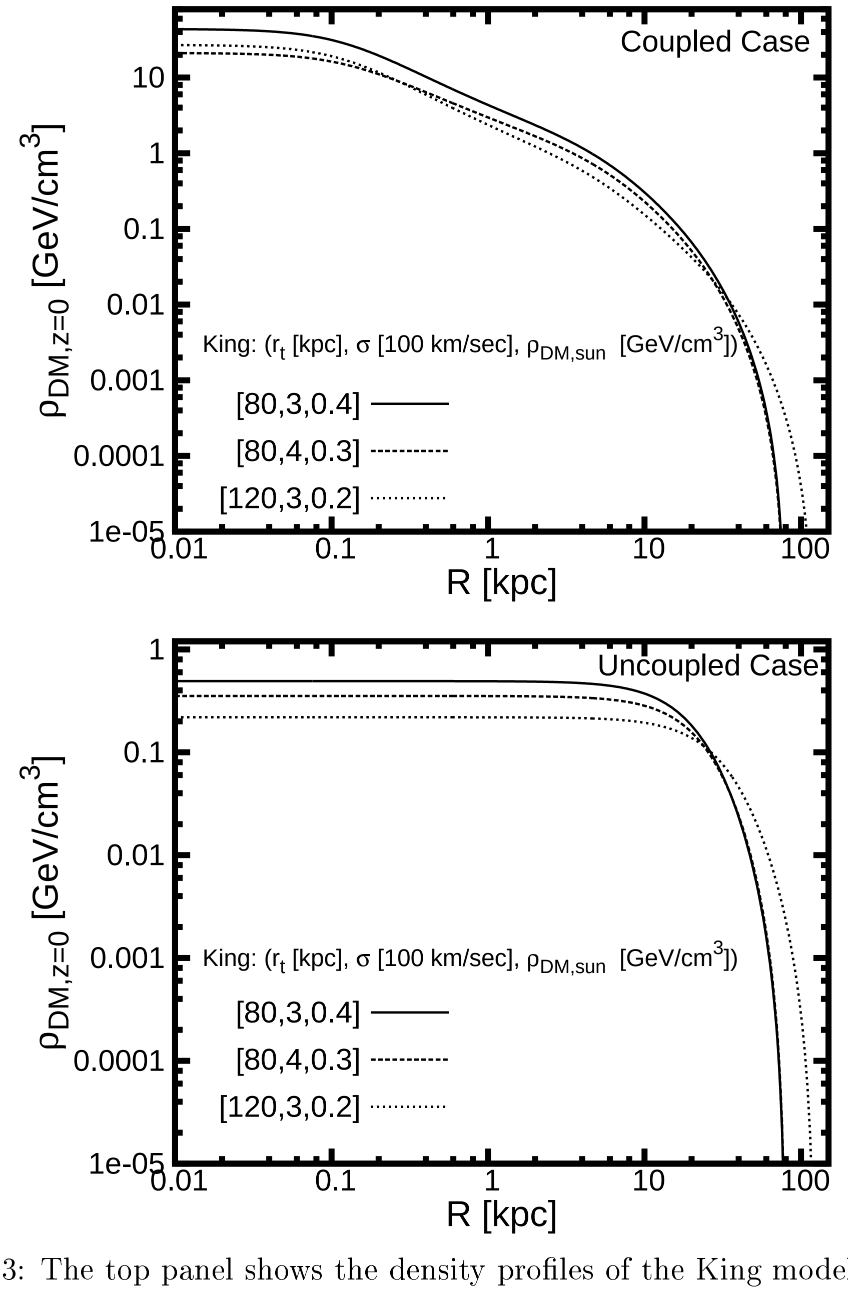


Figure 4.3: The top panel shows the density profiles of the King model halo of the Galaxy for the same three sets of halo parameters as in Figure 4.1 that yield best fit to the rotation curve data of the Galaxy [83, 6] for the 'coupled' case. The density profiles refer to those on the equatorial plane ($z = 0$) of the Galaxy. In the bottom panel, the density profiles are plotted for the same set of dark matter parameters for an isolated halo or 'uncoupled' case for the sake of comparison.

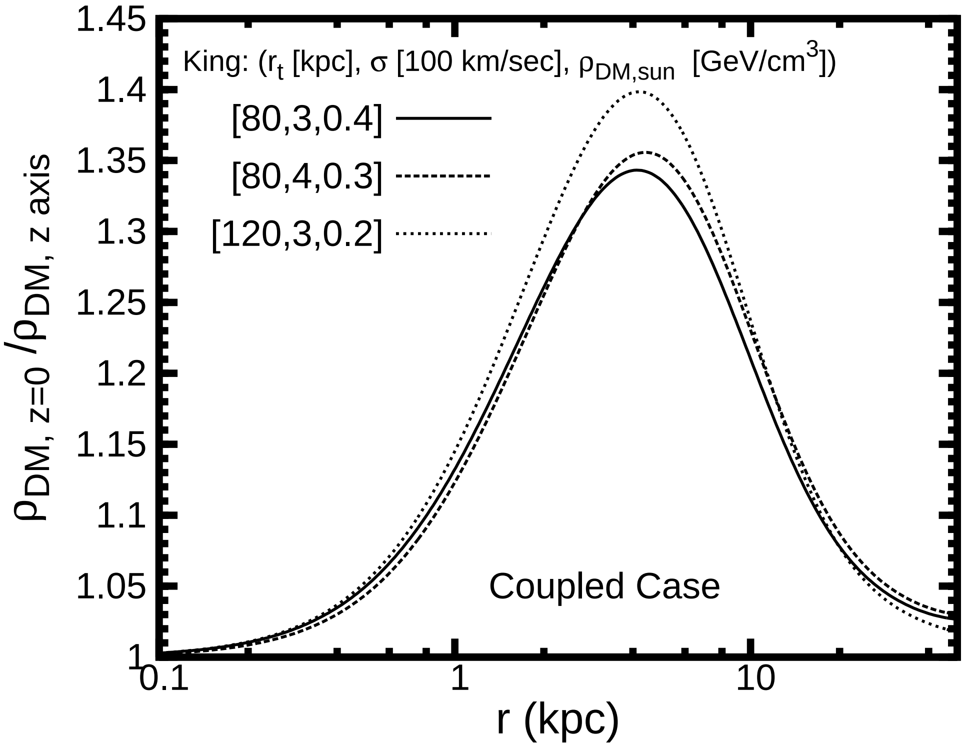


Figure 4.4: The ratio of the DM density on the $z = 0$ plane to that on the $z$ axis as a function of galactocentric distance, for the same three sets of King model parameters as in Figure 4.1 that yield best fit to the rotation curve data of the Galaxy [83, 6] for the 'coupled' case.

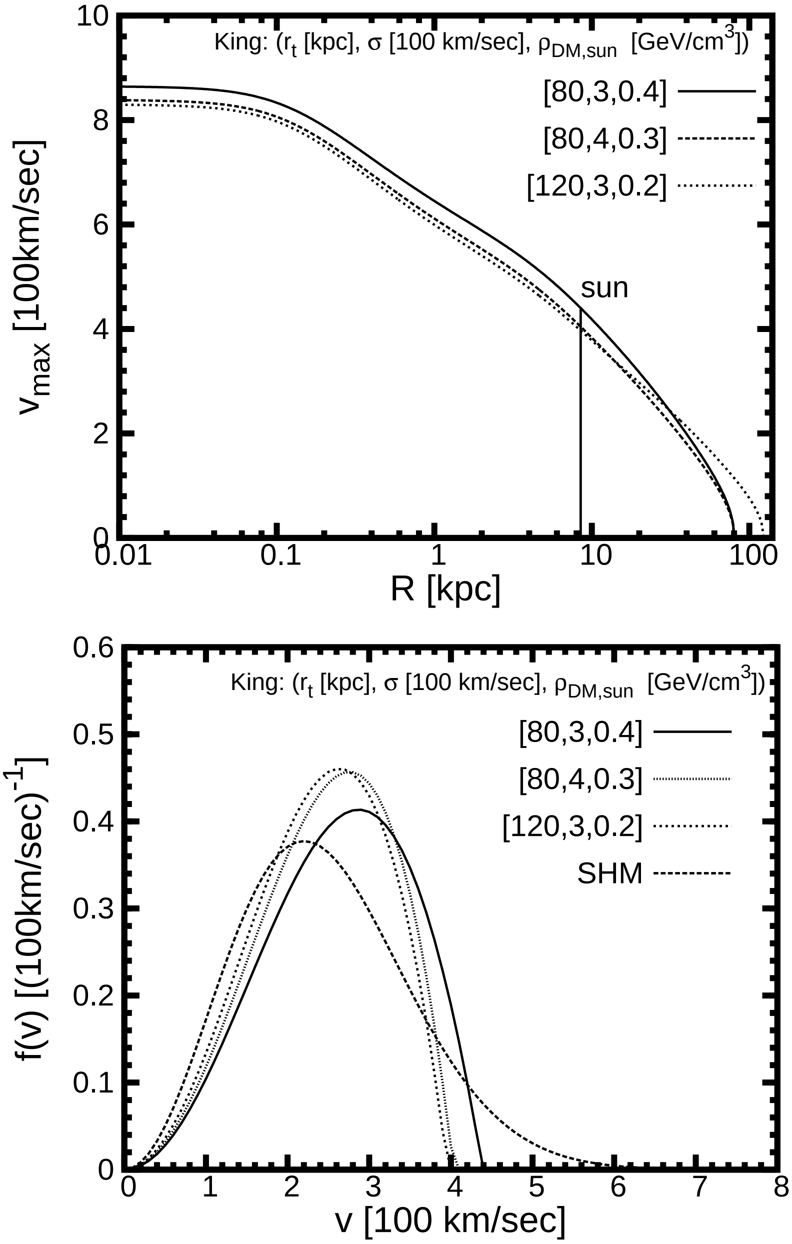


Figure 4.5: Maximum speed of a test particle $v_{\rm max}(\mathbf{x}) = \sqrt{2\Psi(\mathbf{x})}$ as a function of galactocentric distance $R$ (top panel) and the normalized dark matter speed ($v = |\mathbf{v}|$) distribution function (see Equation 4.5) (bottom panel), at Sun's location ($R = R_0$, $z = 0$), for the same three sets of King model parameters as in Figure 4.1 that yield best fit to the rotation curve data of the Galaxy [83, 6] for the 'coupled' case. The Maxwellian speed distribution in the standard halo model (SHM) with velocity dispersion of $\langle v^2\rangle^{1/2} \simeq 270\,\mathrm{km\,s^{-1}}$, is shown along with the best-fit King model speed distributions in the bottom panel, for comparison.

distribution functions of the DM particles (in the Galactic rest frame), $f(v) \equiv \frac{4\pi v^2}{\rho(\mathbf{x})} f(\mathbf{x}, \mathbf{v})$ (with $\int_0^{v_{\rm max}(\mathbf{x})} f(v) dv = 1$), at Sun's location ($R = R_0,\ z = 0,$ for $|\mathbf{x}| = R_0$), are also shown (bottom panel). For comparison, the Maxwellian speed distribution used in the SHM at Sun's location ( $R_0 =$ 8.5 kpc), is also shown. Evidently, the speed distribution for the DM particles constituting a King model type PSDF is significantly non-Maxwellian, especially at the high speed end of the distribution.

For the three King model parameter sets considered in the top panel of Figure 4.5 the maximum speeds of the DM particles at the location of Sun are, from bottom to top, 396, 403 and 439 $\,{\rm km\,s^{-1}}$, respectively. The best fit model with $\rho_{{\rm DM},\odot} = 0.2\,{\rm GeV\,cm^{-3}}$, truncation radius: $r_t = 120\,{\rm kpc}$ and velocity parameter: $\sigma \simeq 300\,{\rm km\,s^{-1}}$ with corresponding local VDF shown in the bottom panel of Figure 4.5, will be used in the calculation of the expected WIMP detection rates and analysis of the results of DD experiments in the following Section. It should be emphasized that the above values refer to the maximum speeds that any *test particle* can have at the location of the Sun to remain bound within the halo.

## 4.6 Implications of the Truncated Isothermal Model of the Galaxy's Dark Matter Halo for the Analysis of Direct Detection Experiments

### 4.6.1 Direct Detection Experiments Considered

In this subsection, we study the issue of compatibility of the claimed modulation signal reported by the DAMA experiment [68] with the null results from three other experiments, namely, CDMS-II (Ge and Si) [88, 81], CRESST-I [89] and XENON-10 [90, 91] [1] within the context of the King model as a description of the Galaxy's DM halo described above. In doing this, we choose the best fit parameter set for the model determined by fitting to the RC data of the Galaxy as discussed in Section 4.3. Here, we restrict our attention to only elastic scattering of WIMPs off nuclei due to SI as well as SD WIMP-nucleus interactions, denoting corresponding interaction cross sections with the nucleons by $\sigma_{\chi-nucleon}$ and $\sigma_{\chi-n(p)}$ for SI and SD case, respectively, for this analysis. .

The details of all the experiments considered here are same as described in Section 3.3 where we have only considered SI interactions of the WIMPs with the target nuclei while analyzing the results. Here, we also consider SD interactions of the WIMPs. Recall that DAMA [69, 68] employs radio-pure NaI crystals as target detector material. Since natural Na and I come almost entirely in the form of $^{23}$Na and $^{127}$I (with other isotopes present only in trace amounts), the total target mass for DAMA is effective for SD interactions of the WIMPs. For CDMS-II (Ge) [81], considering SD interaction of the WIMPs, merely 7.73% of the exposure consisting of $^{73}$Ge isotope (since its natural abundance $\approx$ 7.73%) is sensitive to the WIMPs, whereas for CDMS-II (Si) [88], a fraction of 4.67 % of the exposure consisting of $^{29}$Si isotope (where, natural abundance $\approx$ 4.67%) is effective. For CRESST-I [89], 100% of the $^{27}$Al contained in the $Al_2O_3$ target contributes to the SD interaction whereas $^{16}$O has null contribution since J=0 for Oxygen nucleus. In the case of XENON-10 [90, 91], for the SD case, only the isotopes $^{129}$Xe with a natural abundance of $\approx$ 26.4% and $^{131}$Xe with a natural abundance of $\approx$ 21.2% are

[1] There have been updated results published by the collaborations. However, the analyses presented here with the old versions of the experimental results, should, we believe, be good enough for the purpose of illustrating the effects of the variations of the relevant astrophysical parameters on the results of the various DD experiments.

effective.

For analysis of data for CDMS-II (employing Ge target) [81], we use a minimum bin width of 0.4 keV for precise results in contrast to 5 keV used earlier in the context of an IS model in Section 3.3. For XENON-10 [90, 91], we use an energy resolution function of the form [46] $\sigma(E_R) = (0.579\,\mathrm{keV})\sqrt{E_R/\,\mathrm{keV}} + 0.021 E_R$, an efficiency function of the form [46] $\epsilon(E_R) = 0.46\big(1 - \frac{E_R}{135\mathrm{keV}}\big)$ and an exposure of 316.4 kg-days (58.6 live days $\times$ 5.4 kg) [91].

Table 4.1 summarizes the relevant features of the "null" experiments we consider in this analysis. The values of the relevant quantities like total angular momentum, J, and expectation value of the spin content of the protons and neutrons in the nucleus i.e., $< S_p >$ and $< S_n >$ required for calculation of SD cross-sections for the target nuclei considered here are already given in Table 2.1.

| Experiment | Target | Effective exposure (kg-days) | Threshold ( keV) |
|---|---|---|---|
| CDMS-II [81] | $^{73}$Ge | 304.5 (SI), 23.5 (SD) | 10 |
| CDMS-II [88] | $^{29}$Si | 12.1 (SI), 0.57 (SD) | 7 |
| CRESST-I [89] | $^{27}\mathrm{Al}_2^{16}\mathrm{O}_3$ | 1.51 (SI), 0.80 (SD) | 0.6 |
| XENON-10 [90, 91] | $^{129}$Xe & $^{131}$Xe | 316.4 (SI), 150.6 (SD) | 6.1 |

Table 4.1: Relevant features of the experiments (exposures indicated for spin-independent (SI) and spin-dependent (SD) WIMP-nucleus interactions) with null results. Specific isotopes relevant for calculation of SD cross-sections are also indicated here as superscripts to the target nuclei.

We now analyze the results of the above mentioned DD experiments in the context of King model of the DM halo of the Galaxy with parameters determined by fit to RC data following the analysis techniques already described in Section 3.3.

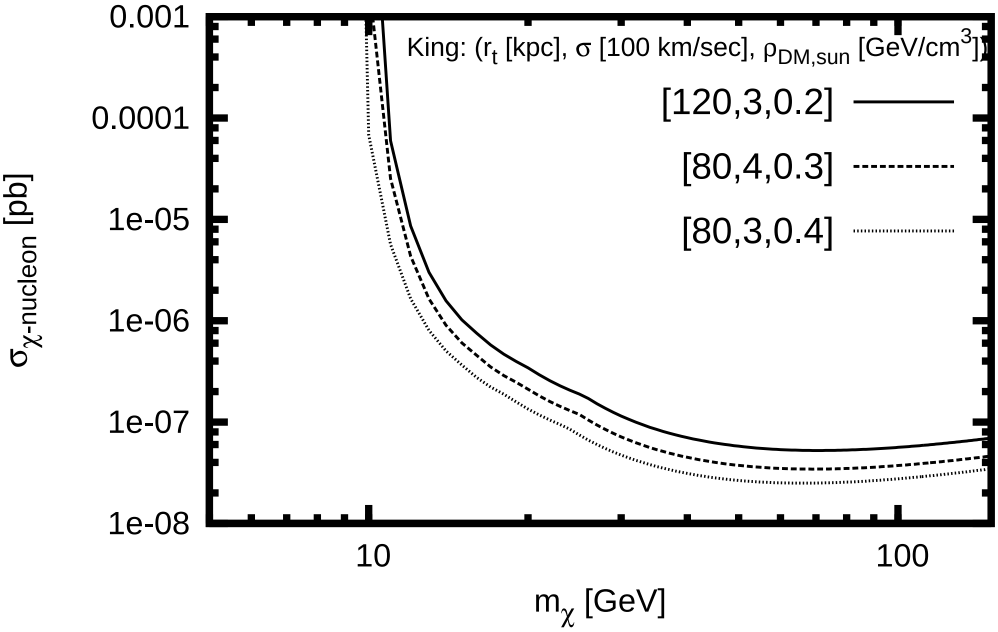


Figure 4.6: The 90% confidence level upper limits on the WIMP-nucleon spin-independent cross section as a function of WIMP mass as implied by the CDMS-II (Ge) results [81], for the self-consistent King model type Galactic dark matter halo described by the same three sets of halo model parameters as in Figure 4.1 that yield best fit to the rotation curve data of the Galaxy [83, 6] for the 'coupled' case.

### 4.6.2 Implications for the WIMP parameters

Figures 4.6 - 4.9 show our main results [101] in terms of the constraints on the relevant WIMP-nucleon cross sections as a function of the WIMP mass, as implied by the results of the DD experiments considered in the last subsection, in the context of a self-consistent King model type Galactic DM halo described by the model parameters that yield best fit to the rotation curve data of the Galaxy [83, 6] for the 'coupled' case. In all these Figures, the regions above the curves are excluded at the 90% C.L. by the results of the respective null experiments.

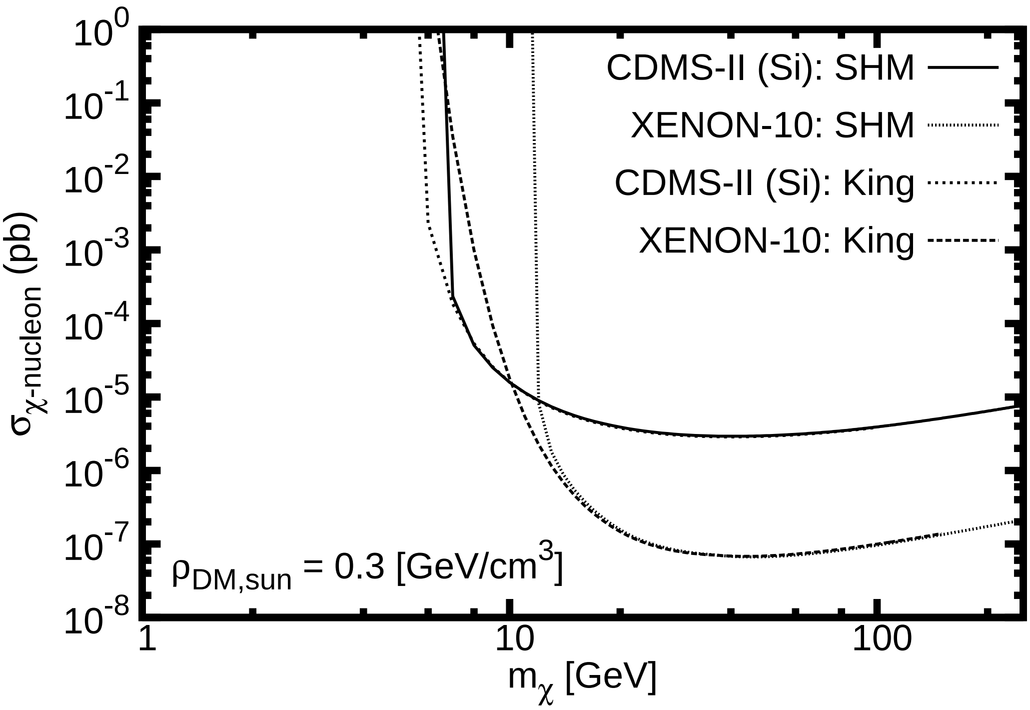


Figure 4.7: The 90% confidence level upper limits on the WIMP-nucleon spin-independent cross section as a function of WIMP mass as implied by the CDMS-II (Si) experiment [88] and XENON-10 experiment [90] using standard halo model or SHM (with dark matter velocity dispersion $\langle v^2\rangle^{1/2} = 270\,\mathrm{km\,s^{-1}}$ and a local dark matter density $\rho_{\mathrm{DM},\odot} = 0.3\,\mathrm{GeV\,cm^{-3}}$) and the King model for same local DM density as $\rho_{\mathrm{DM},\odot} = 0.3\,\mathrm{GeV\,cm^{-3}}$ and the values of the other two parameters ($r_t$ and $\sigma$) that yield best fit to the rotation curve data of the Galaxy [83, 6] for the 'coupled' case.

Figure 4.6 shows the 90% C.L. upper limit on WIMP-nucleon SI cross section as a function of WIMP mass as implied by the CDMS-II (Ge) results [81] for the King model with $\rho_{\rm DM,\odot} = 0.2,\ 0.3,\ 0.4\,{\rm GeV\,cm^{-3}}$ (with other halo parameters fixed by fitting to the RC data). For $\rho_{\rm DM,\odot} = 0.3\,{\rm GeV\,cm^{-3}}$ the lowest upper limit on the WIMP-nucleon SI cross section is $3.4 \times 10^{-8}$ pb at $m_\chi = 69\,{\rm GeV}$. For our self-consistent King model description of the DM halo used here, giving $\rho_{\rm DM,\odot} = 0.2\,{\rm GeV\,cm^{-3}}$ as the local DM density as the global best fit to the RC data, the above upper limit on the SI cross section changes to $\sim 5.3 \times 10^{-8}$ pb at $m_\chi = 71\,{\rm GeV}$. In the high WIMP mass regions, we note that, the upper limits on the cross section approximately scales inversely with the local DM density, $\rho_{\rm DM,\odot}$, values. However, for small WIMP mass region, with $m_\chi \ll M$, the mass of the target nucleus, the velocity integral part contained in the '$\xi$' factor [see Equation (2.5)] contributes differently for different values of VDF as well as $m_\chi$, and consequently, the upper limit on the cross-section does not have the simple inverse scaling with the value of $\rho_{\rm DM,\odot}$.

In the Figure 4.7, we compare SI results from CDMS-II (Si) experiment [88] and XENON-10 experiment [90] analyzed using the SHM with those analyzed in the context of King model for the same value of the local DM density as $\rho_{\rm DM,\odot} = 0.3\,{\rm GeV\,cm^{-3}}$. Note that, for $m_\chi \ll M$ (For Si, mass number is 28 and for Xenon mass number is 131), the SHM and King model results on the upper limits on the cross-sections differ from each other, while agreeing well at high $m_\chi$ region. The reason for this behavior is not hard to understand. In Equation (2.2), the WIMP-nucleus reduced mass $\mu \approx m_\chi$ for $m_\chi \ll M$. Therefore, the lower limit of the velocity integral, $\xi$, reduces to $u_{\rm min}(E_R) = \left(\frac{ME_R}{2m_\chi^2}\right)^{1/2}$, which is larger for smaller values of $m_\chi$. This implies that, as $m_\chi$ gets smaller, correspondingly smaller portion of the high velocity end of the WIMP VDF contributes to the $\xi$ factor of the Equation (2.5). Since, the high velocity end of the VDFs for SHM and King model differ significantly from each other, this results in a significant difference in the exclusion plots for the two models in the $m_\chi \ll M$ region. However, in the large $m_\chi$ region, where $u_{\min}$ is independent of $m_\chi$, the $\xi$ factor receives contribution from the entire VDF, not just from the high velocity ends of the VDF, thus averaging out the differences due to the different behaviors of the two VDFs at their high velocity ends yielding approximately similar values of the $\xi$ factor for the two VDFs. This, in turn, makes the upper limits on the cross-sections fairly insensitive to the exact form of the VDF, and are thus essentially same for the same chosen value of $\rho_{\rm DM,\odot}$. These results underscore the important role played by the form of VDF, especially at its high velocity end for exploring the relatively low mass WIMPs in DD experiments and the consequent need to adopt physically realistic models of the phase space structure of the DM halo of the Galaxy.

Figures 4.8 and 4.9 show the "DAMA compatible" regions (defined in Section 3.3.2), for the cases of WIMP-nucleon SI and SD interactions under elastic scattering. The analysis is based on the King model for local DM density, $\rho_{\rm DM,\odot} = 0.2\,{\rm GeV\,cm^{-3}}$ and the values of the other two parameters ($r_t$ and $\sigma$) that yield best fit to the rotation curve data of the Galaxy [83, 6] for the 'coupled' case.

For the SI case, we find that there is a range of small WIMP masses, $2.6 \lesssim m_\chi \lesssim 10.8\,{\rm GeV}$, within which DAMA's claimed modulation signal is consistent with the null results of other experiments. The allowed WIMP-nucleon SI cross section varies from $\sim 1.2 \times 10^{-5}$ pb at the lower end of the WIMP mass range to $\sim 1.0 \times 10^{-2}$ pb at the upper mass end. In the previous chapter the corresponding regions for SI interaction were obtained as $2.8 \lesssim m_\chi \lesssim 11.8\,{\rm GeV}$

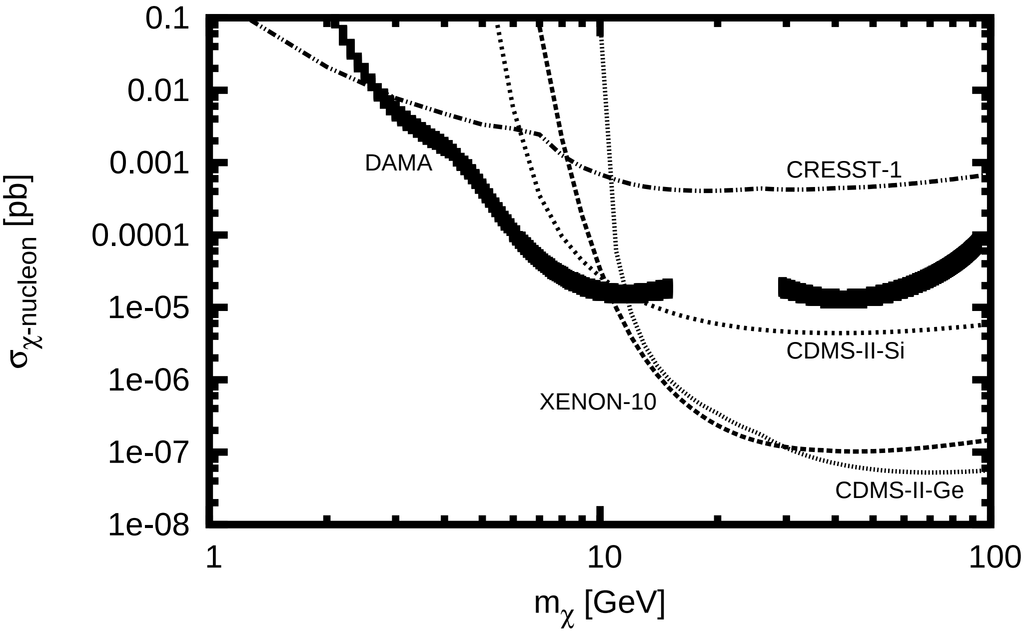


Figure 4.8: The 90% confidence level allowed region in the WIMP mass vs. WIMP-nucleon spin-independent cross section plane implied by the DAMA modulation signal, for our global best-fit King model parameter set obtained from fit to the rotation curve data of the Galaxy [83, 6] (for the 'coupled' case), namely, $r_t = 120\,\mathrm{kpc}$, $\sigma = 300\,\mathrm{km\,s^{-1}}$ and $\rho_{\mathrm{DM},\odot} = 0.2\,\mathrm{GeV\,cm^{-3}}$. Also shown are 90% confidence level upper limits on cross section as a function of WIMP mass as implied by the null results of other experiments for the same dark matter halo parameter set.

and $7.3 \times 10^{-6} \lesssim \sigma_{\chi-nucleon} \lesssim 4.8 \times 10^{-3}$ pb in the context of SHM (see top-left panel of Figure 3.4). It is seen that the mass range becomes a little bit constrained and the cross section limits are about one order of magnitude less stringent in the King model case compared to those in the SHM. However, it should be noted that for the King model analysis the local dark matter density is taken to be $0.2\,\mathrm{GeV\,cm^{-3}}$ whereas for the SHM, considered in the previous chapter, it is 1.5 times higher at $0.3\,\mathrm{GeV\,cm^{-3}}$. However, the shifts in the allowed parameter space do not scale with the value of $\rho_{\mathrm{DM},\odot}$ in the low mass regions, where the local velocity integral is important.

For the SD case, the DAMA-compatible mass range for WIMP-neutron interaction (i.e., $a_p = 0$) is $2.5 \lesssim m_\chi \lesssim 7.4\,\mathrm{GeV}$, with the corresponding WIMP-neutron interaction cross section range of $9.5 \times 10^3$ - 42.0 pb. For the case of WIMP-proton interaction (with $a_n = 0$), the corresponding WIMP mass and cross section ranges are $2.3 \lesssim m_\chi \lesssim 16\,\mathrm{GeV}$ and 79.0 - 0.45 pb, respectively. The SD allowed cross sections for WIMP-proton and WIMP-neutron interactions are seen to be widely different since WIMP interacts with the protons and neutrons differently because of the different structure functions involved (see Section 2.1).

## 4.7 Summary

In this Chapter, we have presented a self-consistent model of the finite-size DM halo of the Galaxy with its PSDF described by a "truncated isothermal" model (or "King" model) [43]. The parameters of the model are determined by fitting with a circular velocity curve of the Galaxy that extends up to a galactocentric distance of $\sim 60\,\mathrm{kpc}$ [83, 6] with best fit parameter values for local dark matter density $\rho_{\mathrm{DM},\odot} = 0.2\,\mathrm{GeV\,cm^{-3}}$, truncation radius $r_t \simeq 120\,\mathrm{kpc}$ and velocity parameter $\sigma \simeq 300\,\mathrm{km\,s^{-1}}$ with local circular velocity of $\sim 232\ \mathrm{km\,s^{-1}}$ and DM velocity dispersion at Solar location, $\langle v^2 \rangle_\odot^{1/2}$, as $252\ \mathrm{km\,s^{-1}}$. In doing this the modifications of the phase-space structure of the halo due to the gravitational influence of the observed VM is taken into account in a self-consistent manner. The speed distribution function of the WIMPs constituting the halo is found to be of non-Maxwellian form, with a finite cut-off at a maximum speed lying within a range of 400 - 450 $\mathrm{km\,s^{-1}}$ for $0.2\,\mathrm{GeV\,cm^{-3}} \leq \rho_{\mathrm{DM},\odot} \leq 0.4\,\mathrm{GeV\,cm^{-3}}$ that is

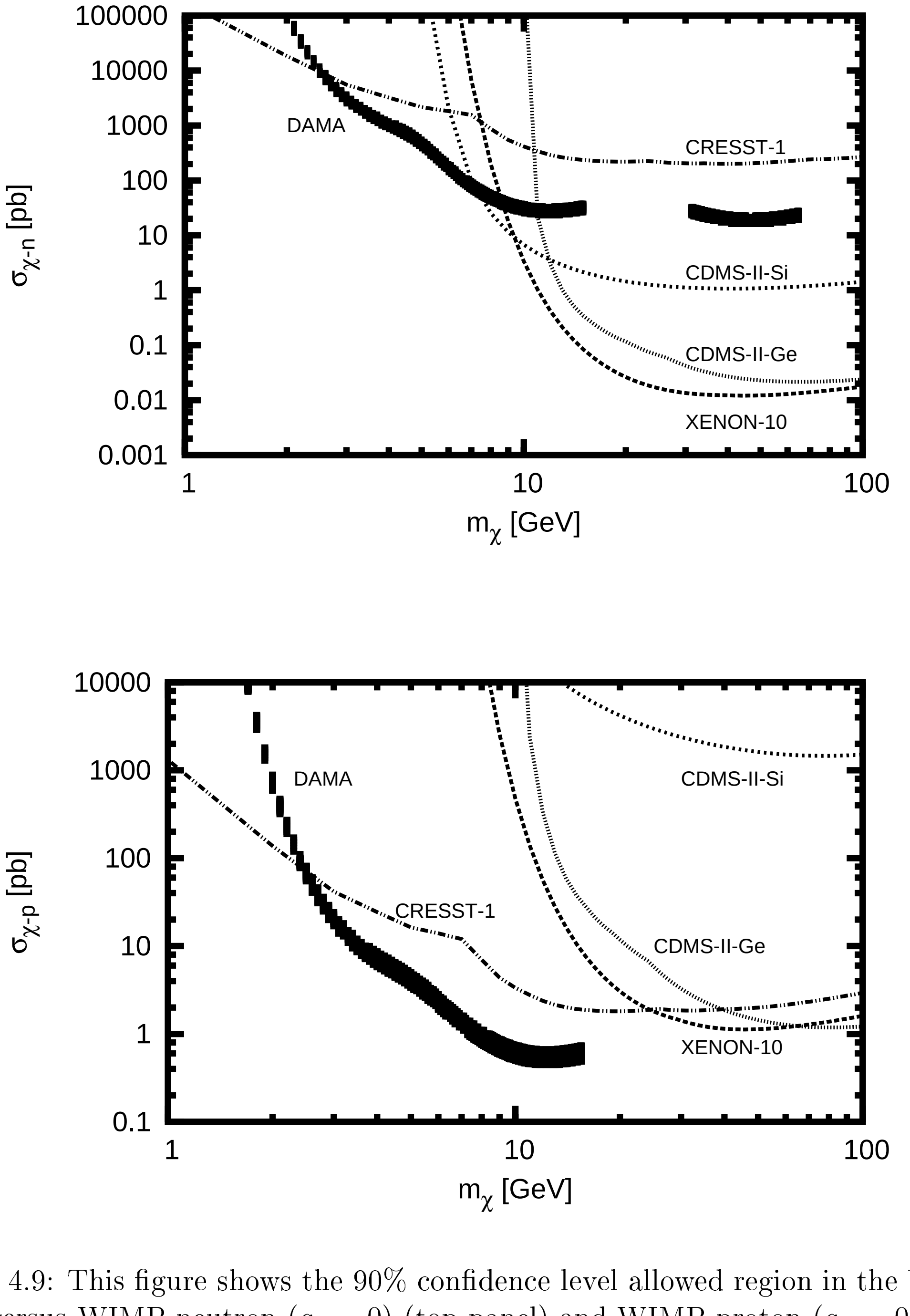


Figure 4.9: This figure shows the 90% confidence level allowed region in the WIMP mass versus WIMP-neutron ($a_p = 0$) (top panel) and WIMP-proton ($a_n = 0$) (bottom panel) spin-dependent cross section plane implied by the DAMA modulation signal, for the self-consistent King model type Galactic DM halo with parameters $r_t = 120\,\mathrm{kpc}$, $\sigma = 300\,\mathrm{km\,s^{-1}}$ and $\rho_{\mathrm{DM},\odot} = 0.2\,\mathrm{GeV\,cm^{-3}}$ that gives global best fit to the rotation curve data of the Galaxy [83, 6] (for the 'coupled' case). Also shown are 90% confidence level upper limits on the cross sections as a function of WIMP mass as implied by the null results of other experiments, again for the same set of halo parameters.

self-consistently determined by the model itself.

The VM coupling also leads to a DM density enhancement of about 30-40 % on the disk plane and leads to a higher central density and lower core radius of the DM density profile compared to the isolated DM halo without the effect of VM on DM (the 'uncoupled' case). The declining trend of the RC imposes strong constraints on the (truncation) radius, central density and hence on the total mass of the Galaxy. Specifically, for values of local DM density in the range $\rho_{\rm DM,\odot} = 0.2\text{-}0.4\,{\rm GeV\,cm^{-3}}$, reasonable fits to the RC data require the truncation radius of the halo to be in the corresponding range $r_t \approx$ 120-80 kpc, in all cases restricting the total mass of the Galaxy (including its DM halo) to relatively low values of $M_{\rm Galaxy} \lesssim 3 \times 10^{11}\, M_{\odot}$.

Note, however, that the rotation curve estimated in Ref. [6], which is used in determining the parameters of our halo model, was derived assuming a value of the local circular velocity to $V_0 \approx 220\ {\rm km\,s^{-1}}$. On the other hand, as suggested in [84], the value of the local circular speed may be larger, namely, $V_{c,\odot} \approx 244\,{\rm km\,s^{-1}}$. This would require appropriate scaling up of the RC data, as explored in a later chapter.

Interestingly, with the King model type DM halo, the upper limits on the relevant WIMP-nucleon interaction cross section implied by the null results of the DD experiments are primarily determined by the chosen value of the local DM density $\rho_{\rm DM,\odot}$, scaling roughly inversely with the value and are relatively less sensitive to integral of the local velocity profile, encoded in the '$\xi$' factor in Equation (2.5), except for small WIMP masses, $m_\chi \ll M$, the mass of target nuclei, where the form of the VDF (especially its high velocity ends) plays an important role. This is shown by comparing the CDMS-II (Ge) experiment [81] exclusion plots for three best fit parameter sets of the King model for local DM density $\rho_{\rm DM,\odot} = 0.2,\ 0.3,\ 0.4\,{\rm GeV\,cm^{-3}}$. For parameter regions where $m_\chi \ll M$ and $u_{\rm min}$ takes high enough values and therefore the cross sections are affected by the velocity integral, particularly by the tail of the VDFs. This is also evident from comparing the CDMS-II (Si) experiment [88] and XENON-10 experiment [90] results from SHM and the King model characterized by same local DM density as $\rho_{\rm DM,\odot} = 0.3\,{\rm GeV\,cm^{-3}}$, but different local VDFs. The plots agree closely except for $m_\chi \ll M$ otherwise cross-section varies roughly as inversely with the value of $\rho_{\rm DM,\odot}$.

For our global best-fit self-consistent King model with parameter values as, $\rho_{\rm DM,\odot} = 0.2\,{\rm GeV\,cm^{-3}}$, $r_t = 120\,{\rm kpc}$ and $\sigma \simeq 300\,{\rm km\,s^{-1}}$, the null result of the CDMS-II (Ge) experiment [81], for example, gives a 90% C.L. upper limit on the WIMP-nucleon SI interaction cross section $\sigma_{\chi-nucleon} \sim 5.3 \times 10^{-8}$ pb at a WIMP mass of 71 GeV though the strongest upper limit on cross section is obtained for $\rho_{\rm DM,\odot} = 0.4\,{\rm GeV\,cm^{-3}}$.

It is found that for the global best-fit halo model, that occurs for $\rho_{\rm DM,\odot} = 0.2\,{\rm GeV\,cm^{-3}}$, there exists a region of the WIMP mass ($m_\chi$) vs. WIMP-nucleon SI cross section parameter space bounded by $2.6 \lesssim m_\chi \lesssim 10.8\,{\rm GeV}$ and $1.0 \times 10^{-2} \gtrsim \sigma^{\rm SI}_{\chi-nucleon} \gtrsim 1.2 \times 10^{-5}$ pb, within which the DAMA's claimed modulation signal is compatible with the null results of other experiments. Similar "DAMA-compatible" regions of small WIMP masses are also obtained for SD interactions. For WIMP-neutron interaction (i.e., $a_p = 0$), we get $2.5 \lesssim m_\chi \lesssim 7.4\,{\rm GeV}$ with the corresponding WIMP-neutron interaction cross section range of $9.5 \times 10^3$ - 42.0 pb. For the case of WIMP-proton interaction (with $a_n = 0$), the corresponding WIMP mass and cross section ranges are $2.3 \lesssim m_\chi \lesssim 16\,{\rm GeV}$ and 79.0 - 0.45 pb, respectively.

For comparison, the above upper limits on the WIMP-nucleon SI cross-sections are about an order of magnitude less stringent than those derived in the previous chapter in the context of SHM. However, it should be noted that for the King model analysis the local dark matter density is taken to be $0.2\,\mathrm{GeV\,cm^{-3}}$ whereas for the SHM, considered in the previous chapter, it is 1.5 times higher at $0.3\,\mathrm{GeV\,cm^{-3}}$ and the shifts in the allowed parameter space bounds do not scale simply with the value of $\rho_{\mathrm{DM},\odot}$ in the low mass regions where the effect of local velocity integral is significant.

# Chapter 5

# Rotation curve of Milky Way from Disk Tracers

## 5.1 Introduction

As clear from the discussions in the previous chapters, the rotation curve (RC) or circular velocity of the Galaxy, $V_c(r) = \sqrt{GM(r)/r}$, of a test particle as a function of Galactic radius, $r$, from the center of a mass distribution gives a direct observational probe of the total gravitational potential and hence total mass, $M(r)$, contained within that radius. See for e.g., [102], [103] for reviews. It is indeed the main observational anchor in our approach to the problem of deriving information on the phase space distribution of the particles hypothesized to constitute the dark matter (DM) halo of our Galaxy. In particular, we have discussed how the RC data can be used to determine both the density profile and the velocity distribution of the DM particles in the Galaxy, which are essential for analyzing the results of both direct as well as indirect DM search experiments [15] (See also [104, 105]). For this purpose, it is crucial to construct the RC to as large a galactocentric distance as possible without referring to any specific model of the visible matter (VM) distribution or DM halo of the Galaxy.

The circular velocity of a test particle in the Galaxy is, of course, not a directly measured quantity. The RC of the Galaxy has to be derived from the kinematical as well as positional data for an appropriate set of tracer objects moving in the gravitational field of the Galaxy. Except in few cases, the full 3-D velocity information of the tracers is not available, and the RC has to be reconstructed from only the measured line-of-sight (*los*) velocity, $v_{\rm h}$, of the tracers and their position coordinates in the Galaxy, by applying corrections for the peculiar motion of the Sun with respect to the local standard of rest (LSR). The later is defined by Galactic Constants (GCs), $\left[\frac{R_0}{\rm kpc}, \frac{V_0}{\rm km\,s^{-1}}\right]$, where $R_0$ and $V_0$ are the distance from and circular rotation speed of the LSR frame around the Galactic center, respectively. Some recent compilations of RC data for the disk region of the Galaxy can be found, e.g., in [105] and [106].

In this chapter, we particularly focus on deriving the RC of the Galaxy spanning a range of galactocentric distances starting from its inner regions ($\sim 0.2\,$kpc) out to $\sim 20\,$kpc using kinematical data on a variety of disk tracer objects, in a manner independent of any models for the VM and DM components of the Galaxy. We use observations on a wide range of tracers such as HI regions, CO emission associated with HII regions, compact objects like Carbon stars (C stars), Cepheids, planetary nebulae (PNe), and so on, to derive the RC of the Galaxy in the disk region.

The investigation of the dependence of the RC data on the choice of GCs is crucial at this point since there have been recent revisions proposed for both the $R_0$ and $V_0$ values [107, 84]. It is to note that RC data do not simply scale with the values of $R_0$ and $V_0$. Here, we have therefore studied the behavior of RC data for various GCs sets by properly calculating the data for different GCs sets starting from first principles. The values of the adopted GCs set are seen to influence the resultant RC data which in turn determine the local DM density obtained by Galactic mass modeling, as will be discussed in Chapter 6. Recent comprehensive discussions of the RC and mass models for our Galaxy can be found, e.g., in [32, 7, 108].

In the following sections, first we show the formalism of constructing the disk RC given the position and heliocentric line of sight velocity of a tracer. Thereafter, we derive the RC considering a variety of disk tracers and combining the corresponding data sets by standard weighted average method to obtain the final disk RC for three different GCs sets. We summarize our results at the end.

## 5.2 Formalism of Construction of Disk Rotation Curve

Let us consider a tracer object with Galactic coordinates $(l,\ b)$ at a heliocentric distance $r_{\rm h}$ and observed heliocentric *los* velocity $v_{\rm h}$ (see Figure 5.1).

For deriving the RC in the disk region of the Galaxy, it is reasonable to assume that the disk tracer objects move in circular orbits around the Galactic center. The velocity of the tracer as would be measured by an observer stationary with respect

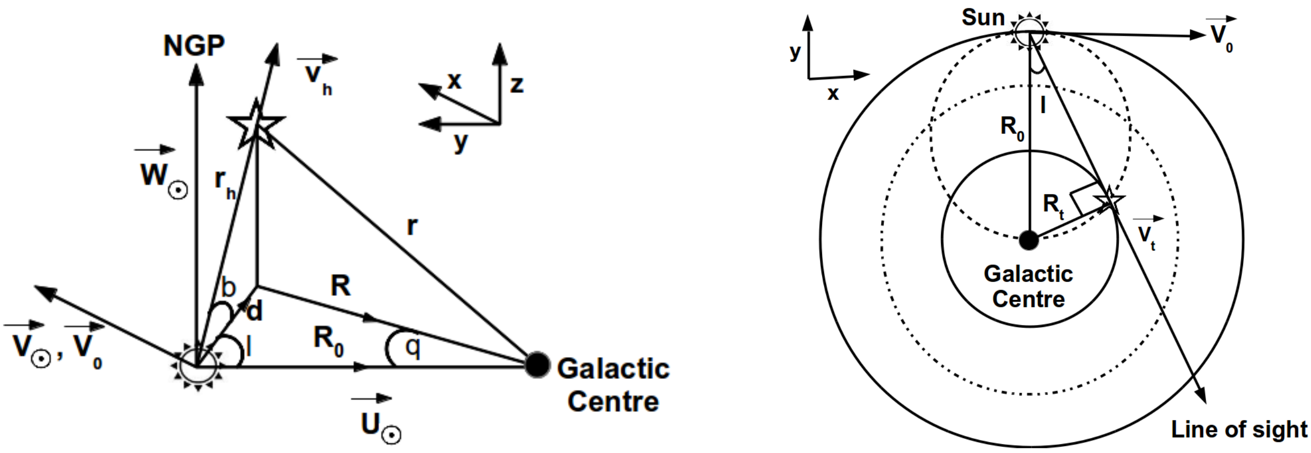


Figure 5.1: Left: Schematic diagram showing the coordinate system, velocity and distance notations used in this chapter. Right: Illustration of the tangent point method for deriving the circular speeds for distances $R < R_0$, where $R_0$ is the distance of the Sun on the disk from Galactic center.

to the LSR, $v_{\rm LSR}$, can be obtained from the measured $v_{\rm h}$ through the relation,

$$v_{\rm LSR} = v_{\rm h} + U_\odot \cos b \cos l + V_\odot \cos b \sin l + W_\odot \sin b, \tag{5.1}$$

where $(U_\odot, V_\odot, W_\odot)$ denote the peculiar motion of the sun with respect to LSR (see Figure 5.1). In the calculations below, we shall take revised values for the peculiar velocities, $(\frac{U_\odot}{\rm km\,s^{-1}}, \frac{V_\odot}{\rm km\,s^{-1}}, \frac{W_\odot}{\rm km\,s^{-1}}) = (11.1,\ 12.24,\ 7.25)$ [109].

For a tracer lying on the equatorial plane (i.e., $b = 0$) at galactocentric distance $R$, the $v_{\rm LSR}$ can be calculated by taking the projection of the difference of circular velocity vector at the point $\mathbf{R}$ given by $\mathbf{V_c}(\mathbf{R})$ and that at LSR (or Solar) location, $\mathbf{R_0}$ given by $\mathbf{V_0}$, along the vector joining Solar location and the point at $R$, given by $\mathbf{d} = \mathbf{R_0} - \mathbf{R}$. Therefore, $v_{\rm LSR}$ is given by,

$$v_{\rm LSR} = \frac{\mathbf{R_0} - \mathbf{R}}{|\,\mathbf{R_0} - \mathbf{R}|} \cdot (\mathbf{\Omega_R} \times \mathbf{R} - \mathbf{\Omega_{R_0}} \times \mathbf{R_0}), \tag{5.2}$$

where $\mathbf{V_c} = \mathbf{\Omega_R} \times \mathbf{R}$ and $\mathbf{V_0} = \mathbf{\Omega_{R_0}} \times \mathbf{R_0}$, and $\mathbf{\Omega_R}$ and $\mathbf{\Omega_{R_0}}$ are the angular velocities at $\mathbf{R}$ and $\mathbf{R_0}$, respectively.

Using vector identities, $\mathbf{a}.(\mathbf{a} \times \mathbf{b}) = 0$ and $\mathbf{a}.(\mathbf{b} \times \mathbf{c}) = \mathbf{b}.(\mathbf{c} \times \mathbf{a})$, we get,

$$v_{\rm LSR} = [\mathbf{\Omega_R} - \mathbf{\Omega_{R_0}}].\frac{\mathbf{R} \times \mathbf{R_0}}{|\,\mathbf{R_0} - \mathbf{R}|}. \tag{5.3}$$

We have, $\mathbf{R_0} \times \mathbf{R} = R_0 R \sin q\ \hat{\mathbf{n}}$ where $q$ is the angle between $\mathbf{R_0}$ and $\mathbf{R}$ and $\hat{\mathbf{n}}$ is the unit vector pointing away vertically upward from the disk. Therefore, we have,

$$v_{\rm LSR} = [\mathbf{\Omega_R} - \mathbf{\Omega_{R_0}}].\ \frac{(\,R_0 R \sin q\ \hat{\mathbf{n}})}{|\,\mathbf{R_0} - \mathbf{R}|}. \tag{5.4}$$

Now, by the law of sines $\frac{\sin q}{|\mathbf{R} - \mathbf{R_0}|} = \frac{\sin(l)}{R}$ and using $\mathbf{\Omega} = \Omega \hat{n}$, we have,

$$v_{\rm LSR} = [\Omega_R - \Omega_{R_0}]\, R_0 \sin l. \tag{5.5}$$

Therefore, the circular velocity at R is given by,

$$V_c(R) = \frac{R}{R_0}\ \left[\frac{v_{\rm LSR}}{\sin l} + V_0\right], \tag{5.6}$$

with $\Omega_R = \frac{V_c}{R}$ and $\Omega_{R_0} = \frac{V_0}{R_0}$.

For tracers lying off the equatorial plane (i.e., $b \neq 0$) at $\mathbf{r}$, Equation (5.6) generalizes to,

$$V_c(R) = \frac{R}{R_0} \left[\frac{v_{\rm LSR}}{\sin l \cos b} + V_0\right] , \tag{5.7}$$

where $R$ is the projection of the galactocentric distance $r$ onto the equatorial plane,

$$R = \sqrt{R_0^2 + r_{\rm h}^2 \cos^2 b - 2\, R_0\; r_{\rm h} \cos b \cos l}\,. \tag{5.8}$$

For a given set of GCs, the Cartesian coordinates of the tracer are given by,

$$\begin{aligned} x &= r_{\rm h}\;\cos b\;\sin l\,, \\ y &= R_0 - r_{\rm h}\;\cos b\;\cos l\,, \\ z &= r_{\rm h}\;\sin b\,, \end{aligned} \tag{5.9}$$

with the Galactic center at the origin and Sun lying on the Galactic mid-plane ($z = 0$) with coordinates $(x, y, z) = (0,\, R_0, 0)$ as illustrated in the left panel of Figure 5.1. Hence, for known $(l,\; b,\; r_{\rm h},\; v_{\rm h})$ for a given tracer candidate one can solve for $V_c$ from Equation (5.7) assuming a given GCs set.

*Tangent Point Method* (TPM) : For $R <\; R_0$, one can calculate $V_c$ by the simple tangent point method [110] as follows: Along a given *los*, the maximum *los* velocity will occur for the tracer closest to the Galactic center as the tangent to the circular orbit of the tracer at that point (see right panel of Figure 5.1). This maximum *los* velocity, called the terminal velocity ($v_t$), is easily seen to be related to $V_c$ through the relation (see right panel of Figure 5.1),

$$V_c(R_t) = |v_{t,\mathrm{LSR}}(R_t) + V_0 \sin l| \,, \quad (b = 0)\,, \tag{5.10}$$

where

$$R_t = |\, R_0 \ \sin l| \tag{5.11}$$

is the distance of the tangent point from the Galactic center, and $v_{t,\mathrm{LSR}}$ is the $v_t$ corrected for the Sun's peculiar motion as in Equation (5.1).

For non zero galactic latitude ($b$), Equation (5.10) generalizes to:

$$V_c(R_t) = \left| \frac{v_{t,\mathrm{LSR}}(R_t)}{\cos b} + V_0 \ \sin l \right| . \tag{5.12}$$

Hence, for a given GCs set, the circular velocity $V_c$ can be calculated directly from the measured terminal velocity ($v_t$) by using Equation (5.12), once the galactic coordinates of the tracer are known. In this case the Cartesian coordinates of the tracer are given by,

$$\begin{aligned} x &= R_0 \ \sin l \ \cos l \,, \\ y &= R_0 \ \sin^2 l \,, \\ z &= R_0 \ \cos l \ \tan b \,. \end{aligned} \tag{5.13}$$

## 5.3 Disk Rotation Curve for Different Galactic Constants

The details of the disk tracer samples used for this analysis along with references to the corresponding data sources for each tracer genre are given in the Table 5.1. The cuts on $l$ and $b$ are adopted from the published source papers. Towards the Galactic center ($l \to 0°$) or anti-center ($l \to 180°$), one should expect $v_{\rm LSR}$ to approach zero to prevent unphysical $V_c$ values there [see Equation (5.7)]. However, $v_{\rm LSR}$ observations in practice have finite values due to contamination from non circular motions dominant there. Therefore, additional restrictions have been applied on $l$ ranges so as to avoid observations too close to Galactic center (anti-center) regions. We further impose a cut to keep only the tracers whose $|z| \leq 2\,{\rm kpc}$ and $R \leq 25\,{\rm kpc}$ so as to ensure that the selected tracers 'belong' to the stellar disk of the Galaxy. The $x$–$y$ and $l$–$z$ scatter plots for the selected disk tracers listed in Table 5.1 are shown in Figures 5.2 and 5.3, respectively (after $l$, $b$ cuts).

It is clear from Equations (5.7) – (5.13) that the RC depends on the set of values of the GCs: $\left[\frac{R_0}{\rm kpc}, \frac{V_0}{\rm km\,s^{-1}}\right]$ adopted in the calculation. Values of $R_0$ in the range $\sim (7-9)\,{\rm kpc}$ and $V_0$ in the range $\sim (180-250)\,{\rm km\,s^{-1}}$ exist in literature [126]-[133]. Actually, the ratio $V_0/R_0 = (A-B)$, $A$ and $B$ being the Oort constants [110], is considerably better constrained. Maser observations and measurements of stellar orbits around SgrA* near the Galactic center report values of $(A-B)$ in the range from about 29 to 32 ${\rm km\,s^{-1}\,kpc^{-1}}$ [134, 129, 130]. RCs have been traditionally presented with the IAU recommended set of values

Table 5.1: Disk tracer types, their source references and ($l$, $b$) ranges of the data sets used for deriving the rotation curve data in the disk region. Superscript '$a$' denotes the tracers limited within the Solar circle ($R < R_0$) where tangent point method has been used to derive the rotation speeds. The identifier for each tracer data set used in the chapter is given within parentheses in the first column under the respective tracer type for subsequent references in this chapter.

| Tracer Type | Data Source | $(l, b)$ Ranges |
|---|---|---|
| HI regions[a] (HI-W76-B78) | [111, 112] | $1° < l < 90°$ |
| CO clouds[a] (CO-B78) | [112] | $9° < l < 82°$ |
| CO clouds[a] (CO-C85) | [113] | $13° < l < 86°$ |
| HI regions[a] (HI-F89) | [114] | $15° < l < 89°$ and $271° < l < 345°$ |
| HII regions (HII-F89) | [114] | $10° < l < 170°$ and $190° < l < 350°$ |
| HII regions & reflection nebulae (HII-RN-B93) | [115] | $10° < l < 170°$ and $190° < l < 350°$ |
| Cepheids (Cepheid-P94) | [116] | $10° < l < 170°$ and $190° < l < 350°$; $\|b\| < 10°$ |
| Planetary nebulae (PNe-M05-M84-D98) | [117]-[119] | $15° < l < 345°$; $\|b\| < 10°$ |
| Open star clusters (OSC-F08-D02) | [120, 121] | $10° < l < 170°$ and $190° < l < 350°$; $\|b\| < 9°$ |
| HII regions (HII-H09) | [122] | $10° < l < 170°$ and $190° < l < 350°$ |
| HII regions[a] (HII-U11) | [123] | $10° < l < 65°$ and $280° < l < 350°$ |
| C stars (C stars-D07-B12) | [124, 125] | $54° < l < 150°$; $3° < \|b\| < 9°$ |

$\left[\frac{R_0}{\mathrm{kpc}}, \frac{V_0}{\mathrm{km\,s^{-1}}}\right]_{\mathrm{IAU}} = [8.5, 220]$, for which, however, the ratio $V_0/R_0 = 25.9$ is outside the range of values of this ratio mentioned above. A recently suggested set of

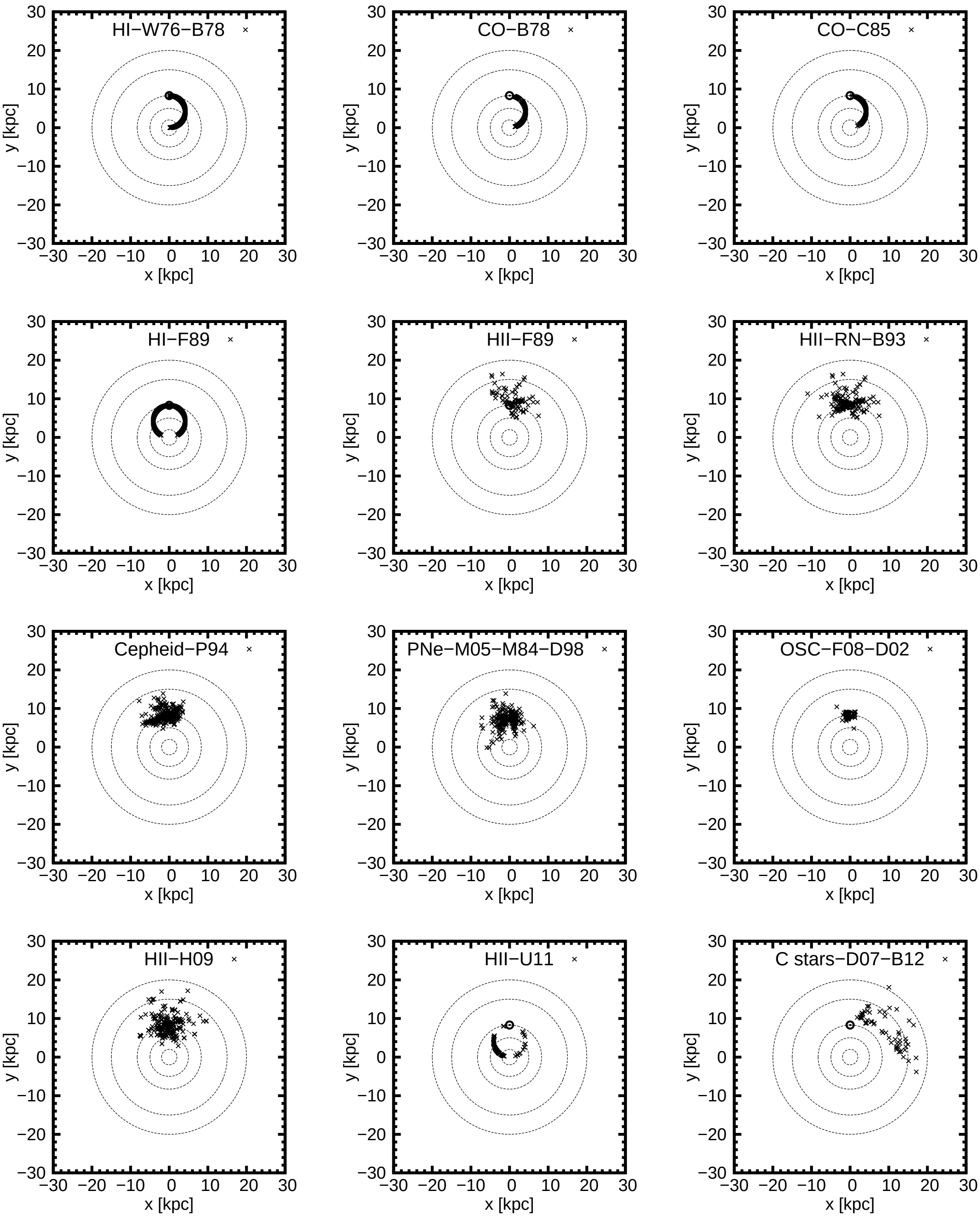


Figure 5.2: $x$–$y$ scatter plots for the different disk tracer samples listed in Table 5.1, for the case $\frac{R_0}{\mathrm{kpc}} = 8.3$. The Galactic Center is chosen to be at origin $(0, 0)$ with the Sun located at $(0,\, R_0)$.

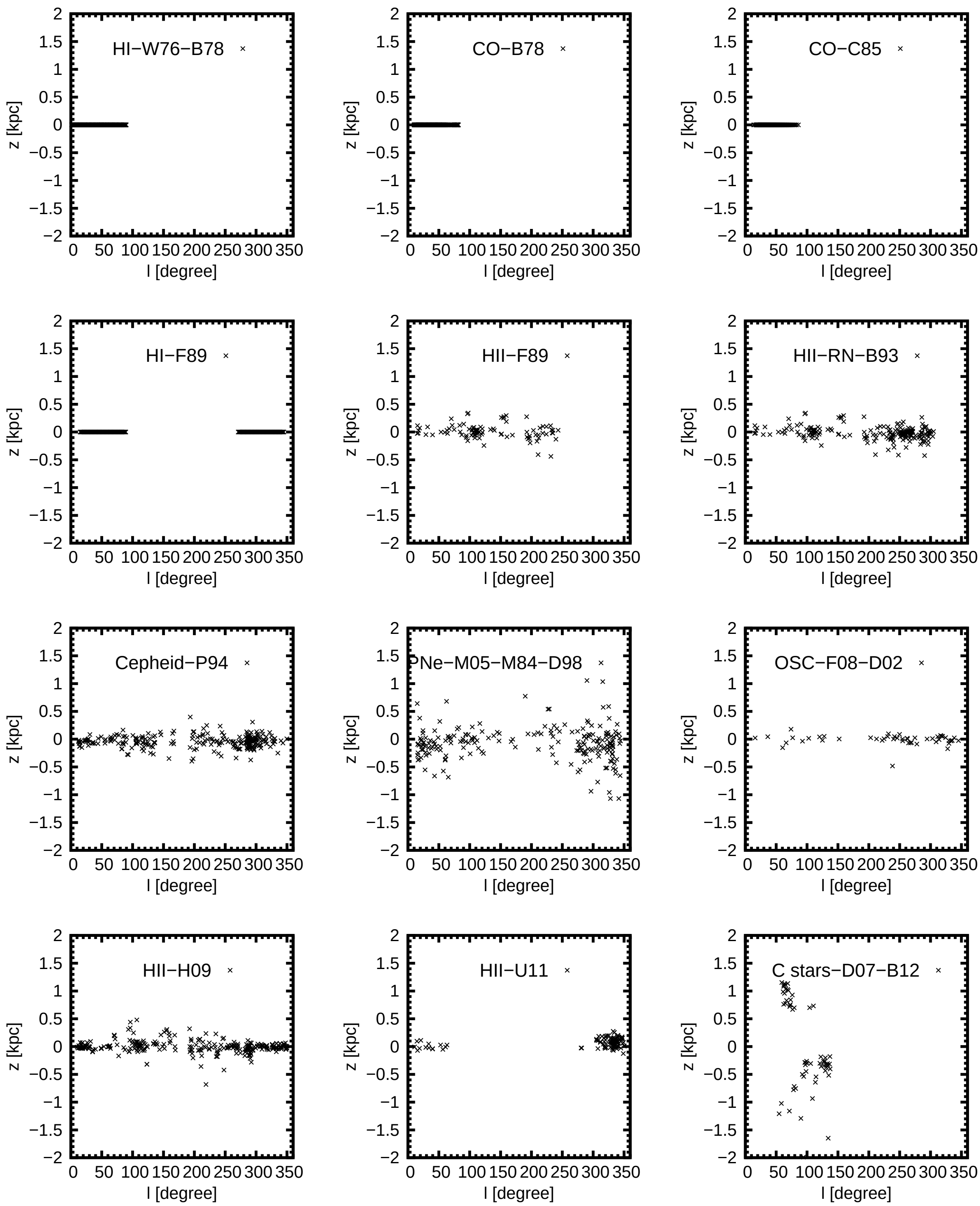


Figure 5.3: Galactic longitude, $l$ (x-axis), versus height from Galactic mid-plane, $z$ (y-axis), for the different disk tracer samples listed in Table 5.1, for the case $\frac{R_0}{\mathrm{kpc}} = 8.3$.

values of GCs, consistent with observations of masers and stellar orbits around SgrA* mentioned above, is $\left[\frac{R_0}{\mathrm{kpc}}, \frac{V_0}{\mathrm{km\,s^{-1}}}\right] = [8.3,\ 244]$ (see Refs: [107, 84]).

In general, as easily seen from Equation (5.7), given a $V_c(R)$ data, for a certain set of values of GCs as $[R_0,\ V_0]$, one can obtain the new RC, $\tilde{V}_c(R)$, for another set of values of the GCs denoted by $[\tilde{R}_0,\ \tilde{V}_0]$, through the relation

$$\tilde{V}_c(R) = \frac{R_0}{\tilde{R}_0}\left[V_c(R) - \frac{R}{R_0}\left(V_0 - \tilde{V}_0\right)\right] . \tag{5.14}$$

In order to illustrate the dependence of the RC on the choice of the GCs, in this chapter we shall calculate RCs with three different sets of values of $\left[\frac{R_0}{\mathrm{kpc}}, \frac{V_0}{\mathrm{km\,s^{-1}}}\right]$, namely, the set [8.3, 244] mentioned above as well as two other sets, namely, the IAU recommended set [8.5, 220] and the set [8.0, 200] (see Ref: [7]).

Figure 5.4 shows our calculated RCs for the disk region of the Galaxy for each of the different tracer samples listed in Table 5.1 for the GCs set $\left[\frac{R_0}{\mathrm{kpc}}, \frac{V_0}{\mathrm{km\,s^{-1}}}\right] = [8.3,\ 244]$. The top panel of Figure 5.5 shows the RCs obtained by taking the weighted averages of the combined $V_c$ data from all the samples shown in Figure 5.4, for three different sets of values of the GCs as indicated.

The circular velocities and their errors for individual disk tracer samples displayed in the top panel of Figure 5.5 are obtained in the following way: For each tracer object in a given sample we calculate $V_c$ and $R$ for the object from the known position coordinates of the object and its measured *los* velocity as described above. We then bin the resulting data ($V_c$ vs. $R$) in $R$, and in each $R$ bin calculate the mean of all the $V_c$ values of all the objects contained within that bin and assign it to the mean $R$ value of the objects in that bin. The error bars on $V_c$ correspond

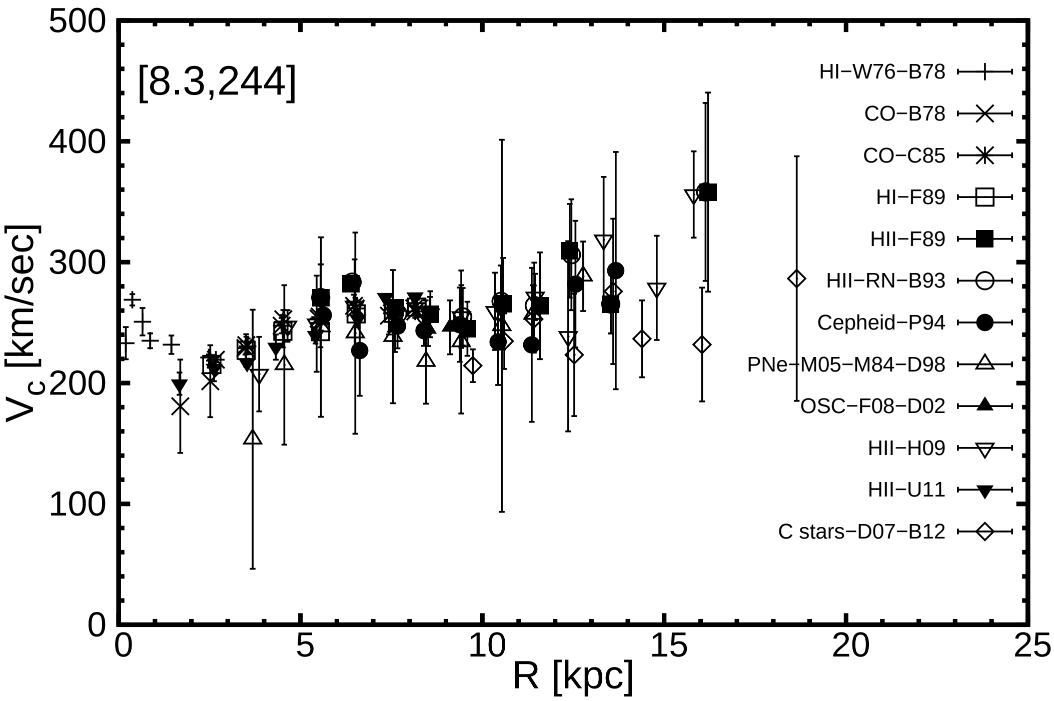


Figure 5.4: Rotation curve data of our Galaxy obtained using the various different disk tracer samples listed in Table 5.1 for the Galactic Constants $\left[\frac{R_0}{\mathrm{kpc}}, \frac{V_0}{\mathrm{km\,s^{-1}}}\right] =$ [8.3, 244].

simply to the standard deviation (s.d.) of the $V_c$ values in that bin [1]. We have taken a bin size of 0.25 kpc for $0 < R \leq 1$ kpc, 1.0 kpc for $1 < R \leq 15$ kpc, and 2.5 kpc for $15 < R \leq 17.5$ kpc. The objects with $R > 17.5$ kpc are few in number and are placed in one single bin. The above choices of the bin widths in $R$ for various ranges of $R$, arrived at by trial and error, are "optimal" in the sense that the bin widths are large enough so that there are sufficient number of objects in each bin (to allow the mean value of $V_c$ in the bin to be a reasonably good representative of the true value of $V_c$ at the value of $R$ under consideration), while at the same time being not too large as to miss the fine features of the RC. The RCs in the top panel of Figure 5.5 are obtained by combining the $V_c$ data from all the samples

[1] Note that the *los* velocities $v_{\mathrm{h}}$ of individual tracer objects are measured fairly accurately and their measurement errors contribute negligibly little to the final errors on the $V_c$ values.

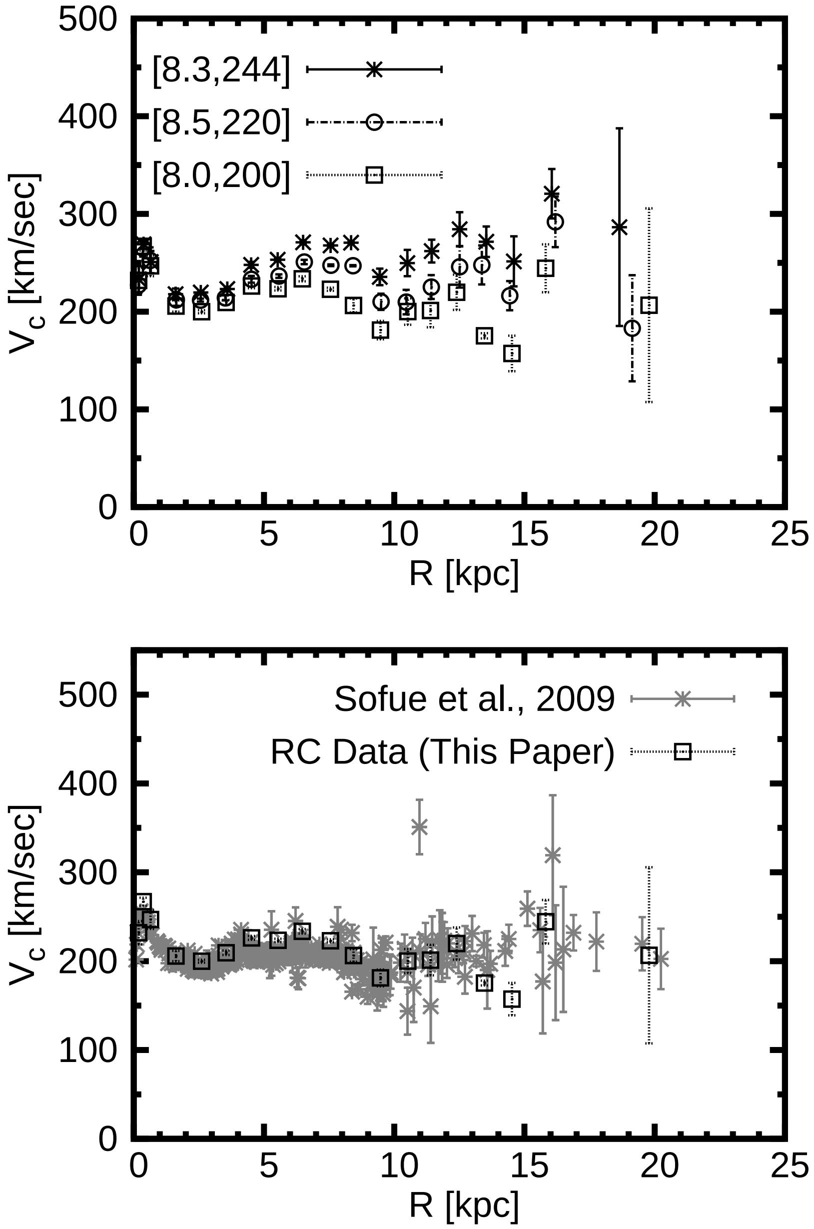


Figure 5.5: Top: Averaged Rotation Curves of the Galaxy for the three different sets of values of $\left[\frac{R_0}{\mathrm{kpc}}, \frac{V_0}{\mathrm{km\,s^{-1}}}\right]$ as indicated obtained using the various different disk tracer samples listed in Table 5.1. Bottom: Averaged Rotation Curve of the Galaxy for the Galactic Constants $\left[\frac{R_0}{\mathrm{kpc}}, \frac{V_0}{\mathrm{km\,s^{-1}}}\right] = [8.0,\, 200]$ compared to the data published by Sofue et al. [106] for the same Galactic Constants set.

shown in Figure 5.4 in the same $R$ bins as above and then calculating the mean circular speed ($V_c$) and its $1\sigma$ uncertainty ($\Delta V_c$) within each bin by the standard weighted average method [135]:

$$V_c = \frac{\sum_i w_i V_{c,i}}{\sum_i w_i}\,, \quad \text{and} \quad \Delta V_c = \sqrt{\frac{1}{\sum_i w_i}}\,, \tag{5.15}$$

with $w_i = 1/(\Delta V_{c,i})^2$, where $V_{c,i}$ and $\Delta V_{c,i}$ are the $V_c$ value and its $1\sigma$ error, respectively, of the $i$-th data point within the bin.

As seen from the top panel in Figure 5.5, the RC in the disk region seems to have dips around $\sim 3$ and 9 kpc and depends significantly on the choice of GCs. Particularly, at any given R the circular velocity is higher for higher value of $V_0$. The bottom panel of the Figure 5.5 shows a comparison of the averaged RC obtained here for the GCs set $\left[\frac{R_0}{\mathrm{kpc}}, \frac{V_0}{\mathrm{km\,s^{-1}}}\right] = [8.0,\, 200]$ to that published in an earlier work by Sofue et al. [106] that used the same GCs set values. Our data are in reasonable good agreement with those reported by Sofue et al. At the same time, we note that our error bars are significantly smaller than those of Sofue et al. [106], which we attribute to our better statistical estimates due to large variety of tracer samples used in our analysis.

In order to extract information on the phase space structure of the DM halo of our Galaxy we need to extend the RC up to large galactocentric distances since it's the DM that dominates the galactic mass at large galactocentric distances. This can be done by using data sets on distant tracers like Blue Horizontal Branch stars, K Giant stars and relatively rare tracer objects like Globular Clusters, dwarf spheroidal galaxies and so forth, populating the DM halo beyond the disk out to galactocentric distances of several hundreds of kpc. The method of deriving the RC using non-disk tracers are different from that discussed in section 5.2 since these tracers do not follow any systematic circular motion like tracers populating the disk. Recently, we have derived the RC in the non-disk region (discussed in detail in [136]) and published [8] an unified RC $\sim 0.2$ kpc up to $\sim 200$ kpc combining with the disk RC data derived in this chapter. The full RC data so obtained for GCs set $\left[\frac{R_0}{\mathrm{kpc}}, \frac{V_0}{\mathrm{km\,s^{-1}}}\right] = [8.3\ ,\ 244]$ is presented in Table: 5.2. An important feature of this unified RC is that it declines beyond about $\sim 60$ kpc, as would be expected of an effectively finite size of the DM halo of the Galaxy.

## 5.4 Summary

In this chapter, we have presented the results pertaining to the construction of the RC of our Galaxy from a galactocentric distance of $\sim 0.2$ kpc out to $\sim 20$ kpc using kinematical data on a wide variety of disk objects that trace the gravitational potential of the Galaxy, without assuming any theoretical models of the VM and DM components of the Galaxy. The results seem are in overall good agreement with published data in literature, but out results have smaller uncertainties in the circular velocity values. We have studied the dependence of the disk RC on the choice of the GCs and found that at a given galactocentric distance, R, the derived disk circular velocity, $\mathrm{V_c(R)}$, varies directly with the value of $V_0$. However, upcoming data on positions, proper motions, distances and photometric data of $\sim$ few billion stars in our Galaxy from satellite missions like Gaia [137] will enable us to construct more accurate RCs with less systemic errors.

Table 5.2: The rotation curve data, $V_c$, up to $\sim 200$ kpc and its 1-$\sigma$ error, $\Delta V_c$, for various values of the galactocentric distance, R, for Galactic Constants $\left[\frac{R_0}{\mathrm{kpc}}, \frac{V_0}{\mathrm{km\,s^{-1}}}\right]$ = [8.3,244] [8].

| $R$ (kpc) | $V_c$ ($\mathrm{km\,s^{-1}}$) | $\Delta V_c$ ($\mathrm{km\,s^{-1}}$) | $R$ (kpc) | $V_c$ ($\mathrm{km\,s^{-1}}$) | $\Delta V_c$ ($\mathrm{km\,s^{-1}}$) |
|---|---|---|---|---|---|
| 0.20 | 233.0 | 13.32 | 38.41 | 191.57 | 11.73 |
| 0.38 | 268.92 | 4.67 | 40.42 | 197.59 | 14.12 |
| 0.66 | 250.75 | 11.35 | 42.40 | 192.79 | 5.92 |
| 1.61 | 217.83 | 5.81 | 44.49 | 213.22 | 17.17 |
| 2.57 | 219.58 | 1.48 | 45.99 | 179.39 | 11.23 |
| 3.59 | 223.11 | 2.43 | 48.06 | 213.03 | 24.72 |
| 4.51 | 247.88 | 2.99 | 49.49 | 178.57 | 17.63 |
| 5.53 | 253.14 | 1.69 | 51.39 | 183.31 | 23.58 |
| 6.50 | 270.95 | 2.19 | 53.89 | 157.89 | 19.57 |
| 7.56 | 267.80 | 0.96 | 56.89 | 191.76 | 24.35 |
| 8.34 | 270.52 | 0.66 | 57.98 | 210.72 | 29.81 |
| 9.45 | 235.58 | 8.44 | 60.92 | 168.02 | 25.67 |
| 10.50 | 249.72 | 13.44 | 64.73 | 206.47 | 36.27 |
| 11.44 | 261.96 | 11.71 | 69.31 | 203.62 | 40.89 |
| 12.51 | 284.30 | 17.50 | 72.96 | 190.53 | 40.98 |
| 13.53 | 271.54 | 15.57 | 76.95 | 222.72 | 74.37 |
| 14.59 | 251.43 | 25.60 | 81.13 | 186.29 | 66.53 |
| 16.05 | 320.70 | 25.27 | 84.90 | 122.25 | 36.46 |
| 18.64 | 286.46 | 101.18 | 89.35 | 143.95 | 29.49 |
| 26.30 | 189.64 | 6.74 | 92.44 | 154.66 | 67.23 |
| 28.26 | 237.99 | 11.54 | 97.41 | 184.0 | 72.86 |
| 29.51 | 209.82 | 9.16 | 100.72 | 108.68 | 40.99 |
| 32.04 | 179.14 | 6.65 | 106.77 | 137.15 | 53.17 |
| 33.99 | 170.37 | 6.93 | 119.98 | 150.18 | 25.46 |
| 36.49 | 175.92 | 6.62 | 189.49 | 125.01 | 37.32 |

# Chapter 6

# Local Density of the Dark Matter Particles in the Galaxy from Rotation Curve Data

## 6.1 Introduction

As mentioned in Chapter 2, the knowledge of local density, $\rho_{\mathrm{DM},\odot}$, and the local velocity distribution function (VDF) of the dark matter (DM) particles constituting the halo of our Galaxy are crucial for interpreting the results of DM direct detection (DD) experiments [15, 51]. One of the approaches in determining $\rho_{\mathrm{DM},\odot}$ is to use the kinematics of stars in the Solar neighborhood perpendicular to the Galactic disk. Here, one uses the one dimensional (in direction perpendicular to the disk) Jeans equation and Poisson's equation to obtain a relationship involving the measured stellar density and vertical velocity dispersion and the total matter density. Finally, by separately estimating local visible matter (VM) content, one can obtain the local DM density. As a second approach, one can consider mass modeling of the Galaxy using rotation curve (RC) data or kinematics of high velocity stars, etc by starts by adopting suitable density profiles for VM as well as the DM halo of the Galaxy and then determine the parameters of the model by fitting to relevant observational data. In this chapter we shall follow the second approach to determine the value of $\rho_{\rm DM,\odot}$.

There have been many earlier attempts to derive limits on $\rho_{\rm DM,\odot}$ from a variety of considerations. However, there is a large range of uncertainty on the values of $\rho_{\rm DM,\odot}$ obtained by different methods. A wide range of values have been quoted in literature including local and global measures [24]-[34],[138]-[150]. For a recent comprehensive review, see [151].

In this chapter, we determine the parameters ($\rho_{\rm DM,\odot}$ being one of them) of an assumed form of the VM and DM halo density profiles, by fit to a rotation curve (RC) data set of our Galaxy extending from $\sim 0.2$ kpc up to $\sim 200$ kpc [8]. We use the Markov Chain Monte Carlo (MCMC) [152] analysis to determine the best fit parameters and the uncertainty ranges by fitting to the RC data for three different Galactic Constants (GCs) sets, namely, $\left[\frac{R_0}{\rm kpc}, \frac{V_0}{\rm km\,s^{-1}}\right]$ = [8.3, 244], [8.5, 220] and [8.0, 200].

In the following sections, we first describe the density models (both VM and DM) used for this mass modeling exercise and present a short description of the MCMC formalism. Finally, we present our results and summarize at the end.

## 6.2 Visible Matter Model

For the present analysis, we use the form of the VM distribution taken as a spherical bulge superposed on a double exponential disk [85] given in Equations (3.14) and (3.15) and parameters as defined in Section 3.2.

The prior ranges on VM parameter set for MCMC runs are taken as follows:-
Bulge central density ($\rho_{b0}$): [0.5-3]$\times$ 4.2 $\times$ $10^2$ $M_\odot \mathrm{pc}^{-3}$ [85],
bulge scale radius ($r_b$): [0.5-2]$\times$ 0.103 kpc [85],
local disk visible matter surface density ($\Sigma_\odot$): [35-58]$\times$ $M_\odot \mathrm{pc}^{-2}$ [32],
disk scale length ($R_d$): [1.5-5] kpc consistent with [153].
However, the disk scale height ($z_h$) has been kept fixed at 0.3 kpc since the results are fairly insensitive to this parameter.

## 6.3 Dark Matter Models

We choose four density models all of which can serve as a good description of the DM halo as observed in N-body simulations. These are given below. In all these expressions of $\rho_{\mathrm{DM}}$ given below, $r_s$ is the scale radius of the system and $R_0$ is the distance of Sun from the Galactic center.

**Navarro-Frenk-White Model**:
The Navarro-Frenk-White (NFW) density profile [154]-[156] is given by

$$\rho_{\mathrm{DM}}(r) = \rho_{\mathrm{DM},\odot} \frac{R_0}{r} \left( \frac{r_s + R_0}{r_s + r} \right)^2 . \tag{6.1}$$

This was first proposed as the universal profile that can nicely describe the DM halos obtained in numerical N-body simulations. Evidently, this two parameter profile shows a cuspy behavior for small r, where $\rho_{\rm DM}(r)$ varies as $\propto r^{-1}$ and varies as $\propto r^{-3}$ for larger radii.

**Hernquist Model**:

Hernquist density profile [157, 158] has the form,

$$\rho_{\rm DM}(r) = \rho_{{\rm DM},\odot}\frac{R_0}{r}\left(\frac{r_s + R_0}{r_s + r}\right)^3. \tag{6.2}$$

It is also a two parameter density profile. Similar to the NFW model, this profile too shows a cuspy behavior for small $r$ where $\rho_{\rm DM}(r)$ varies as $\propto r^{-1}$ and varies as $\propto r^{-4}$ for larger radii.

**Einasto Model**:

Einasto density profile [159]-[161] can be written as,

$$\rho_{\rm DM}(r) = \rho_{{\rm DM},\odot}e^{-2s_n[(r/r_s)^{\frac{1}{s_n}} - (R_0/r_s)^{\frac{1}{s_n}}]} \tag{6.3}$$

where $s_n$ is the shape parameter. This model can account for cored as well as cuspy profiles (though with a finite central density unlike NFW), controlled by the shape parameter $s_n$.

**Burkert Model**:

Burkert density profile [162] has the form

$$\rho_{\rm DM}(r) = \rho_{{\rm DM},\odot}\frac{(r_s + R_0)(r_s^2 + R_0^2)}{(r_s + r)(r_s^2 + r^2)}. \tag{6.4}$$

This two parameter model has a density profile with a constant core while the $\rho_{\rm DM}(r)$ varies as $\propto r^{-3}$ for larger radii like NFW.

For each of the halo models we define the virial radius, $r_{vir}$, as the radius within which the average DM density is 200 times the critical density of Universe. For a given virial radius, the total mass contained within that radius is calculated using Equation (4.10) by putting $r = r_{vir}$ and $\rho = \rho_{\rm DM} + \rho_{VM}$. The local surface mass density of DM on the equatorial plane is calculated by integrating the halo density over $|z| \leq 1.1\,{\rm kpc}$ using,

$$\Sigma_{\rm DM} = \int_{-z}^{+z} \rho_{\rm DM}(\mathbf{x}) dz'. \tag{6.5}$$

The prior ranges on DM parameter set for our MCMC runs have been kept wide enough and are as follows:-

$\rho_{\rm DM,\odot}$: 0.01-1 $\,{\rm GeV\,cm^{-3}}$, $r_s$: 1-150 kpc, $s_n$: 0.5-7.

## 6.4 Markov Chain Monte Carlo analysis

Having specified the VM and DM density profiles in Section 6.2 and 6.3, for a given parameter set, we can calculate the respective gravitational potentials by solving the Poisson's equations (Equation 3.12) with the boundary conditions given in Equation (3.13) and solve for the theoretical RC as a function of the galactocentric distance $R$, using Equation (3.11). Our motive to use the time efficient MCMC analysis is to determine the most likely values and the uncertainties in the VM and DM parameters by fitting with a given set of RC data. [1] The RC data extending from $\sim 0.2$ kpc up to $\sim 200$ kpc for three different GCs sets [8] have been used to calculate the $\chi^2$ [see Equation (3.20)] used as a test statistic for the MCMC analysis.

Bayesian inference, as we use here, is a method of statistical inference in which evidence (RC data here) is used to estimate parameters (say $n$ parameters) and predictions in a probability model. In Bayesian inference, all uncertainty is summarized by a “posterior distribution function” (PDF) which is a probability distribution for all uncertain quantities (i.e., the parameters), given the data and the model. Consider a model $g$ depending on n parameters,

$$g = g(a) \quad \text{where} \quad a \equiv [a(1), a(2)....a(n)]. \tag{6.6}$$

We aim to determine the conditional PDF of the parameters, P(a|data), given the data. This posterior probability quantifies the change in the degree of belief one can have in the $n$ parameters of the model in the light of the data. Bayes theorem can be expressed as,

$$P(\mathrm{a}|\mathrm{data}) = \frac{\mathrm{P(data|a)P(a)}}{\mathrm{P(data)}}, \tag{6.7}$$

where P(data) is the data probability which does not depend on the parameters and hence can be considered to be a normalization factor. This theorem links the posterior probability to the likelihood of the data, L(a) $\equiv$ P(data|a) and the so-called prior probability, P(a), indicating the degree of belief one has before observing the data. Having determined the posterior PDF, P(a|data), to extract

[1] However, this parameter estimation exercise can also be performed in principle by using grid method analysis but that will be highly time consuming with increasing dimension of parameter space. For e.g., if a certain run consumes $m$ seconds, then to scan a $n$ dimensional parameter space with each parameter divided into $M$ values, the total computation time is $\sim m \times M^n$.

information about a single parameter, $a(j)$ , the posterior density is integrated over all other $n-1$ parameters $a(k \neq j)$ in a procedure called marginalization. Finally, by integrating the individual posterior PDF further, we are able to determine the expectation value, confidence level, or higher order modes of the parameter $a(j)$. There is a technical difficulty in Bayesian parameter estimations: determining the individual posterior PDF requires a high-dimensional integration of the overall posterior density. Thus, an efficient sampling method for the posterior PDF is mandatory. MCMC methods explore the probability distribution of a $n$ dimensional parameter space, where each point can be represented by a vector $a$ by generating a sequence of $i$ points (hereafter a chain). Each position of $a$ is a vector of $n$ components, each representing one parameter value, in the $n$-dimensional parameter space.

For our problem, we run several chains for 1,00,000 chain length i.e., each sampling the parameter space 1,00,000 times in a random manner via a given $n \times n$ dimension proposal matrix, limited by the flat priors set on each of the parameters. In addition, the chain is Markovian in the sense that the condition to accept the randomly chosen $(i+1)^{th}$ position in the parameter space is solely decided by the $i^{th}$ position. The prescription that we use to generate the Markov chains by random sampling of the parameter space is the so-called Metropolis-Hastings algorithm [163, 164]. For each new position, our MCMC algorithm calculates a quantity $\alpha = e^{-0.5(\chi^2_{i+1} - \chi^2_i)}$ where $\chi^2_i$ denotes the test statistic [see Equation (3.20)] for $i^{th}$ position of the chain. According to Metropolis-Hastings algorithm, if $\alpha > 1$, the new position is accepted, else a random number generator is employed to generate any number $\zeta$ lying in the range, $0 \leq \zeta \leq 1$, from an uniform distribution. If $\alpha > \zeta$, the position is accepted, otherwise the chain stays in the $i^{th}$ position and again randomly jumps to another position in the parameter space and checks the acceptability by using the Metropolis-Hastings algorithm. Therefore, the time spent by the Markov chain in a region of the parameter space is proportional to the target PDF value in this region. Finally, for our analysis we collect about six or more chains with acceptance value of 20-25% and are analyzed by the 'getdist' programme supplied by the COSMOMC routine [165]. The analysis recalculates the proposal matrix which takes into account the different correlations between the parameters and gives a value of R. The quantity 'R' basically measures (variance of chain means)/(mean of variances), hence for convergence R should approach 1. We have set a value of $R - 1 < 0.1$ to be good a tolerance for convergence, and once we attain that, we adopt the resultant posterior probability distributions, best fit parameter sets, desired limits etc. obtained from the 'getdist' programme as our final result. If not, we replace the proposal matrix and re-run the chains till convergence is reached.

## 6.5 Results

In Figure 6.1, the colored plots show the 2D posterior probability density function for the Galactic DM halo parameters marginalized over the rest of the parameters and the black/white plots show the 1D probability distributions for the DM parameters where dotted line and solid line show the mean likelihood from all considered chains and the marginalized distribution for a given parameter, respectively. In the 2D plots, the black region denotes the area with higher probability (and contains the best fit points) and the probability values decrease with orange to yellow regions. Results are presented for the four DM halo models (NFW, Hernquist, Einasto and Burkert) using MCMC with Galactic rotation curve data [8] for three different sets of values for the GCs, $\left[\frac{R_0}{\text{kpc}}, \frac{V_0}{\text{km}\,\text{s}^{-1}}\right] = [8.3,\ 244], [8.5,\ 220]$ and $[8.0,\ 200]$. As is evident, with decreasing $V_0$ (towards right) the $\rho_{\text{DM},\odot}$ decreases, irrespective of the halo model considered.

The derived most likely values of $\rho_{\text{DM},\odot}$ along with their marginalized limits for mean and 1 $\sigma$ range for the four different DM halo models, for the three different sets of values of GCs are displayed in Figure 6.2. It is quite evident that the $\rho_{\text{DM},\odot}$ values are sensitive to the choice of GC, especially to the values of circular rotation speed of the local standard of rest frame around the Galactic center, $V_0$, irrespective of the nature of the DM halo model used (be it cored or cuspy). The best fit value of $\rho_{\text{DM},\odot}$ increases by about a factor of three from $\sim 0.2$ to $\sim 0.6$ $\text{GeV}\,\text{cm}^{-3}$ as $V_0$ changes from 200 to 244 $\text{km}\,\text{s}^{-1}$.

Table 6.1 shows the most-likely values of the DM halo model parameters, their mean $\pm$ one sigma values ($\mu \pm \sigma$), the $\chi^2$ values scaled by the degree of freedom (dof) i.e., number of RC data points, halo virial radius ($r_{vir}$), total virial mass ($M_{tot}(\leq r_{vir})$) and maximum speed at Solar location ($v_{max,\odot}$) [2] obtained for the four dark matter halo models by MCMC analysis using the Galactic rotation curve data [8] for three different sets of values of the GCs, $\left[\frac{R_0}{\text{kpc}}, \frac{V_0}{\text{km}\,\text{s}^{-1}}\right] = [8.3,\ 244], [8.5,\ 220]$ and $[8.0,\ 200]$, as indicated. Unlike the local quantity like $\rho_{\text{DM},\odot}$, the large scale quantities like total mass, halo virial radius etc. which are dependent on large distance behavior of the RC are seen to be uncorrelated with GCs values since RC data beyond disk regime are not sensitive to the GCs set adopted [8].

[2]Since these halo profiles have infinite extent, the maximum particle speed at any location is given by, $v_{\max}(\mathbf{x}) = \sqrt{2\left[\Phi_{\text{tot}}(|\mathbf{x}| = \infty) - \Phi_{\text{tot}}(\mathbf{x})\right]}$ where, $\Phi_{\text{tot}}(\mathbf{x}) = \Phi_{\text{DM}}(\mathbf{x}) + \Phi_{\text{VM}}(\mathbf{x})$.

For all the three GCs sets, Figures 6.4 and 6.3 show the density- and RC profiles for the best fit set of parameters for the four DM halo models. Figures 6.5 and 6.6 show the best fit mass- and maximum speed profiles, for the same DM halo models.

## 6.6 Summary

In this chapter, fit to the RC data of our Galaxy extending up to $\sim 200$ kpc, for three different sets of values of the GCs sets $\left[\frac{R_0}{\mathrm{kpc}}, \frac{V_0}{\mathrm{km\,s^{-1}}}\right] = [8.3{,}244]$, $[8.5{,}220]$ and $[8.0{,}200]$ have been used to determine the parameters for four DM halo profiles (NFW, Hernquist, Einasto and Burkert) considering a standard VM density distribution by an extensive MCMC analysis. The derived best fit values of $\rho_{\mathrm{DM},\odot}$ marginalized over all the rest of DM and VM parameters, show a monotonic behavior with the $V_0$ value of the chosen GCs set. This feature is generic, i.e., independent of the DM halo model type employed for the analysis. We will therefore, choose a particular halo model, namely the Einasto profile, to represent the DM halo of our Galaxy for our successive calculations. The local DM density is uncertain by a factor of $\sim 3$, roughly changing from $\sim 0.2$ to $\sim 0.6$ $\mathrm{GeV\,cm^{-3}}$ for $V_0$ changing from 200 to 244 $\mathrm{km\,s^{-1}}$. The large scale quantities like total mass, virial radius etc. which are dependent on large distance behavior of the RC are seen to be uncorrelated with the GCs since RC data beyond disk regime are not sensitive to GCs set adopted [8].

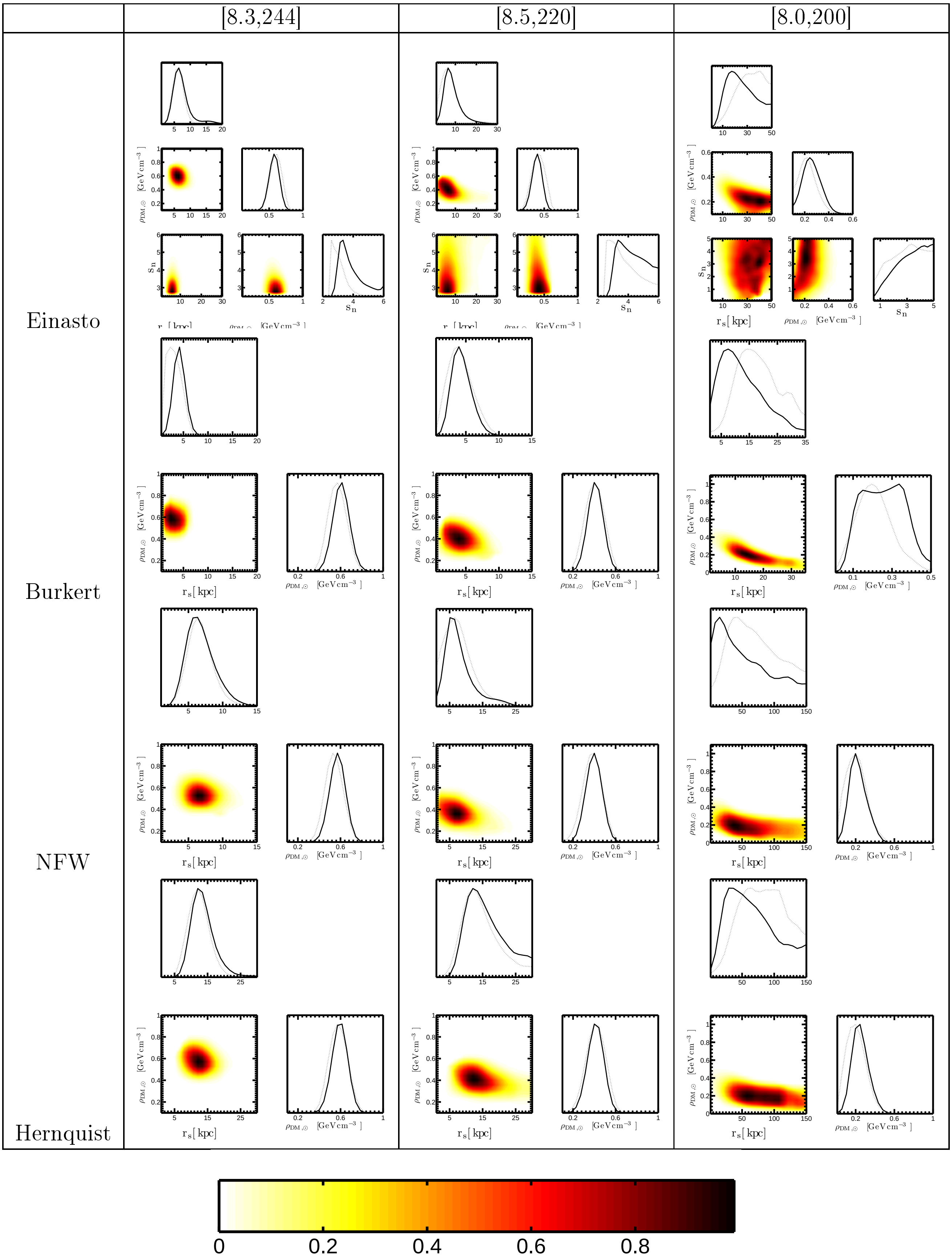


Figure 6.1: 2D posterior probability density function (colored plots) for the Galactic dark matter (DM) halo parameters (local DM density: $\rho_{\mathrm{DM},\odot}$, halo scale radius: $r_s$ and shape parameter: $s_n$) marginalized over the rest of the parameters. The black/white plots shows the 1D probability distributions for the DM parameters where dotted line and solid line show the mean likelihood and the marginalized distribution, respectively. The color code is shown along the horizontal bar at the bottom. Results are given for four different Galactic dark matter halo models (NFW, Hernquist, Einasto and Burkert) using Markov Chain Monte Carlo analysis with Galactic rotation curve data [8] for three different sets of values of the Galactic Constants, as $\left[\frac{R_0}{\mathrm{kpc}}, \frac{V_0}{\mathrm{km\,s^{-1}}}\right] = [8.3,\ 244], [8.5,\ 220]$ and $[8.0,\ 200]$ as indicated.

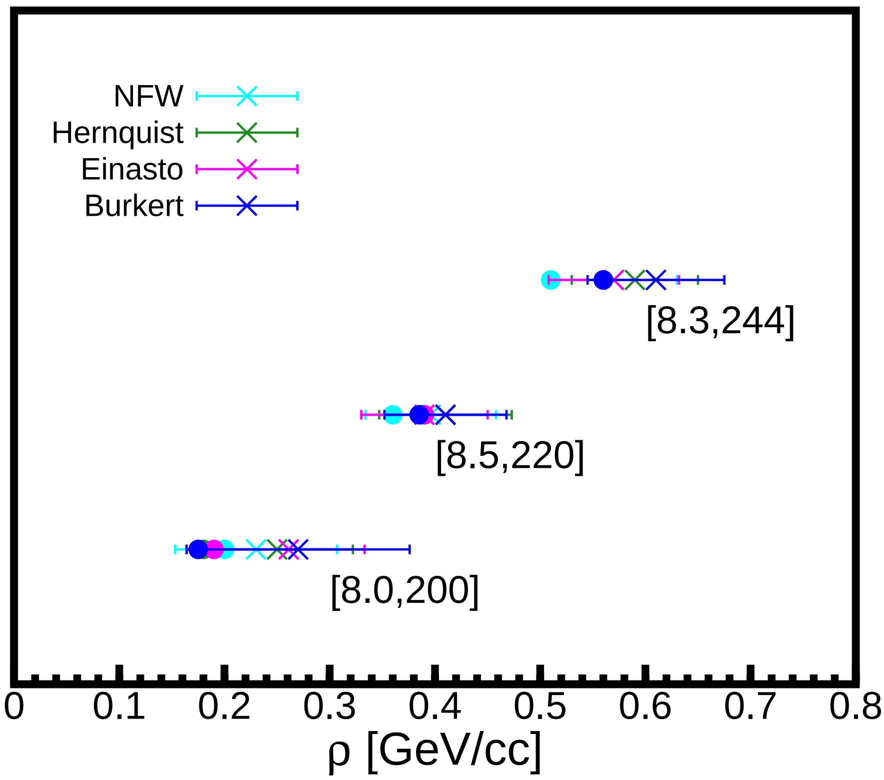


Figure 6.2: Best fit (circles) and marginalized limits ($\mu \pm \sigma$) (crosses with error bars) for local dark matter density (denoted by $\rho$) for four different Galactic dark matter halo models (NFW, Hernquist, Einasto and Burkert) obtained by fit to Galactic rotation curve data [8] using Markov Chain Monte Carlo analysis for three different sets of values of the Galactic Constants, $\left[\frac{R_0}{\text{kpc}}, \frac{V_0}{\text{km s}^{-1}}\right] = [8.3,\ 244], [8.5,\ 220]$ and $[8.0,\ 200]$ as indicated.

| GCs sets | parameters | Best-fit | $\mu \pm \sigma$ | $\chi^2$/dof | $r_{vir}$ (kpc) | $M_{tot}(\leq r_{vir})$ ($M_\odot \times 10^{11}$) | $v_{max,\odot}$ ($\mathrm{km\,s^{-1}}$) |
|---|---|---|---|---|---|---|---|
| | | | **NFW** | | | | |
| [8.3, 244] | $r_s$ (kpc) | 5.8 | 6.8 ± 1.99 | 10.469 | 191 | 7.8 | 566 |
| | $\rho_{DM,\odot}$ ($\mathrm{GeV\,cm^{-3}}$) | 0.51 | 0.57 ± 0.06 | | | | |
| [8.5, 220] | $r_s$ (kpc) | 5.7 | 8.1 ± 4.2 | 3.967 | 169 | 5.7 | 505 |
| | $\rho_{DM,\odot}$ ($\mathrm{GeV\,cm^{-3}}$) | 0.36 | 0.396 ±0.062 | | | | |
| [8.0, 200] | $r_s$ (kpc) | 42.5 | 57.82 ±40.8 | 5.322 | 241 | 14.9 | 560 |
| | $\rho_{DM,\odot}$ ($\mathrm{GeV\,cm^{-3}}$) | 0.2 | 0.23 ±0.077 | | | | |
| | | | **Hernquist** | | | | |
| [8.3, 244] | $r_s$ (kpc) | 12.1 | 13.6 ± 3.35 | 7.75 | 163 | 5.3 | 541 |
| | $\rho_{DM,\odot}$ ($\mathrm{GeV\,cm^{-3}}$) | 0.56 | 0.59 ± 0.06 | | | | |
| [8.5, 220] | $r_s$ (kpc) | 14.3 | 15.998 ± 5.57 | 3.553 | 157 | 4.5 | 492 |
| | $\rho_{DM,\odot}$ ($\mathrm{GeV\,cm^{-3}}$) | 0.39 | 0.41 ± 0.063 | | | | |
| [8.0, 200] | $r_s$ (kpc) | 79.7 | 66.7 ± 36.4 | 5.153 | 223 | 12.0 | 528 |
| | $\rho_{DM,\odot}$ ($\mathrm{GeV\,cm^{-3}}$) | 0.18 | 0.25 ± 0.072 | | | | |
| | | | **Einasto** | | | | |
| [8.3, 244] | $r_s$ (kpc) | 5.74 | 7.35 ± 2.81 | 7.57 | 157 | 4.5 | 532 |
| | $\rho_{DM,\odot}$ ($\mathrm{GeV\,cm^{-3}}$) | 0.56 | 0.57 ± 0.062 | | | | |
| | $s_n$ | 3.09 | 3.97 ± 0.94 | | | | |
| [8.5, 220] | $r_s$ (kpc) | 6.95 | 8.76 ± 4.17 | 3.56 | 145 | 3.9 | 482 |
| | $\rho_{DM,\odot}$ ($\mathrm{GeV\,cm^{-3}}$) | 0.39 | 0.39 ± 0.06 | | | | |
| | $s_n$ | 3.01 | 4.29 ± 0.86 | | | | |
| [8.0, 200] | $r_s$ (kpc) | 36.97 | 25.69 ± 11.35 | 5.15 | 214 | 11.4 | 525 |
| | $\rho_{DM,\odot}$ ($\mathrm{GeV\,cm^{-3}}$) | 0.19 | 0.261 ± 0.072 | | | | |
| | $s_n$ | 3.08 | 3.26 ± 1.14 | | | | |
| | | | **Burkert** | | | | |
| [8.3, 244] | $r_s$ (kpc) | 3.89 | 4.18 ± 0.81 | 4.91 | 176 | 6.5 | 554 |
| | $\rho_{DM,\odot}$ ($\mathrm{GeV\,cm^{-3}}$) | 0.56 | 0.61 ± 0.065 | | | | |
| [8.5, 220] | $r_s$ (kpc) | 4.4 | 4.38 ± 1.32 | 2.90 | 157 | 5.1 | 499 |
| | $\rho_{DM,\odot}$ ($\mathrm{GeV\,cm^{-3}}$) | 0.385 | 0.41 ± 0.058 | | | | |
| [8.0, 200] | $r_s$ (kpc) | 16.79 | 12.5 ± 7.01 | 5.381 | 206 | 9.8 | 520 |
| | $\rho_{DM,\odot}$ ($\mathrm{GeV\,cm^{-3}}$) | 0.175 | 0.27 ± 0.106 | | | | |

Table 6.1: The most-likely values of the dark matter (DM) halo model parameters ($r_s$ is the scale radius of the system, $\rho_{DM,\odot}$ is local DM density and $s_n$ is the shape parameter), their mean ± one sigma values ($\mu \pm \sigma$), the $\chi^2$ values (scaled by the degree of freedom (dof) i.e., number of rotation curve data points), halo virial radius ($r_{vir}$), total virial mass ($M_{tot}(\leq r_{vir})$) and maximum speed at Solar location ($v_{max,\odot}$) are tabulated for four different Galactic DM halo models viz. NFW, Hernquist, Einasto and Burkert obtained by fit to Galactic rotation curve data [8] using Markov Chain Monte Carlo analysis for three different sets of values of the Galactic Constants, $\left[\frac{R_0}{\mathrm{kpc}}, \frac{V_0}{\mathrm{km\,s^{-1}}}\right]$ = [8.3, 244], [8.5, 220] and [8.0, 200] as indicated.

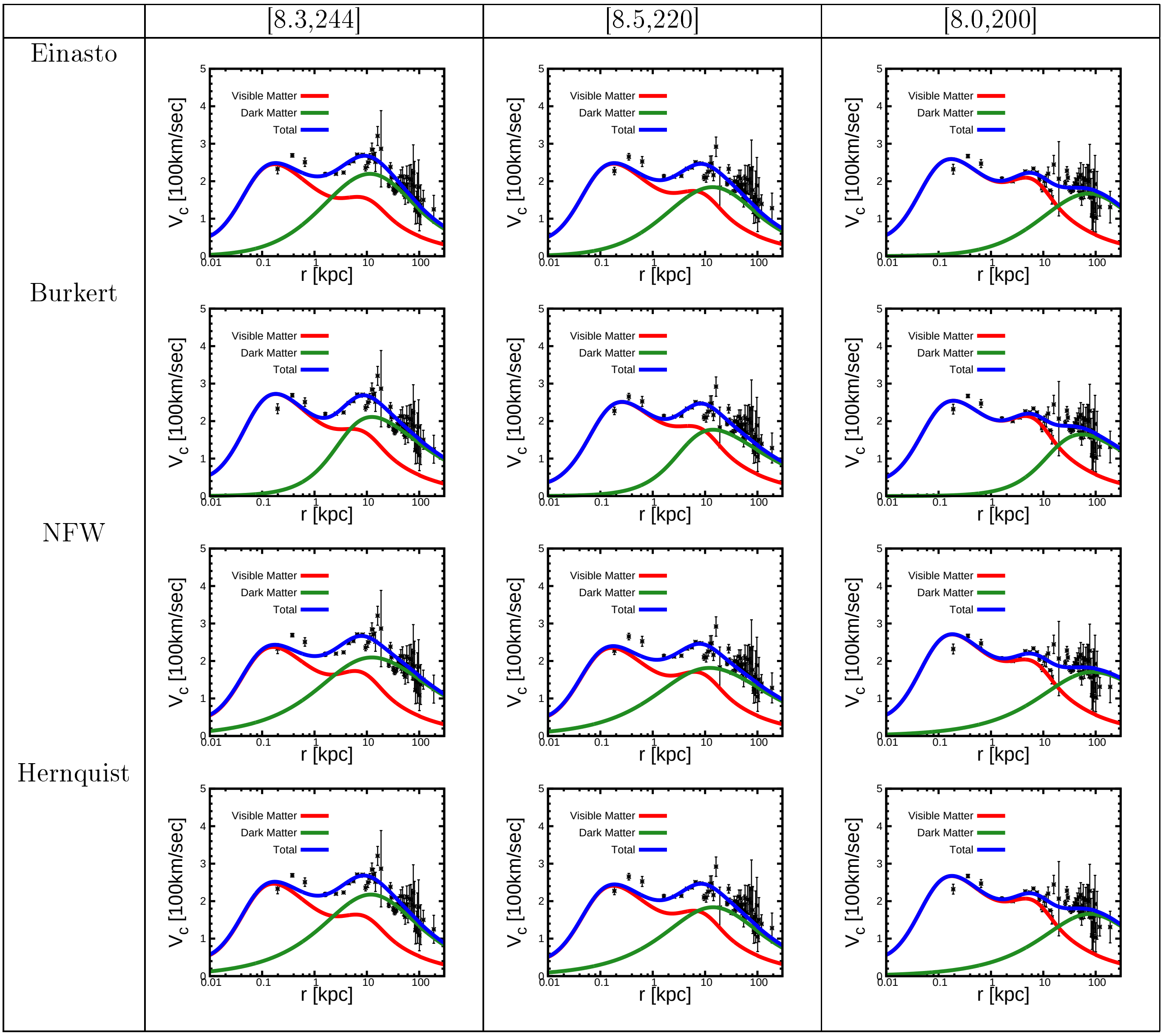


Figure 6.3: Best-fit rotation curves with visible matter (red line), dark matter (green line) and total matter (blue line) contributions shown for four different Galactic dark matter halo models (NFW, Hernquist, Einasto and Burkert) and assuming the same visible matter model [see Equations (3.14) and (3.15)] obtained by fit to Galactic rotation curve data [8] for three different sets of values of the Galactic Constants, $\left[\frac{R_0}{\mathrm{kpc}}, \frac{V_0}{\mathrm{km\,s^{-1}}}\right]$ = [8.3, 244], [8.5, 220] and [8.0, 200] as indicated.

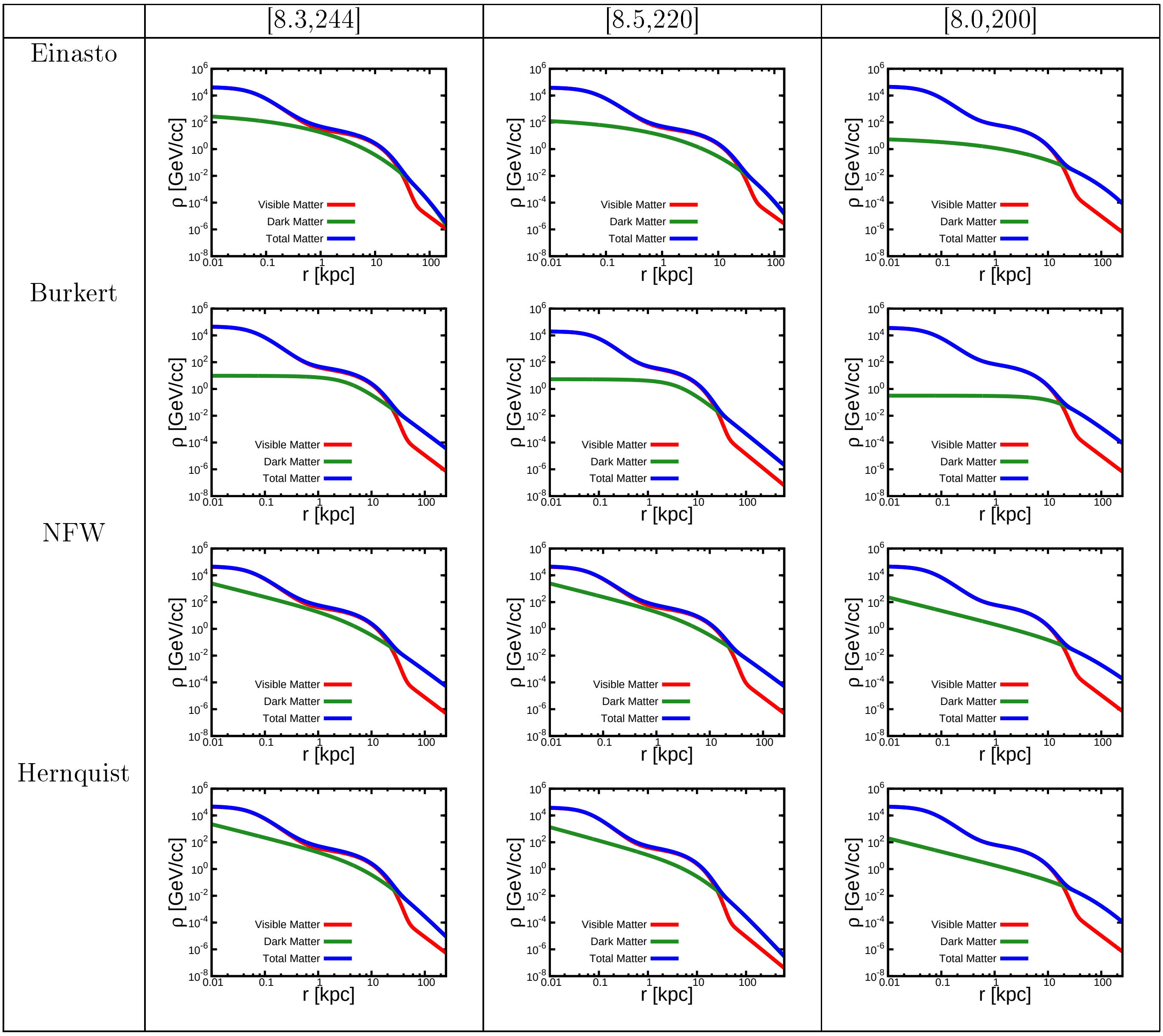


Figure 6.4: Best-fit density profiles with visible matter (red line), dark matter (green line) and total matter (blue line) contributions shown for four different Galactic dark matter halo models (NFW, Hernquist, Einasto and Burkert) and assuming the same visible matter model [see Equations (3.14) and (3.15)] obtained by fit to Galactic rotation curve data [8] for three different sets of values of the Galactic Constants, $\left[\frac{R_0}{\text{kpc}}, \frac{V_0}{\text{km s}^{-1}}\right]$ = [8.3, 244], [8.5, 220] and [8.0, 200] as indicated.

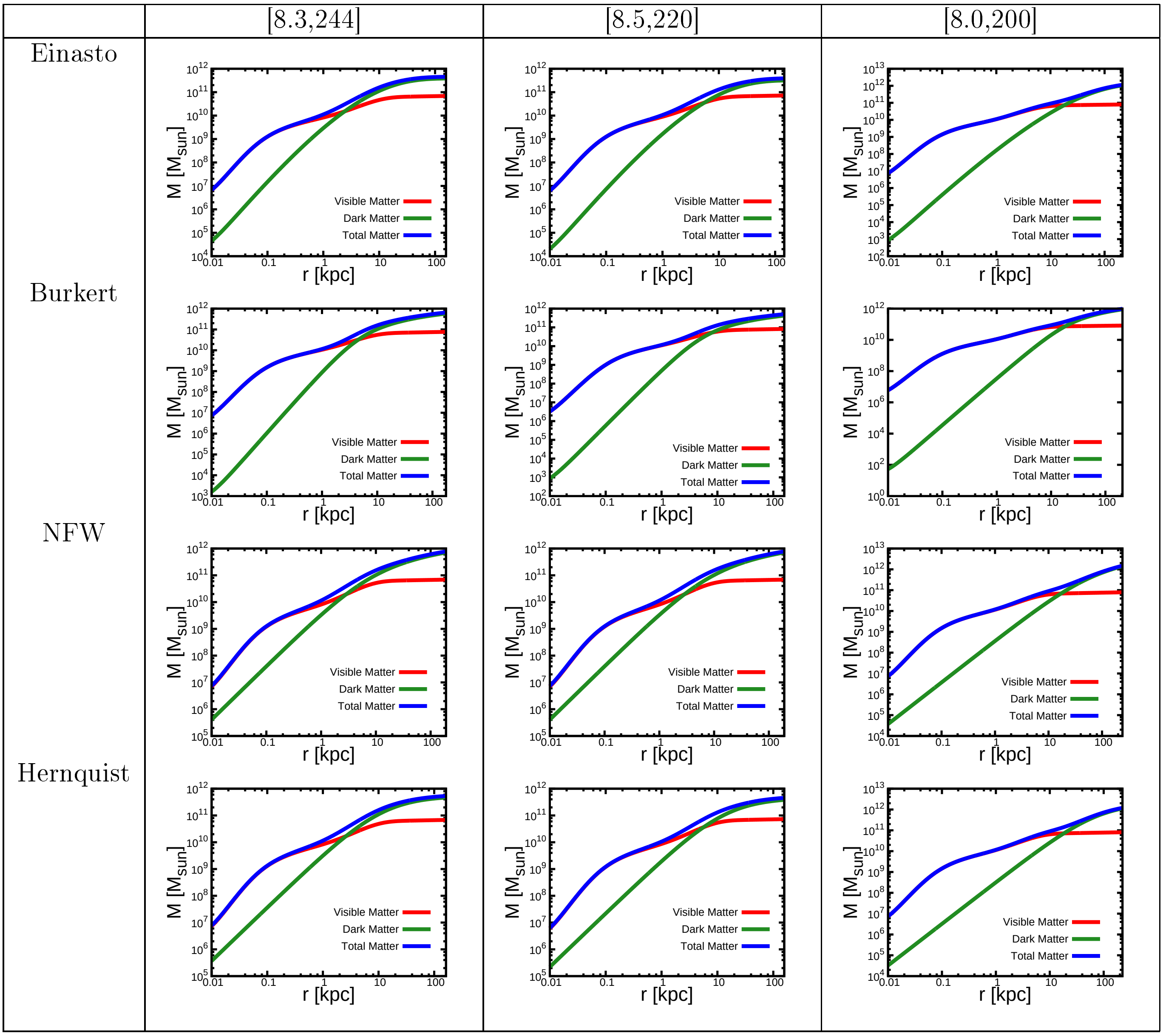


Figure 6.5: Best-fit mass profiles with visible matter (red line), dark matter (green line) and total matter (blue line) contributions shown for four different Galactic dark matter halo models (NFW, Hernquist, Einasto and Burkert) and assuming the same visible matter model [see Equations (3.14) and (3.15)] obtained by fit to Galactic rotation curve data [8] for three different sets of values of the Galactic Constants, $\left[\frac{R_0}{\mathrm{kpc}}, \frac{V_0}{\mathrm{km\,s^{-1}}}\right]$ = [8.3, 244], [8.5, 220] and [8.0, 200] as indicated.

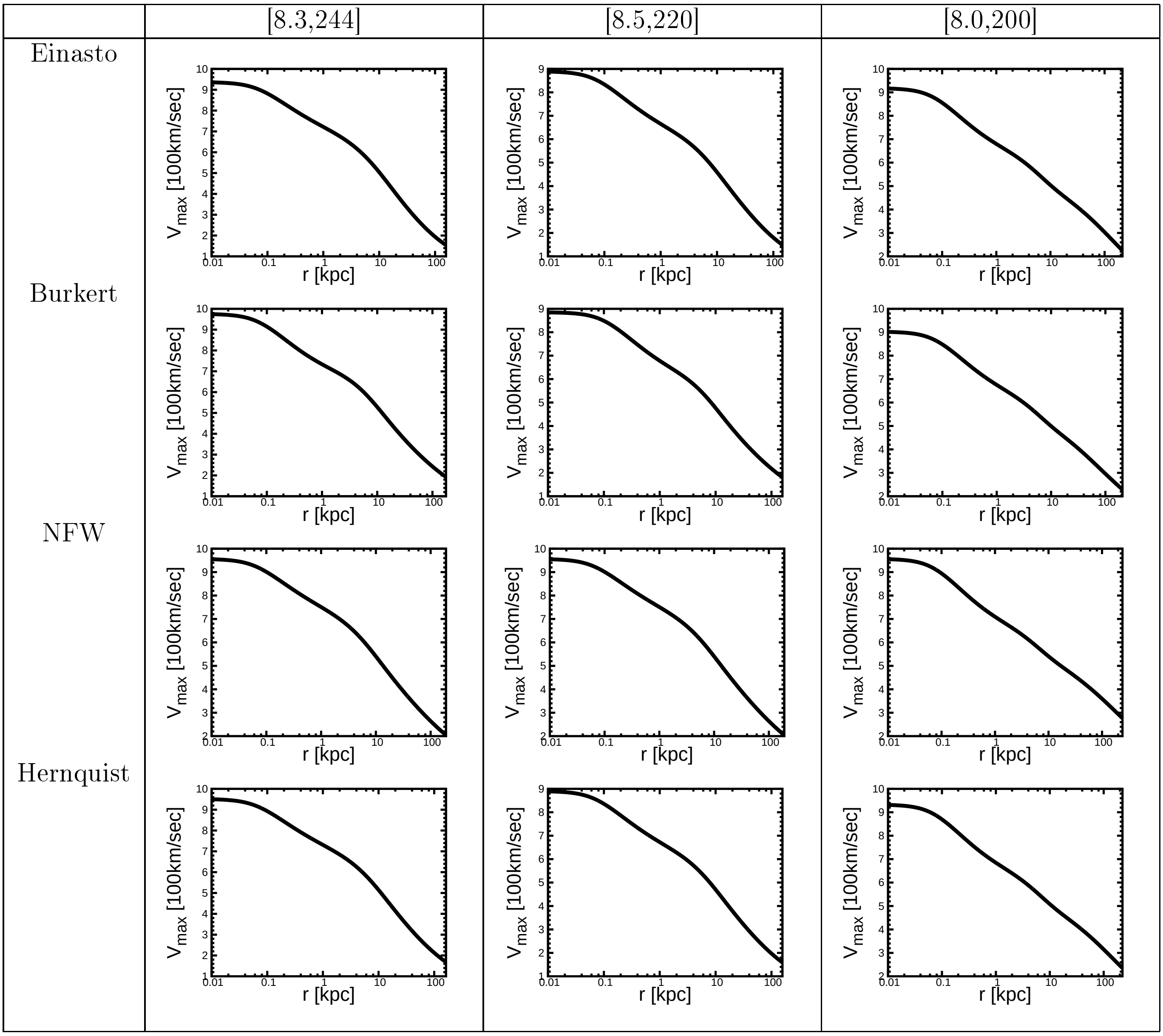


Figure 6.6: Best-fit maximum speed, $v_{max}$, profiles of the Galaxy modeled with four different Galactic dark matter halo models (NFW, Hernquist, Einasto and Burkert) in the presence of visible matter model [see Equations (3.14) and (3.15)], obtained by fit to Galactic rotation curve data [8] for three different sets of values of the Galactic Constants, $\left[\frac{R_0}{\mathrm{kpc}}, \frac{V_0}{\mathrm{km\,s^{-1}}}\right]$ = [8.3, 244], [8.5, 220] and [8.0, 200] as indicated.

# Chapter 7

# Velocity Distribution of Dark Matter Particles in the Galaxy from Rotation Curve Data

## 7.1 Introduction

In the previous chapter, we have derived the local density of dark matter (DM), $\rho_{\rm DM,\odot}$, using the rotation curve (RC) data [8] of our Galaxy. As already mentioned in Chapter 2, in addition to $\rho_{\rm DM,\odot}$, another crucial input for analyzing and interpreting the results of direct detection experiments searching for the Weakly Interacting Massive Particle (WIMP) candidates of DM is the local velocity distribution function (VDF) of the DM particles in the Galaxy.

There is no direct observational data available for the DM velocity distribution till date. However, phenomenological models of VDFs motivated by the results of N-body simulations are available in literature; see for e.g., [166]. There are also propositions in literature on possible forms of the VDFs [40, 41, 42]. Recent simulations (see for e.g., [35]-[39]) indicate a significant departure from typical Maxwellian behavior customarily used in the standard halo model and also anisotropic nature of the VDFs of the DM particles in the halos. Though simulations have become the standard way to investigate the structure, dynamics and evolution of DM halos, they do not yet satisfactorily include the gravitational effects of the visible matter (VM) components of the real Galaxy, which, for our Milky Way, provide the dominant gravitational potential in the inner regions including the Solar neighborhood region.

Given a phase space distribution function (PSDF), the density profile is obtained by integrating over the velocity space of the DM particles [see Equation (3.3)]. It is of interest to ask the question if, given a density profile, Equation (3.3) can be "inverted" to derive the PSDF and consequently a VDF consistent with the given density profile. This problem was studied way back in 1916 by A. S. Eddington [167]. In particular, he showed that an ergodic PSDF, $f(\mathbf{x}(t), \mathbf{v}(t)) = f(E)$ (introduced in Chapter 2) with an isotropic VDF can be obtained by "inverting" a spherically symmetric density profile. This approach has been discussed in [168] (also discussed in detail in Ref. [136]). This formalism was subsequently generalized to construct anisotropic VDFs applicable to spherical systems. Osipkov-Merritt technique (OM) [50, 43] is one such formalism. For systems with anisotropic VDF, the PSDF has the functional dependence as $f(E, L^2)$, where $E$ and $L$ are the specific energy and angular momentum of the system. In the OM formalism, given that the PSDF depends on $E$ and $L$ only through a third variable $Q$ obeying a particular form (see below), the density can be inverted to obtain the PSDF, $f(Q)$. The OM technique has been used earlier to study anisotropic spherical systems in different contexts [169]-[172].

In this chapter, we attempt to construct the anisotropic VDF of the DM particles using the OM formalism starting from a spherically symmetric halo density profile, the parameters of which have been determined by fit to a RC data set of our Galaxy [8], which provides a direct observational probe of the total gravitational potential profile of the Galaxy. It is to note that the VDF of the DM particles at any location in the Galaxy is self-consistently related to the total gravitational potential, i.e., potentials exerted by the DM as well as the underlying VM profile, of the Galaxy. Therefore, it is important to take into account the effect of VM potential while deriving the VDFs of the DM particles.

In the following sections, first we describe the OM formalism in detail. Then, we describe the DM and VM profiles and parameter sets adopted for the analysis. Finally, we present our results and summarize at the end.

## 7.2 Osipkov-Merritt Formalism

For a spherical system of collisionless particles (WIMPs, for example) with anisotropic VDF, the Jeans theorem [43] ensures that the PSDF, $f(\mathbf{x}, \mathbf{v})$, satisfying the collisionless Boltzmann equation depends on the phase space coordinates ($\mathbf{x}$, $\mathbf{v}$) through the total energy per unit mass, $E$, defined before as $E = \frac{1}{2}v^2 + \Phi(r)$ and total angular momentum per unit mass, $L$, where $\vec{L} = \mathbf{x} \times \mathbf{v}$. Here, $v = |\mathbf{v}|$ is the speed, $r = |\mathbf{x}|$ being the radial position of a DM particle and $\Phi(r)$ is the spherically symmetric gravitational potential seen by a test particle at radial distance $r$.

Following the discussions for King model in Chapter 3, we set the relative potential and relative energy as,

$$\Psi(r) \equiv -\Phi(r) + \mathcal{C}, \tag{7.1}$$

$$\mathcal{E} \equiv -E + \mathcal{C} = \Psi(r) - \frac{1}{2}v^2. \tag{7.2}$$

As mentioned earlier, one can invert a chosen spherically symmetric DM density profile, $\rho(r)$, with underlying potential, $\Phi$, to obtain the PSDF, $f(Q)$, by OM technique where $f$ depends on $E$ and $L$ only through the variable $Q$ defined as,

$$Q \equiv \mathcal{E} - \frac{L^2}{2r_a^2}. \tag{7.3}$$

Here, $r_a$ is a constant known as the anisotropy radius of the system within which the velocity space has a nearly isotropic behavior and is still unknown for our Galaxy. The constant $\mathcal{C}$ in Equations (7.1 and 7.2) is chosen such that $f > 0$ for $Q > 0$, and $f = 0$ for $Q \leq 0$. With $r_a \to \infty$, $Q \to \mathcal{E}$ and the system has isotropic VDF every where. One can also express $Q$ in any of the forms given below,

$$Q = \Psi - \frac{1}{2}v^2(1 + \frac{r^2}{r_a^2}\sin^2\eta), \tag{7.4}$$

$$Q = \Psi - \frac{1}{2}\left[v_r^2 + (1 + \frac{r^2}{r_a^2})v_t^2\right], \tag{7.5}$$

where $\eta$ is the polar angle variable, and $v_r$ and $v_t$ are the radial and tangential velocity components, respectively, with $v^2 = v_r^2 + v_t^2$.

The density is related to $f(Q)$ as,

$$\rho(r) = \int f(Q) d^3\mathbf{v}. \tag{7.6}$$

Now, replacing the integration variable $v$ by $Q$ at constant $r$ and $\eta$, we have $dQ = -[1 + \frac{r^2}{r_a^2}\sin^2\eta]\ v\ dv$, and then Equation (7.6) simplifies to

$$\rho(r) \;\; = \;\; 2\pi \int_0^\pi d\eta \sin\eta \int_0^\Psi dQ\ f(Q) \frac{\sqrt{2(\Psi - Q)}}{[1 + (\frac{r}{r_a})^2 \sin^2\eta]^{3/2}}, \tag{7.7}$$

and further performing integration over $\eta$ first, we get,

$$\int_0^\pi \frac{\sin\eta\ d\eta}{[1 + (\frac{r}{r_a})^2 \sin^2\eta]^{3/2}} = \frac{2}{1 + (\frac{r}{r_a})^2}. \tag{7.8}$$

Hence, we can define a new variable $\tilde{\rho}$,

$$\tilde{\rho}(r) \equiv \rho(r)(1 + \frac{r^2}{r_a^2}) = 4\pi \int_0^\Psi dQ f(Q) \sqrt{2(\Psi - Q)}. \tag{7.9}$$

Since $\Psi$ is a monotonic function of $r$ in any spherical system, we can express $\tilde{\rho}$ in terms of $\Psi$ and rewrite Equation (7.9) as

$$\frac{\tilde{\rho}(\Psi)}{\sqrt{8}\pi} = 2 \int_0^\Psi dQ f(Q) \sqrt{(\Psi - Q)}. \tag{7.10}$$

Now, differentiating both sides of the above integral with respect to $\Psi$ we obtain

$$\frac{1}{\sqrt{8}\pi}\frac{d\tilde{\rho}(\Psi)}{d\Psi} = \int_0^{\Psi} dQ \frac{f(Q)}{\sqrt{(\Psi - Q)}}. \tag{7.11}$$

Equation (7.11) is a Abel integral equation which can be solved for $f(Q)$ as [43],

$$f(Q) = \frac{1}{\sqrt{8}\pi^2}\left[\int_0^{Q} \frac{d\Psi}{\sqrt{Q-\Psi}}\frac{d^2\tilde{\rho}}{d\Psi^2} + \frac{1}{\sqrt{Q}}\left(\frac{d\tilde{\rho}}{d\Psi}\right)_{\Psi=0}\right]. \tag{7.12}$$

For a given DM density profile, $\rho(r)$, one can construct $\tilde{\rho}(r)$ from Equation (7.9) and plug in the total potential included in $\Psi(r)$ as seen by a DM particle, and calculate $f(Q)$ using Equation (7.12) for a chosen value of $r_a$. A model for which the PSDF has the form $f(Q)$, where $Q$ is given by Equation (7.3), is called an OM model.

At any location $r$, a DM particle feels not only its own gravitational potential but also the potential of the underlying VM. Therefore the relative potential, $\Psi(r)$, can be written as,

$$\Psi(r) \equiv \Psi_{\rm tot}(r) = \Psi_{\rm DM}(r) + \Psi_{\rm VM}(r). \tag{7.13}$$

To calculate $\Psi(r)$, the spherical $\Phi_{\rm DM}$ is obtained by using $\rho_{\rm DM}$ by solving Poisson's equation [Equation (3.12)] with the boundary conditions given as in Equation (3.13). In this context it must be mentioned that $\Phi_{\rm VM}$ (obtained from $\rho_{\rm VM}$ by solving Poisson's equation) is axisymmetric due to influence of the axisymmetric nature of the VM disk. The OM formalism as described above is valid for spherical systems, therefore, we use the spherical approximation [172, 173] to generate the spherically symmetric VM potential to be used for Equation (7.12) as,

$$\Phi_{\rm VM}(r) \simeq G\int_0^{r} M_{\rm VM}(r')/r'^2 dr', \tag{7.14}$$

where $M_{\rm VM}(r)$ is the total VM mass contained within $r$.

Once $f(Q)$ is calculated from Equation (7.12), at any location '$r$', the normalized radial VDF, $f_r^{\rm rad}(v_r)$, tangential VDF, $f_r^{\rm tan}(v_t)$, and speed distribution, $f_r(v)$, can be written as

$$f_r^{\rm rad}(v_r) = \frac{2\pi}{\rho(r)} \int_0^{\sqrt{\frac{2\Psi - v_r^2}{\gamma^2}}} dv_t \; v_t \; f(Q), \tag{7.15}$$

where $-v_{r,\rm max} \leq v_r \leq v_{r,\rm max}$ with $v_{r,\rm max} = \sqrt{2\Psi}(r)$,

$$f_r^{\rm tan}(v_t) = \frac{2\pi}{\rho(r)} \int_{-\sqrt{2\Psi - \gamma^2 v_t^2}}^{\sqrt{2\Psi - \gamma^2 v_t^2}} dv_r \; v_t \; f(Q), \tag{7.16}$$

where $0 \leq v_t \leq v_{t,\rm max}$ with $v_{t,\rm max} = \sqrt{\frac{2\Psi}{\gamma^2}}(r)$, with $\gamma^2 = (1 + \frac{r^2}{r_a^2})$, and

$$f_r(v) = \frac{2\pi}{\rho(r)} \int_{-\eta_{\rm lim}}^{-\eta_{\rm lim}} d\eta \sin\eta \; v^2 f(Q), \tag{7.17}$$

where $\eta_{\rm lim} = \sqrt{\frac{r_a^2}{r^2 v^2}[\frac{v^2 r^2}{\gamma^2 r_a^2} - 2(\Psi - Q)]}$ and $0 \leq v \leq v_{\rm max}$ with $v_{\rm max} = \sqrt{2\Psi}(r)$.

All the distributions are normalized to unity at any $r$:

$$\int_{-v_{r,\rm max}}^{v_{r,\rm max}} f_r^{\rm rad}(v_r) dv_r = 1 \tag{7.18}$$

$$\int_0^{v_{t,\rm max}} f_r^{\rm tan}(v_t) dv_t = 1 \tag{7.19}$$

$$\int_0^{v_{\rm max}} f_r(v) dv = 1. \tag{7.20}$$

Using Equations (7.15), (7.16), (7.17) one can consequently calculate the velocity moments of the distribution. The anisotropy parameter, denoted by $\beta$, is defined as

$$\beta(r) = 1 - \frac{\sigma_t^2(r)}{2\sigma_r^2(r)}, \tag{7.21}$$

where $\sigma_t$ and $\sigma_r$ are the velocity dispersions in tangential and radial directions, respectively, and are given by,

$$\sigma_r^2(r) = \int_{-v_{r,\mathrm{max}}}^{v_{r,\mathrm{max}}} v_r^2 f_r^{\mathrm{rad}}(v_r) dv_r, \tag{7.22}$$

$$\sigma_t^2(r) = \int_0^{v_{t,\mathrm{max}}} v_t^2 f_r^{\mathrm{tan}}(v_t) dv_t, \tag{7.23}$$

and

$$< v^2 >= \sigma_r^2 + \sigma_t^2 = \int_0^{v_{\mathrm{max}}} v^2 f_r(v) dv. \tag{7.24}$$

For the OM technique, $\beta$ follows a specific form of the radial variation parametrized by $r_a$ and is given by [43],

$$\beta(r) = \frac{r^2}{r^2 + r_a^2}. \tag{7.25}$$

This function rises from zero (true for isotropic VDFs) at $r \ll r_a$ to unity at $r \gg r_a$ (radially biased VDF), and already exceeds 0.9 for $r > 3r_a$. This form which holds good irrespective of the DM halo and underlying VM model used, also serves as a consistency check of our numerical calculations,

## 7.3 The Dark and Visible Matter Model

In order to derive the VDF for the DM particles constituting the Galactic halo, we adopt the simulation motivated Einasto profile [159]-[161] given in Equation (6.3) and a VM density distribution given in Equations (3.14) and (3.15). The parameters of both the DM and VM profiles have been determined by fit to the RC data for our Galaxy [8] using Markov Chain Monte Carlo analysis as done in the previous chapter. In particular, we adopt the best fit parameters obtained from fit to RC data for the Galactic Constants (GCs) set $\left[\frac{R_0}{\mathrm{kpc}}, \frac{V_0}{\mathrm{km\,s^{-1}}}\right] = [8.3,\, 244]$ compatible with recent measurements Oort's constants (see Chapter 5 for details). The resultant best-fit values of the parameters are listed below in Table 7.1. Since both VM and DM profiles considered have no physical truncation, we can set,

$$C \equiv \Phi(\infty), \tag{7.26}$$

in Equation (7.2) and construct relative potentials as,

$$\Psi_{\mathrm{VM\ or\ DM}}(r) \equiv \Phi_{\mathrm{VM\ or\ DM}}(\infty) - \Phi_{\mathrm{VM\ or\ DM}}(r). \tag{7.27}$$

| Parameter | Units | Most-likely |
|---|---|---|
| | Visible Matter | |
| $\rho_{b0}$ | $10^2\,M_\odot\,\mathrm{pc}^{-3}$ | 11.01 |
| $r_b$ | kpc | 0.06 |
| $\Sigma_\odot$ | $M_\odot\,\mathrm{pc}^{-2}$ | 56.82 |
| $R_d$ | kpc | 4.02 |
| $z_h$ | kpc | 0.3 |
| | Dark Matter | |
| $\rho_{\mathrm{DM},\odot}$ | $\mathrm{GeV\,cm}^{-3}$ | 0.56 |
| $r_s$ | kpc | 5.74 |
| $s_n$ | – | 3.09 |

Table 7.1: Best fit parameters values of visible matter model [see Equations (3.14) (3.15)] and Einasto type dark matter halo model obtained by fit to a Galactic rotation curve data [8] for Galactic Constants $\left[\frac{R_0}{\mathrm{kpc}}, \frac{V_0}{\mathrm{km\,s}^{-1}}\right] = [8.3,\, 244]$.

## 7.4 Results and Discussions

We now numerically invert the Einasto density profile to solve for the most likely PSDF, $f(Q)$, using Equation (7.12) by including the gravitational influence of the VM model on the DM particles in a self-consistent manner. The parameters of the Einasto DM halo and VM parameters have been adopted as the best fit values as obtained by fit to the Galactic RC data [8] for GCs set $\left[\frac{R_0}{\mathrm{kpc}}, \frac{V_0}{\mathrm{km\,s}^{-1}}\right] = [8.3,\, 244]$ by assuming a particular form of VM distribution [see Equations (3.14) and (3.15)]. We thereafter derive the VDF profiles at different locations for different values of the anisotropy radius, $r_a$.

The PSDF i.e., $f(Q)$ profile for the Einasto halo, as obtained by OM formalism, is found to be non-negative every where for $r_a \geq 4$ kpc. Hence, we can conclude that the Galactic halo can take any value of anisotropy radius greater than or equal to 4 kpc.

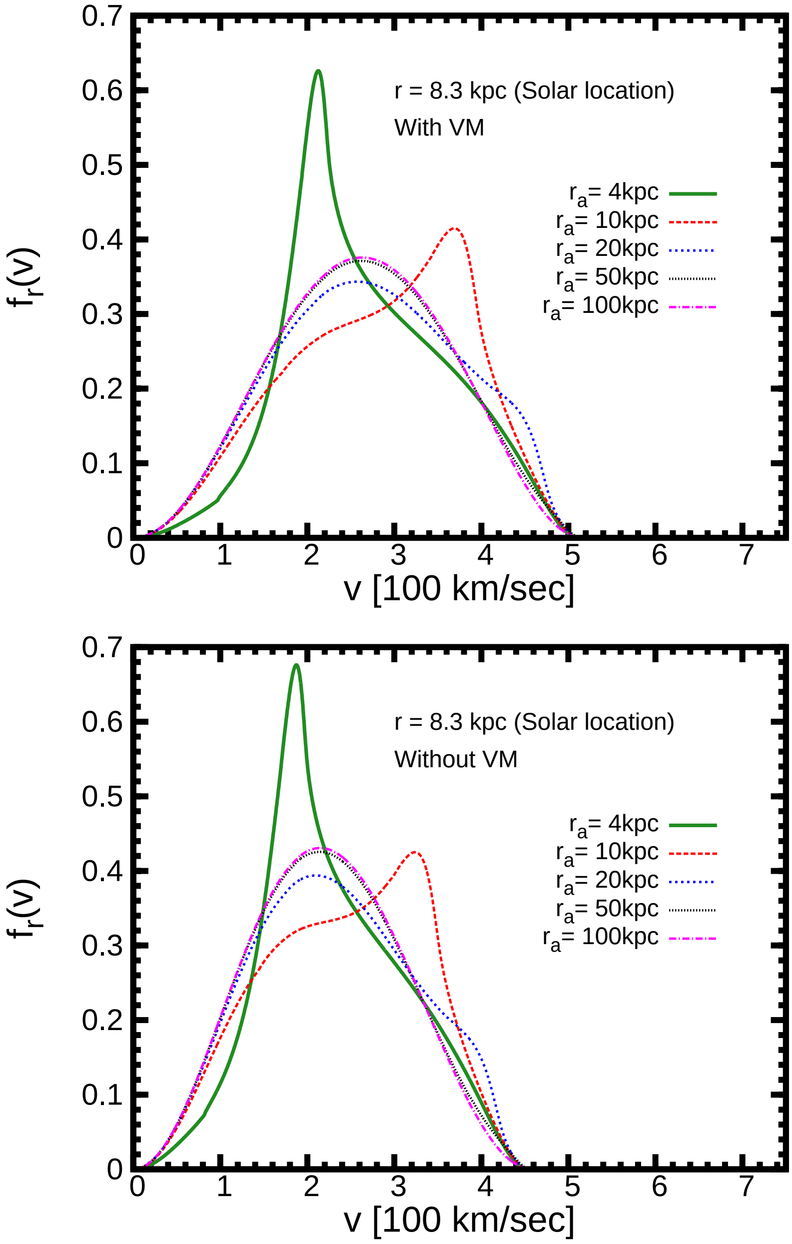


Figure 7.1: Top : The speed distribution ($f_r(v)$) of the dark matter particles constituting an Einasto type Galactic halo at Solar location (r = 8.3 kpc) for various values of anisotropy radius ($r_a$), 'with VM'. Bottom : Same for 'without VM'.

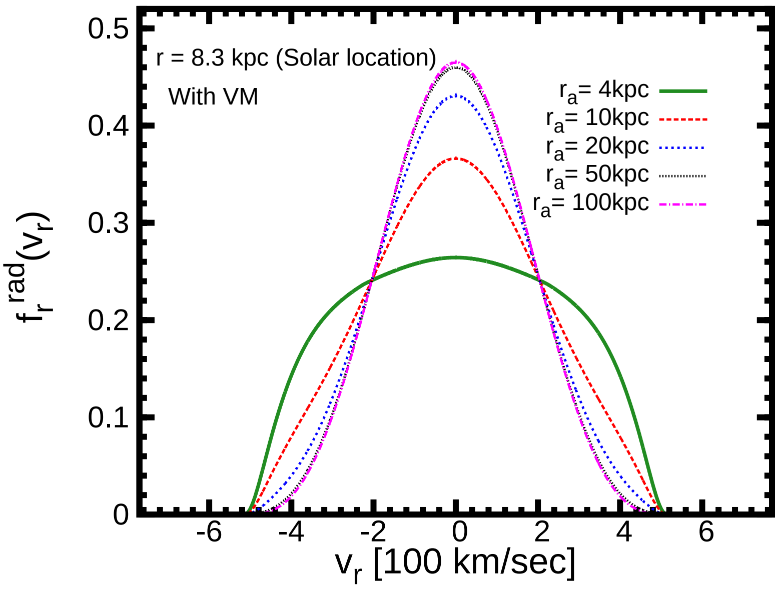


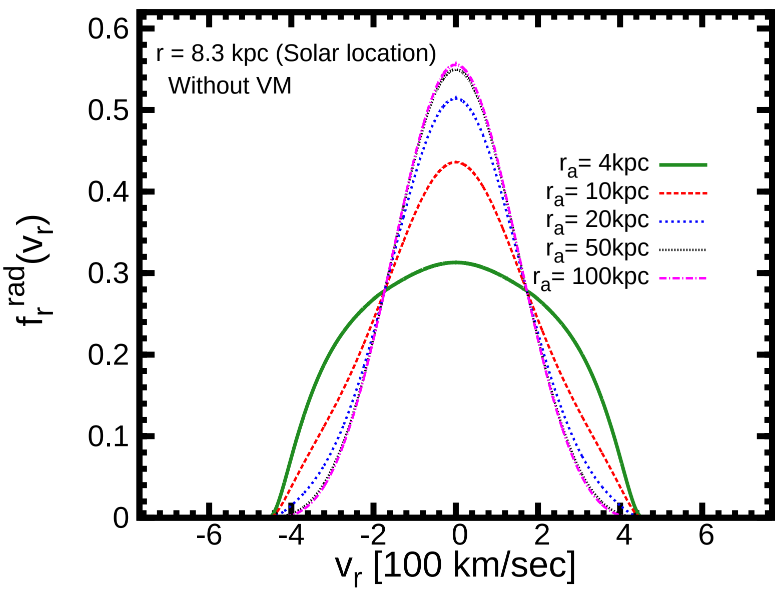


Figure 7.2: Top : The radial velocity distribution ($f_r^{\rm rad}(v_r)$) of the dark matter particles constituting an Einasto type Galactic halo at Solar location (r = 8.3 kpc) for various values of anisotropy radius ($r_a$), 'with VM'. Bottom : Same for 'without VM'.

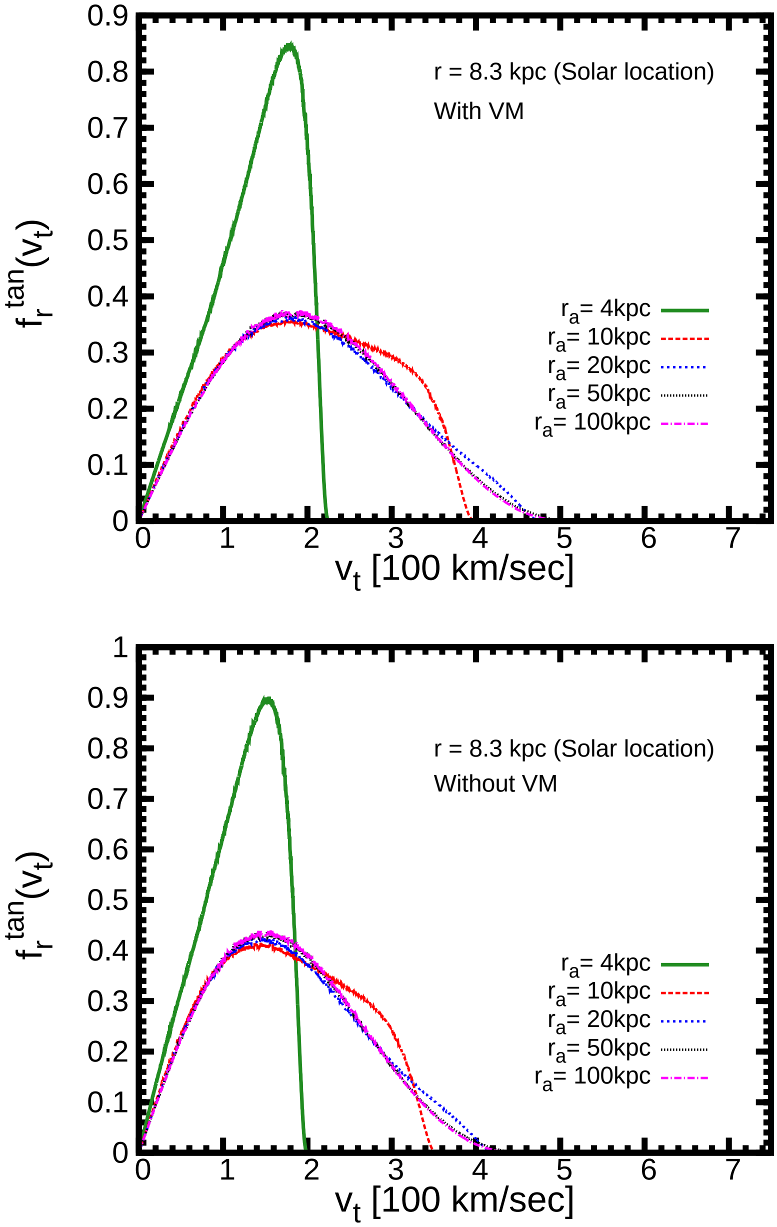


Figure 7.3: Top: The tangential velocity distribution ($f_r^{\tan}(v_t)$) of the dark matter particles constituting an Einasto type Galactic halo at Solar location (r = 8.3 kpc) for various values of anisotropy radius ($r_a$), 'with VM'. Bottom : Same for 'without VM'.

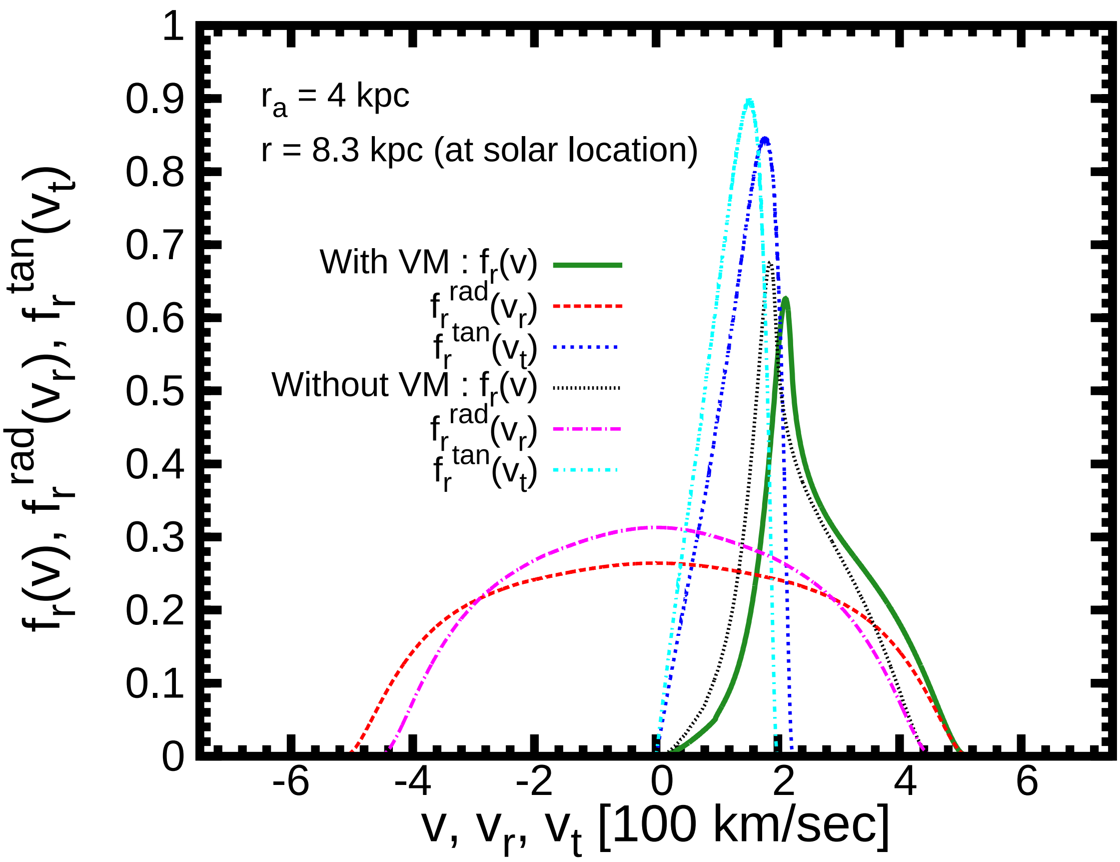


Figure 7.4: Local [total: $f_r(v)$, radial: $f_r^{\rm rad}(v_r)$ and tangential $f_r^{\rm tan}(v_t)$] anisotropic velocity distributions of dark matter particles constituting a Einasto type Galactic halo at Solar location (r = 8.3 kpc) 'with' and 'without' VM for anisotropy radius, $r_a$= 4 kpc.

The local VDFs of the DM particles constituting an Einasto type Galactic halo 'with' and 'without' VM for various $r_a$ are presented in Figures 7.1, 7.2, 7.3 and 7.4 calculated using Equations (7.15), (7.16) and (7.17), respectively, for $r \equiv R_0 = 8.3\,\mathrm{kpc}$. The VDFs are seen to be of non-Maxwellian form and anisotropic in nature and the coupling to VM clearly broadens the distribution by supporting higher velocity dispersion. The phrase 'with VM' refers to the usual 'coupled case' where $\Psi \equiv \Psi_{\rm DM} + \Psi_{\rm VM}$ in Equation (7.12), and 'without VM' refers to the isolated halo or 'uncoupled case' with $\Psi \equiv \Psi_{\rm DM}$ in Equation (7.12). In all cases, the Einasto halo and VM parameters have been obtained by fitting to the rotation curve data [8] for GCs set $\left[\frac{R_0}{\rm kpc}, \frac{V_0}{\rm km\,s^{-1}}\right] = [8.3, 244]$ by assuming a form of the VM distribution given by Equations (3.14) and (3.15).

Figures 7.5, 7.6 and 7.7 show the normalized speed, radial and tangential velocity distributions calculated using Equations (7.15), (7.16) and (7.17), respectively, of the dark matter particles constituting an Einasto type Galactic halo at various galactocentric radii for a chosen anisotropy radius, $r_a = 4$ kpc 'with' and 'without' VM. It is clearly evident that VDFs of this system is not only non-Maxwellian but also shows anisotropic behavior every where throughout the halo and the effect of VM decreases with higher radii, as expected.

Figure 7.8 shows the radial variation of radial and tangential components of velocity dispersions and the total velocity dispersion of the DM particles constituting an Einasto type halo density profile. These has been self-consistently calculated using Equations (7.22), (7.23) and (7.24), respectively, for different possible values of the anisotropy radius, $r_a \geq 4$ kpc. It is evident that 'coupling' to VM significantly affects the velocity dispersion profiles of the DM particles. In fact, as the DM particles move under the total gravitational potential of DM +

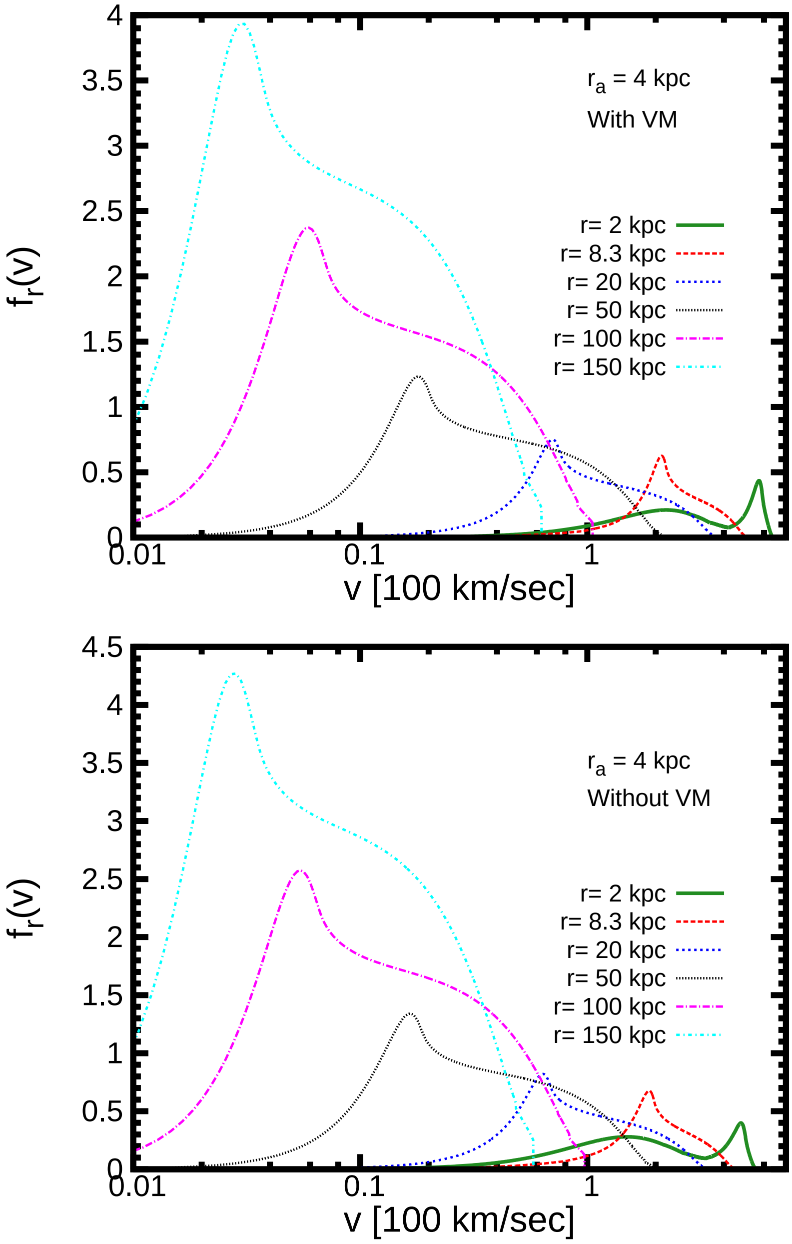


Figure 7.5: Normalized speed distribution ($f_r(v)$) of the dark matter particles constituting an Einasto type Galactic halo at various galactocentric radii for anisotropy radius, $r_a$= 4 kpc, 'with' (Top) and 'without' (Bottom) VM.

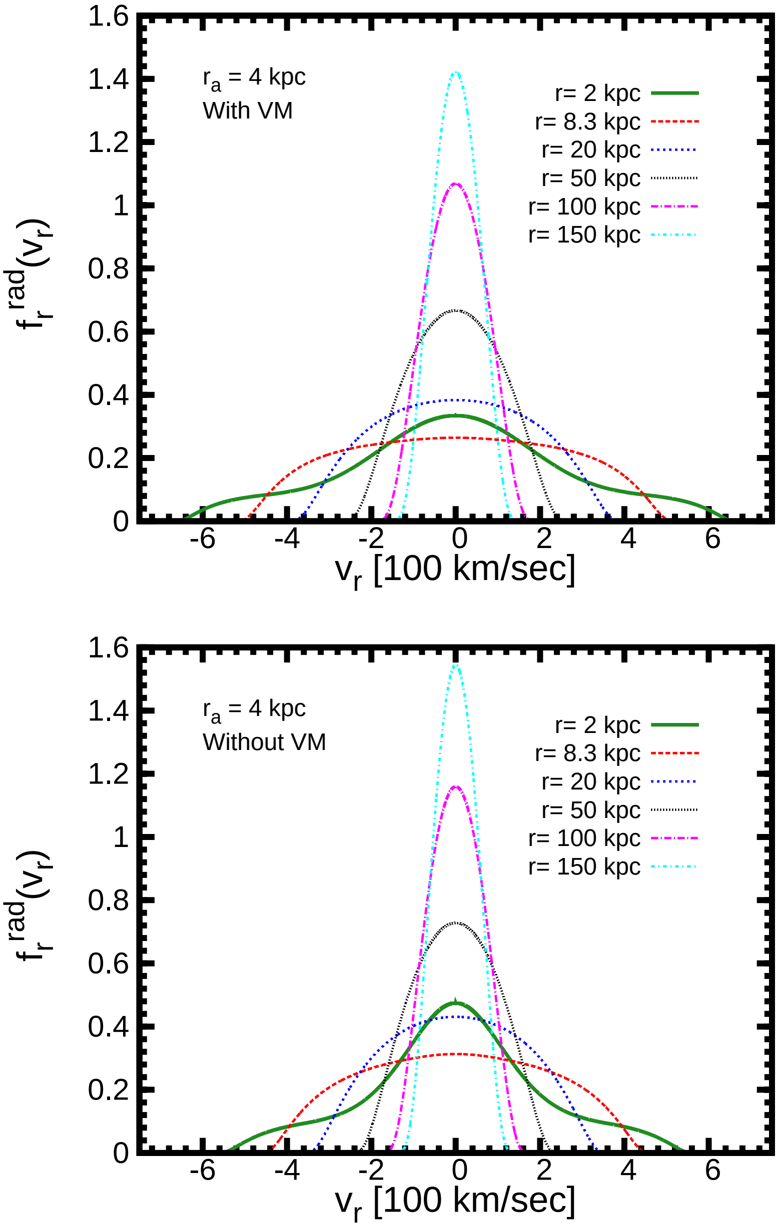


Figure 7.6: Normalized radial velocity distribution ($f_r^{\mathrm{rad}}(v_r)$) of the dark matter particles constituting an Einasto type Galactic halo at various galactocentric radii for anisotropy radius, $r_a$= 4 kpc, 'with' (Top) and 'without' (Bottom) VM.

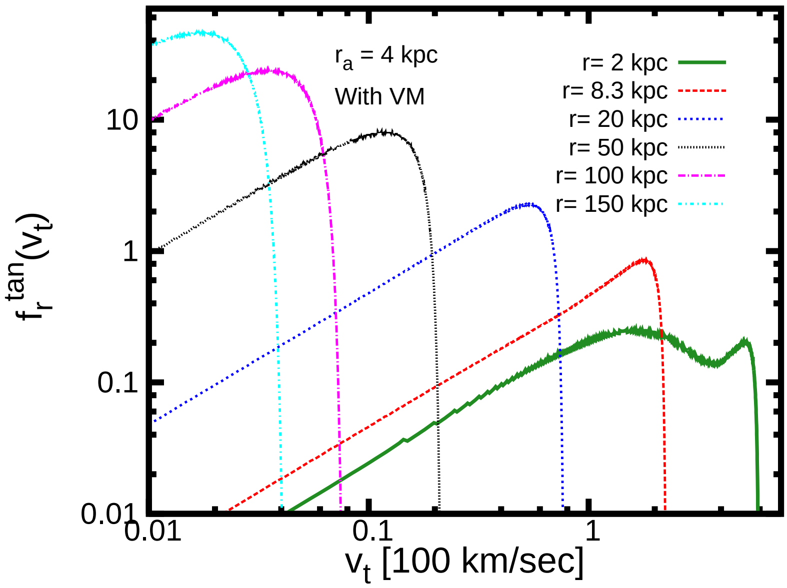


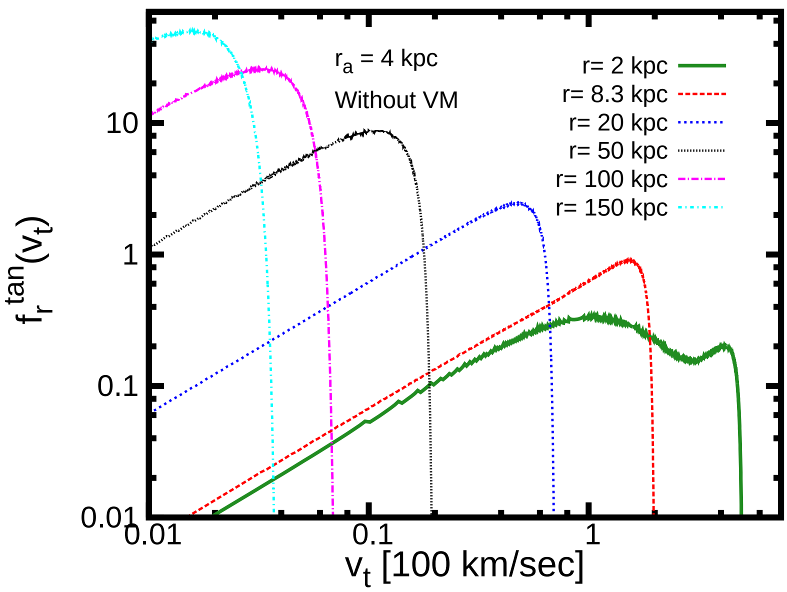


Figure 7.7: Normalized tangential velocity distribution ($f_r^{\tan}(v_t)$) of the dark matter particles constituting an Einasto type Galactic halo at various galactocentric radii for anisotropy radius, $r_a$= 4 kpc, 'with' (Top) and 'without' (Bottom) VM.

VM, the additional VM potential is capable of supporting higher velocity dispersion values and also introduces an additional broad peak at some inner radii. It is interesting to note that for both with and without VM case, the velocity dispersion profiles exhibit non-monotonic behavior with radius.

Figure 7.9 shows the radial profile of the anisotropy parameter, $\beta(r)$, associated with an OM model. It is to note that the $\beta(r)$ is only determined by the $r_a$ value and is insensitive to the particular DM and VM model details. The limit on $r_a$ puts a upper bound on $\beta_\odot \equiv \beta(r = R_0)$ from Equation (7.25) as $\beta_\odot \leq 0.81$.

Finally in Table 7.2, the values of some of the relevant physical quantities of interest characterizing the Galaxy, derived from the most likely VM and (Einasto type) DM parameters listed in Table 7.1, are presented. The best fit total mass has been found to be $\sim 4.5 \times 10^{11}\, M_\odot$ for a virial radius of 157 kpc, roughly 2 times larger than that obtained for the King model earlier in Chapter: 4. Also, the best fit values of the local circular velocity ($\sim 267$ $\mathrm{km\,s^{-1}}$), local escape speed ($\sim$ 532 $\mathrm{km\,s^{-1}}$) and local velocity dispersion ($\sim 283$ $\mathrm{km\,s^{-1}}$) are found to take higher values than those in King model where the values were $\sim$ 232, 396, 252 $\mathrm{km\,s^{-1}}$, respectively.

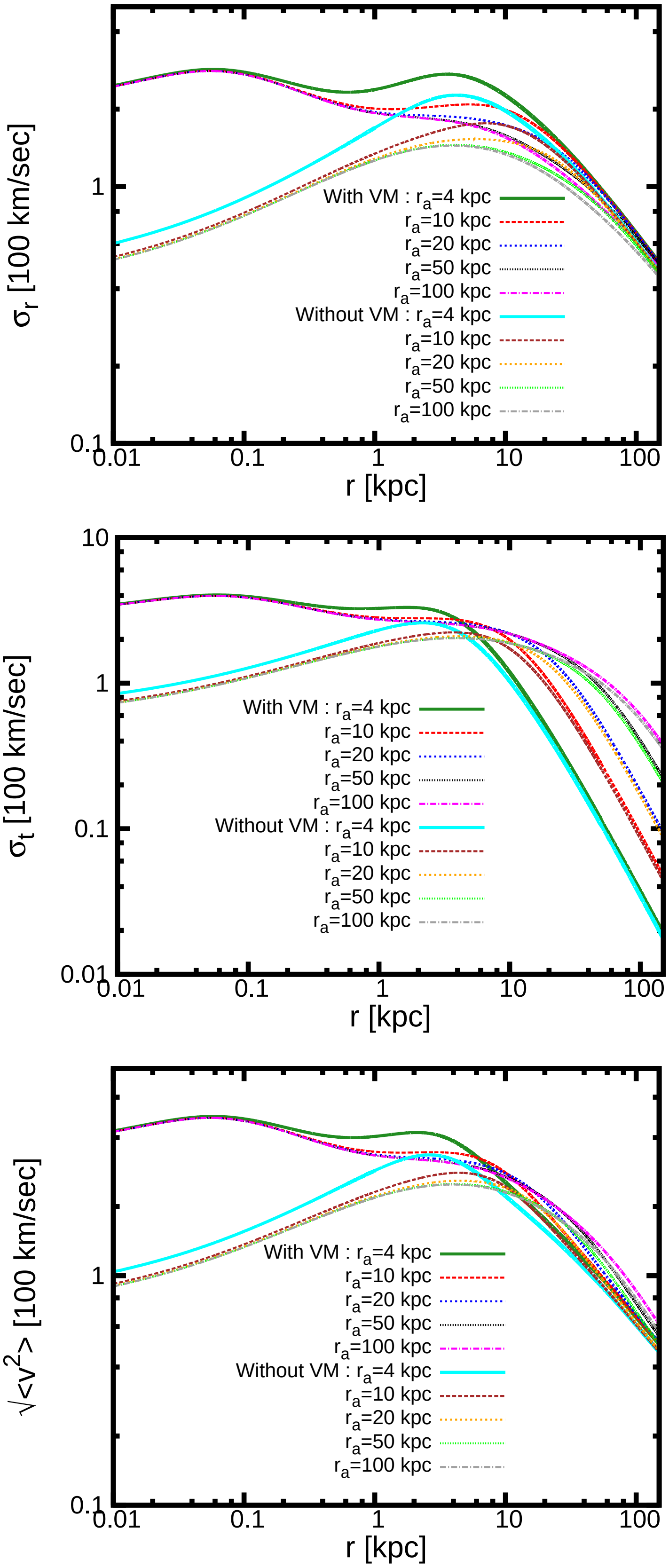


Figure 7.8: Radial ($\sigma_r$), tangential ($\sigma_t$) and total ($\langle v^2 \rangle^{1/2}$) (top, middle, bottom) velocity dispersion profiles of dark matter particles constituting a Einasto type halo with galactocentric distance up to virial radius shown for 'with VM' and 'without VM' cases, for different anisotropy radius ($r_a$) values.

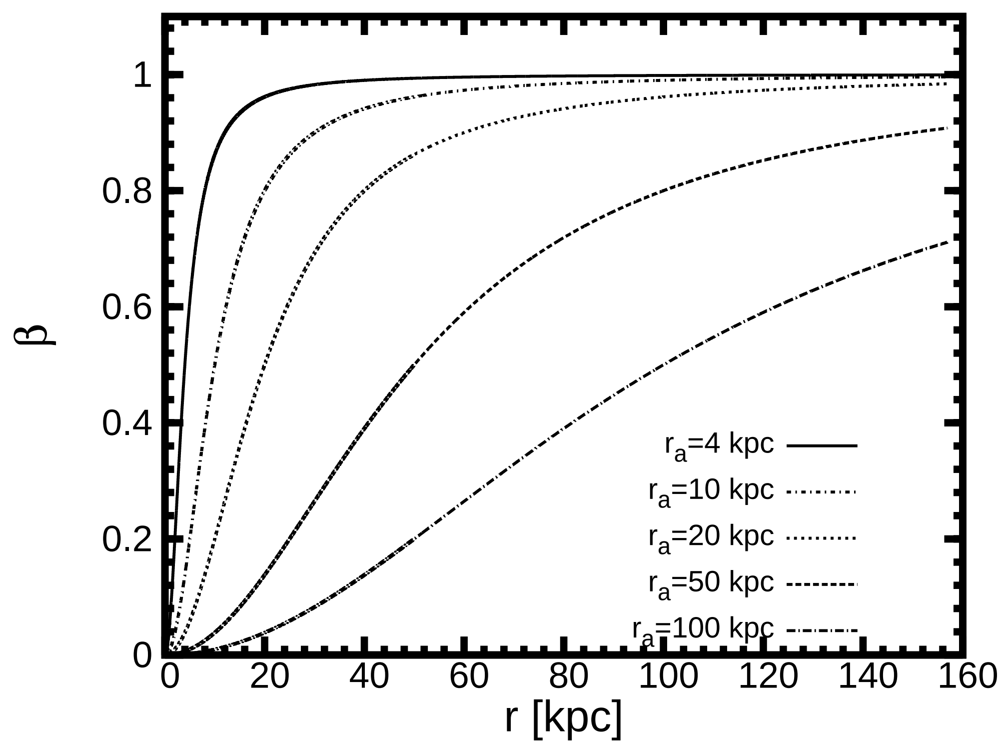


Figure 7.9: The radial profile of the anisotropy parameter, $\beta$, profile for the dark matter particles constituting an Einasto type Galactic halo for various values of the anisotropy radius, $r_a \geq 4\,\mathrm{kpc}$ the context of Osipkov-Merritt formalism.

## 7.5 Summary

In this chapter, we have studied the VDF of the WIMPs hypothesized to constitute the dark matter halo in our Galaxy considering the N-body simulation motivated Einasto density profile as the halo density model. The best fit Einasto type DM and VM [see Equations (3.14) and (3.15)] parameters have been obtained by fitting to a RC data set extending up to $\sim 200$ kpc for the GCs set, $\left[\frac{R_0}{\mathrm{kpc}}, \frac{V_0}{\mathrm{km\,s^{-1}}}\right] = [8.3,\, 244]$ [8]. The best fit $\rho_{\mathrm{DM},\odot}$ is found to be $\sim 0.56$ $\mathrm{GeV\,cm^{-3}}$ whereas a value of 0.2 $\mathrm{GeV\,cm^{-3}}$ was obtained with the finite sized King model DM halo in Chapter 4 with RC extending to $\sim 60$ kpc for GCs set $\left[\frac{R_0}{\mathrm{kpc}}, \frac{V_0}{\mathrm{km\,s^{-1}}}\right] = [8.5,\, 220]$ with pre-fixed VM parameters. The OM technique has been employed to

| Derived Quantities | Unit | Einasto |
|---|---|---|
| Bulge mass ($M_b$) | $10^{10}\,M_\odot$ | 2.2 |
| Disk mass ($M_d$) | $10^{10}\,M_\odot$ | 4.7 |
| Total VM mass ($M_{\rm VM} = M_b + M_d$) | $10^{10}\,M_\odot$ | 6.9 |
| DM Halo virial radius ($r_{vir}$) | kpc | 157 |
| Concentration parameter ($\frac{r_{vir}}{r_s}$) | – | 27.3 |
| DM halo virial mass ($M_{\rm DM}$) | $10^{11}\,M_\odot$ | 3.8 |
| Total virial mass of Galaxy ($M_{\rm tot} = M_{\rm VM} + M_{\rm DM}$) | $10^{11}\,M_\odot$ | 4.5 |
| VM mass within $R_0$ | $10^{10}\,M_\odot$ | 4.1 |
| DM mass within $R_0$ | $10^{10}\,M_\odot$ | 9.1 |
| Total mass within $R_0$ | $10^{11}\,M_\odot$ | 1.3 |
| DM surface density, $\Sigma_{\rm DM}$ at $R_0$ ($\lvert z\rvert \leq 1.1\,$kpc) | $M_\odot\,{\rm pc}^{-2}$ | 35.2 |
| Total Mass within 50 kpc | $10^{11}\,M_\odot$ | 3.9 |
| Total Mass within 60 kpc | $10^{11}\,M_\odot$ | 4.1 |
| Total Mass within 100 kpc | $10^{11}\,M_\odot$ | 4.4 |
| Local circular velocity ($V_{c,\odot}$) | ${\rm km\,s^{-1}}$ | 267 |
| Local maximum velocity ($v_{max,\odot}$) | ${\rm km\,s^{-1}}$ | 532 |
| Local total dispersion* ($\langle v^2\rangle_\odot^{1/2}$) | ${\rm km\,s^{-1}}$ | 282.7 |
| Local radial dispersion* (${\sigma^2_{r,\odot}}^{1/2}$) | ${\rm km\,s^{-1}}$ | 240.0 |
| Local tangential dispersion* (${\sigma^2_{t,\odot}}^{1/2}$) | ${\rm km\,s^{-1}}$ | 147.4 |
| Local anisotropy* ($\beta_\odot$) | – | 0.81 |

Table 7.2: The most-likely values of various relevant physical parameters of the Milky Way calculated with visible matter [see Equations (3.14) and (3.15)] and dark matter constituting an Einasto type Galactic halo with the most-likely values of the parameters listed in Table 7.1 obtained by fit to a Galactic rotation curve data [8] for Galactic Constants $\left[\frac{R_0}{\rm kpc}, \frac{V_0}{\rm km\,s^{-1}}\right] = [8.3,\ 244]$. The quantities marked with a * have been calculated for the lowest allowed value of the anisotropy radius, $r_a = 4\,$kpc.

"invert" the Einasto density profile to derive a self-consistent PSDF considering the gravitational influence of the underlying VM. The PSDF, describing the WIMPs, is found to be non-negative for $r_a \geq 4$ kpc which sets an upper bound $\beta_\odot \leq 0.81$.

The VDFs so obtained indicates that the velocity space throughout the halo is anisotropic in nature and exhibits significant departure from typical Maxwellian form. It is observed that coupling to VM introduces an additional broad peak within the Solar circle and supports higher values of velocity dispersions. The gravitational influence (through gravitational potential) of VM also leads to rise in values of maximum velocities [see Equations (7.15), (7.16) and (7.17)] since it is $\propto \sqrt{\Psi_{\rm tot}(r)}$, where $\Psi_{\rm tot}(r)$ is the total (DM+VM) relative gravitational potential of the Galaxy. However, the VM effect decreases with higher radii as expected.

The relevant physical parameters like total mass ($\sim 4.5 \times 10^{11}\, M_{\odot}$ for a virial radius of 157 kpc), local escape speed ($\sim 532$ $\mathrm{km\,s^{-1}}$), local circular velocity ($\sim 267$ $\mathrm{km\,s^{-1}}$) and local velocity dispersion ($\sim 283$ $\mathrm{km\,s^{-1}}$) are found to take higher values than the analysis done earlier in Chapter 4 with King model in the context of an RC for GCs set $\left[\frac{R_0}{\rm kpc}, \frac{V_0}{\rm km\,s^{-1}}\right] = [8.5,\, 220]$.

Due to the restrictive form of $\beta(r)$ the in OM formalism, there have been recent attempts to extend the OM technique to address more general forms of $\beta(r)$; see, e.g., Refs. [174] - [179]. We wish to consider these aspects in a future work.

# Chapter 8

# Summary

---

In this chapter, we summarize the results we have obtained in this thesis.

Detection of dark matter (DM), which constitutes $\sim 26\%$ of the present energy density in our Universe, has been one of the toughest challenges in astroparticle physics for several decades. There has been various lines of evidence for this elusive matter component on scales ranging from dwarf galaxies to the largest scale structures seen in the Universe today. The behavior of the observed rotation curve (RC) of spiral galaxies, like our own Milky Way, provides one of the strongest pieces of evidence in support of the existence of DM on the galactic scale. In particular, the non-declining nature of RC beyond the visible edge of the Galaxy can be naturally explained within the hypothesis that the luminous matter is embedded in a roughly spherical halo of DM, the true extent of which is, however, currently unknown. A range of precise cosmological surveys indicate them to be stable, non-baryonic and essentially dissipationless and collisionless by nature. Currently, one of the most favored candidates of DM belongs to a class of particles called 'Weakly Interacting Massive Particles' or WIMPs, with masses possibly lying within few GeV to several hundreds of TeV. The WIMPs can naturally explain the observed cosmological relic density of DM-a fact known as 'WIMP miracle'. Several experiments worldwide are currently searching for WIMPs via direct detection (DD) experiments (that look for nuclear recoil events arising from WIMPs scattering off nuclei of suitably chosen detector materials) as well as through indirect detection experiments (that look for signals of self-annihilation products of the WIMPs, such as, neutrinos, gamma rays, anti protons, positrons, etc. in high WIMP density regions). In addition there are searches going on in accelerators such as LHC.

For this thesis, we have focused particularly on DD of WIMPs. In order to analyze and interpret the results from DD experiments, one needs two crucial astrophysical inputs, namely, the local (i.e., the Solar neighborhood) density of DM, $\rho_{DM,\odot}$, and the local velocity distribution function (VDF) of the DM particles constituting the Galactic halo, which are currently not known with certainty. Towards this end, in this thesis, we attempted to derive these quantities from direct observational data, pertaining to the Milky Way.

We have explored two approaches to the problem of determining the phase space distribution function (PSDF) of the DM particles (assumed to be WIMPs throughout this thesis) in our Galaxy. In the first approach, we use a suitable ansatz for the form of the PSDF describing the WIMPs that is a stationary solution of the collisionless Boltzmann equation (CBE). Such PSDFs can be expressed, due to Jeans theorem, as function of integral of motions such as the specific energy ($E$), angular momentum ($L$), and so forth. In particular we have studied PSDFs, that depend only on $E$, which implies that the VDFs corresponding to the chosen PSDF is isotropic in nature. Specifically, we have studied the 'isothermal sphere' (IS) model customarily used in the so called 'standard halo' model (SHM) description of the phase space structure of the DM particles populating the Galactic halo. However, the IS (describing the SHM) suffers from some serious limitations in providing a realistic description of Galactic halo., viz., it has a diverging total mass and the VDF of this system is Maxwellian by nature where the maximum attainable velocity of a particle can be as large as $\infty$, which is unexpected of the WIMPs populating a finite sized galactic halo, like Milky Way, in order for it to remain bound to the system. We have, therefore, considered the 'King' or 'lowered isothermal' model describing a finite size PSDF of the Galactic halo. In both cases (IS and King), the parameters of the models have been determined by fitting the observed RC data of our Galaxy. In doing this, we have included the effect of gravitational influence of the observed visible matter (VM) on the PSDF describing the DM halo in a self consistent manner since it's the VM that dominates the gravitational potential in the inner regions of the Galaxy. Further, we have studied the implications of this model, for the various DD experiments.

In the second approach, we have used the Osipkov-Merritt (OM) formalism to obtain the PSDF of the DM halo of our Galaxy by "inverting" a given spherically symmetric density profile of the DM halo. Such a PSDF satisfies the stationary CBE and depends on both $E$ and $L$, which implies that the VDFs corresponding to the chosen PSDF is anisotropic in nature. We have chosen the 'Einasto' density profile, which provides a good description of the DM halo profile obtained in numerical N-body simulations. The parameters of this profile have been determined by fit to the RC data of our Galaxy. As in the first approach, we have again included the effect of the gravitational influence of VM on DM in a self consistent manner.

We have shown that, the inclusion of VM effect significantly changes the nature of the PSDFs both in the case of IS and King models, which significantly influence the results of the analysis of the DD experiments. In particular, in **Chapter** 3, we have found that, by considering the effect of the gravitational influence of the VM, the IS halo requires values of DM velocity dispersion, $\langle v^2 \rangle^{1/2}$, considerably higher than 270 $\mathrm{km\,s^{-1}}$, a $\langle v^2 \rangle^{1/2}$ value customarily adopted in the SHM model along with $\rho_{\mathrm{DM},\odot} \simeq 0.3$ $\mathrm{GeV\,cm^{-3}}$, to fit the RC data. This is because the added VM potential is now able to support higher DM $\langle v^2 \rangle^{1/2}$ values in order to tolerate a $\rho_{\mathrm{DM},\odot} \simeq 0.3$ $\mathrm{GeV\,cm^{-3}}$ compared to the 'isolated' SHM model. The compatibility region in the WIMP mass versus WIMP nucleon spin-independent cross-section parameter space (where the annual modulation seen by DAMA experiment is compatible with the null results of other experiments) shrinks with increasing values of $\langle v^2 \rangle^{1/2}$. In addition, we have found that there is significant change in the compatibility region with varied values of the WIMP-nucleus scattering inelasticity parameter, $\delta$.

The King model, studied in **Chapter** 4, represents a spherically symmetric cored finite size DM halo of the Galaxy. The gravitational influence of VM has a significant effect in "pulling in" more DM towards the center of the Galaxy leading to a shrinking of the core radius by enhancing the central DM density and introducing a flattening of DM density on the disk by 30-40% with respect to vertical density of the DM halo profile. The VDF is non-Maxwellian in nature with a sharp cut off at a finite maximum speed self-consistently determined by the model itself. This form of VDF has significant effect on the best fit DAMA compatible regions, particularly for low mass (for WIMP mass $\ll$ mass of target nuclei) regions compared to results in the context of SHM, which has a a typical Maxwellian VDF. In the low WIMP mass regions the velocity integral part (low WIMP mass implies a higher value of the lower limit of this integration) in the calculation of direct detection event rates [see Equation (2.4)] contributes differently for different VDFs and WIMP masses, whereas, a simple approximation of the upper limits on cross-section $\sim \rho_{\rm DM,\odot}^{-1}$ holds otherwise. This also indicates the importance of adopting a physically acceptable halo model to explore low mass WIMP regions.

Throughout this thesis, RC has been the main observational anchor in our approach to the problem of deriving information on the PSDF of the DM particles hypothesized to constitute the halo of our Galaxy. In **Chapter** 5, we have attempted the construction of the RC data of our Galaxy without referring to any specific model of the VM or DM halo of the Galaxy. We have particularly concentrated in the disk region and considered kinematical data on a variety of disk tracer objects to compile the RC data. We have also investigated the sensitivity of the disk RC data with the assumed set of Galactic Constants (GCs) values and found that, at any given R, the circular velocity is higher for higher value of $V_0$, the circular velocity of the local standard of rest frame around the Galactic center. The RC set so obtained is found to have dips around 3 and 9 kpc consistent with earlier works in literature. In addition, our results are seen to have significantly smaller error bars, which we attribute to the better statistical estimates obtained in our analysis due to consideration of a larger variety of tracer samples.

In **Chapter** 6, we have presented a comprehensive study of the derivation of the $\rho_{\rm DM,\odot}$, using RC data of our Galaxy extending up to $\sim 200$ kpc for various GCs sets, by adopting four different profiles for the Galactic DM halo model. The parameters of the models have been determined by fit to the RC data by a Markov Chain Monte Carlo analysis. We have found that the best fit $\rho_{\rm DM,\odot}$ is fairly independent of the DM halo density profile (be it cored or cuspy) and rather shows a monotonic behavior with the value of $V_0$ value of the GCs set chosen. Specifically it varies by a factor of $\sim 3$ (from $\sim 0.2$ to $\sim 0.6$ GeV cm$^{-3}$ for $V_0$ changing from 200 to 244 km/sec) within the chosen $V_0$ range. The global properties like halo virial radius, total virial mass etc. which are dependent on the large distance behavior of RC data, are seen to be uncorrelated to the $V_0$ values since it has been observed that RC profile beyond the disk region is insensitive to the GCs set adopted.

Following the second approach to determining the PSDF of the DM halo of the Galaxy in **Chapter** 7, we derived the PSDF of the WIMPs populating the DM halo by "inverting" the Einasto density profile using OM technique. The self consistent PSDF so obtained is characterized by an anisotropic velocity space and parametrized by an anisotropy radius, $r_a$, within which the VDF has a nearly isotropic behavior. We have found that the $r_a$ has a lower bound based on the condition of non-negativity of the PSDF every where, which in turn places a upper bound on anisotropy parameter values at all positions throughout the halo. The effect of gravitational influence of VM is significant up to $\sim$ Solar radius and found to support higher radial and tangential values and introduce an additional broad peak in the inner Solar circle region for the velocity dispersions. However, the VM effect decreases with higher radii, as expected.

Our findings, presented in this thesis, have significant implications for the analysis and interpretation of the results of DD experiments, which we propose to study in more detail in future work.

# Bibliography


[1] P. A. R. Ade, et al. [Planck Collaboration], Astron. Astrophys. **571** (2014) A16

[2] H. Hoekstra, H. Yee, & M. Gladders, New Astron. Rev. **46** (2002) 767;
L. A. Moustakas et al., Science white paper submitted to the *Astro2010 Decadal Cosmology & Fundamental Physics Science* Frontier Panel, **arXiv**: 0902.3219;
L. V. Koopmans & T. Treu, ApJ **583** (2003) 606

[3] M. Mateo, Ann. Rev. Astron. Astrophys. **36** (1998) 435;
S. S. Vogt, et al., Astron. J. **109** (1995) 151

[4] V. C. Rubin, N. Thonnard, & W. K. Jr. Ford, Astron. J. **87** (1982) 477

[5] P. Salucci & A. Borriello, Lect. Notes Phys. **616** (2003) 66

[6] X. X. Xue, et al., ApJ **684** (2008) 1143

[7] Y. Sofue, PASJ **64** (2012) 75

[8] P. Bhattacharjee, S. Chaudhury, & S. Kundu, ApJ **785** (2014) 63

[9] D. Clowe, et al., ApJ **648** (2006) L109

[10] G. Bertone, D. Hooper, & J. Silk, Phys. Rep. **405** (2005) 279

[11] G. Steigman & M. S. Turner, Nucl. Phys. B **253** (1985) 375

[12] D. Hooper & S. Profumo, Phys. Rep. **453** (2007) 29

[13] M. Drees, et al., PRD **63** (2001) 035008;
A. Bottino, et al., PRD **69** (2004) 037302

[14] H. C. Cheng, J. L. Feng, & K. T. Matchev, PRL **89** 211301 (2002)

[15] G. Jungman, M. Kamionkowski, & K. Griest, Phys. Rep. **267** (1996) 195

[16] M. E. Peskin, J. Phys. Soc. Jap. **76** (2007) 111017

[17] J. L. Feng, Ann. Rev. Astron. Astrophys. **48** (2010) 495

[18] M. Milgrom, ApJ **270** (1983) 365;
M. Milgrom, ApJ **270** (1983) 371;
M. Milgrom, ApJ **270** (1983) 384

[19] R. Scarpa, AIP Conf. Proc. **822** (2006) 253;
J. D. Bekenstein, Contemporary Physics **47** (2006) 387
M. Milgrom, *Israel Physical Society, IYA* (2009), **arXiv**: 0908.3842;
M. Milgrom, *Proceedings of Science PoS (HRMS)* 033 (2010), **arXiv**: 1101.5122

[20] M. W. Goodman & E. Witten, PRD **31** (1985) 3059

[21] O. Adriani, et al. [PAMELA Collaboration], PRL **111** (2013) 081102;
M. Ackermann, et al. [Fermi Collaboration], PRD **88** (2013) 082002;
M. Aguilar, et al. [AMS Collaboration], PRL **110** (2013) 141102;
A. Renshaw, **arXiv**: 1403.4575;
M. G. Aartsen et al., PRL **110** (2013) 131302

[22] Andrew C. Kobach, PRD **88** (2013) 116001;
Mads T. Frandsen, et al., JHEP **1207** (2012) 123;
G. Aad, et al., JHEP. **1304** (2013) 075

[23] L. E. Strigari, Phys. Rep. **531** (2013) 1

[24] C. Moni Bidin, et al., ApJ **751** (2012) 30

[25] J. Bovy & S. Tremaine, ApJ **756** (2012) 89

[26] S. Garbari , MNRAS **425** (2012) 1445

[27] M. C. Smith, S. H. Whiteoak, & N. W. Evans, ApJ **746** (2012) 181

[28] L. Zhang, et al., ApJ **772** (2013) 108

[29] J. Bovy & H.-W. Rix, ApJ **779** (2013) 115

[30] P. Salucci, F. Nesti, G. Gentile, & C. F. Martins, Astron. Astrophys. **523** (2010) 83

[31] R. Catena & P. Ullio, JCAP **08** (2010) 004

[32] M. Weber & W. de Boer, Astron. Astrophys. **509** (2010) 25

[33] F. Iocco et al., JCAP **11** (2011) 029

[34] P. J. McMillan, MNRAS **414** (2011) 2446

[35] J. Stadel, et al. [GHALO simulation], MNRAS **398** (2009) L21

[36] J. Diemand, et al. [Via Lactea simulation], Nature (London) **454** (2008) 735

[37] V. Springel, et al. [Aquarius simulation], MNRAS **391** (2008) 1685

[38] F. S. Ling, et al., JCAP **02** (2010) 012

[39] J. I. Read, et al. [Dark Disk Simulation], MNRAS **389** (2008) 1041

[40] J. D. Vergados, et al., PRD **77** (2008) 023509

[41] M. Lisanti, et al., PRD **83** (2011) 023519

[42] B. J. Kavanagh & A. M. Green, PRL **111** (2013) 031302

[43] J. Binney & S. Tremaine, *Galactic Dynamics*, 2nd Edition (Princeton University Press, Princeton, 2008)

[44] A. K. Drukier, K. Freese, & D. N. Spergel, PRD **33** (1986) 3495

[45] K. Freese, J. A. Frieman, & A. Gould, PRD **37** (1988) 3388

[46] C. Savage, G. Gelmini, P. Gondolo, & K. Freese, JCAP **04** (2009) 010

[47] A. M. Green, Mod. PLA **27** (2012) 1230004

[48] R. Cowsik, C. Ratnam, & P. Bhattacharjee, PRL **76** (1996) 3886;
*ibid* **78** (1997) 2262

[49] R. Cowsik, et al., New Astron. **12** (2007) 507

[50] L. P. Osipkov, Pisma Astron. Zh. **5** (1979) 77;
L. P. Osipkov, Soviet Astron. Lett. **5** (1979) 42;
D. Merritt, Astron. J. **90** (1985) 1027

[51] J. D. Lewin & R. F. Smith, Astropart. Phys. **6** (1996) 87

[52] F. J. Petriello & K. M. Zurek, JHEP **09** (2008) 047

[53] R. Bernabei, et al. [DAMA/LIBRA Phase 1], Eur. Phys. J. C **73** (2013) 2648

[54] C. E. Aalseth, et al. [CoGeNT Collaboration], PRL **106** (2011) 131301;
C. E. Aalseth, et al., PRL **107** (2011) 141301;
C. E. Aalseth, et al., PRD **88** (2013) 012002

[55] J. H. Davis, PRL **113** (2014) 081302

[56] D. Mihalas & J. Binney, *Galactic Astronomy* (Freeman, San Francisco, 1981)

[57] R. H. Helm, Phys. Rev. **104** (1956) 1466

[58] J. Engel, PLB **264** (1991) 114

[59] P. Gondolo, *XXXI Rencontres de Moriond: Dark Matter in Cosmology, Quantum Measurements, Experimental Gravitation*, Les Arcs, France, 1996, **arXiv**: hep-ph/9605290

[60] D. R. Tovey et al., PLB **488** (2000) 17

[61] P. Gondolo, et al., JCAP **07** (2004) 008

[62] V. Dimitrov, J. Engel, & S. Pittel PRD **51** (1995) 291

[63] M. T. Ressell et al., PRD **48** (1993) 5519

[64] J. Engel, M. T. Ressell, I. S. Towner, & W. E. Ormand, PRC **52** (1995) 2216

[65] M. T. Ressell & D. J. Dean, PRC **56** (1997) 535

[66] S. Archambault, et al. [PICASSO Collaboration], PLB **711** (2012) 153

[67] E. Behnke, et al. [COUPP Collaboration], PRD **86** (2012) 052001

[68] DAMA collaboration, R. Bernabei et al., Eur. Phys. J. C **56** (2008) 333

[69] R. Bernabei, et al., Riv. Nuovo Cim. **26N1** (2003) 1

[70] R. Bernabei, et al. [DAMA/LIBRA Phase 1], Eur. Phys. J. C **74** (2014) 2827

[71] G. Angloher, et al. [CRESST-II Collaboration], Eur. Phys. J. C **72** (2012) 1971

[72] R. Agnese, et al. [CDMS-II Collaboration], PRL **111** (2013) 251301

[73] Z. Ahmed, et al. [CDMS-II Collaboration], **arXiv**: 1203.1309

[74] D. Y. Akimov, et al. [ZEPLIN-III Collaboration], PLB **709** (2012) 14

[75] V. N. Lebedenko, et al. [ZEPLIN-III Collaboration], PRD **80** (2009) 052010

[76] E. Aprile, et al. [XENON-100 Collaboration], PRL **109** (2012) 181301

[77] E. Armengaud, et al. [EDELWEISS Collaboration], PLB **702** 2011 329;
E. Armengaud, et al. [EDELWEISS Collaboration], PRD **86** (2012) 051701

[78] M. Felizardo, et al. [SIMPLE Collaboration], PRL **108** 201302 (2012)

[79] E. Aprile, et al. [XENON-100 Collaboration], PRL **111** (2013) 021301

[80] D. S. Akerib, et al. [LUX Collaboration], PRL **112** (2014) 091303

[81] Z. Ahmed, et al. [CDMS Collaboration], Science **327** (2010) 1619

[82] D. Lynden-Bell, MNRAS **136** (1967) 101

[83] M. Honma & Y. Sofue, PASJ **49** (1997) 453

[84] J. Bovy, D. W. Hogg, & R. Hans-Walter, ApJ **704** (2009) 1704

[85] J. Caldwell & J. Ostriker, ApJ **251** (1981) 61;
K. Kuijken & G. Gilmore, MNRAS **239** (1989) 571;
ibid. **239** (1989) 605;

ibid. **239** (1989) 651;

ApJ **367** (1991) L9

[86] T. Naab & J. Ostriker, MNRAS **366** (2006) 899

[87] M. C. Smith, et al., MNRAS **379** (2007) 755

[88] D. S. Akerib, et al. [CDMS Collaboration], PRL **96** (2006) 011302

[89] G. Angloher, et al., Astropart. Phys. **18** (2002) 43

[90] J. Angle, et al. [XENON Collaboration], PRL **100** (2008) 021303

[91] J. Angle, et al. [XENON Collaboration], PRL **101** (2008) 091301

[92] A. Bottino, et al., PRD **78** (2008) 083520;

S. Chang, et al., PRD **79** (2009) 043513;

S. Chang, A. Pierce, & N. Weiner, PRD **79** (2009) 115011;

M. Fairbairn & T. Schwetz, JCAP **09** (2009) 037;

D. Hooper, et al., PRD **79** (2009) 015010;

S. Andreas, T. Hambye, & M. H. G. Tytgat, JCAP **10** (2008) 034

[93] E. M. Drobyshevski, Mod. Phys. Lett. A **23** (2008) 3077

[94] R. Bernabei, et al. [DAMA Collaboration], Eur. Phys. J. C **53** (2008) 205

[95] R. Foot, PRD **78** (2008) 043529

[96] R. Bernabei, et al. [DAMA Collaboration], Nucl. Instrum. Meth. A **592** (2008) 297

[97] S. Yellin, PRD **66** (2002) 032005;

S. Yellin, **arXiv**: 0709.2701

[98] Table 36.3 of Particle Physics Booklet released by Particle Data Group, 2012, *www.http://pdg.lbl.gov/*

[99] Z. Ahmed, et al. [CDMS collaboration], PRL **102** (2009) 011301

[100] J. K. Adelman-McCarthy, et al., ApJS **175** (2008) 297

[101] S. Chaudhury, P. Bhattacharjee, & R. Cowsik, JCAP **09** (2010) 020

[102] Y. Sofue & V. Rubin, Ann. Rev. of Astron. Astrophys. **39** (2001) 137

[103] V. Trimble, Ann. Rev. of Astron. Astrophys. **25** (1987) 425

[104] R. Cowsik, et al., New Astron. **12** (2007) 507

[105] B. Burch & R. Cowsik, ApJ **779** (2013) 35

[106] Y. Sofue, M. Honma, & T. Omodaka, PASJ **61** (2009) 227

[107] S. Gillessen, et al., ApJ, **692** (2009) 1075

[108] F. Nesti, & P. Salucci, JCAP **016** (2013) 1307

[109] R. Schönrich, J. Binney & W. Dehnen, MNRAS **403** (2010) 1829

[110] J. Binney & M. Merrifield, *Galactic Astronomy* (Princeton, NJ: Princeton Univ. Press, 1988)

[111] G. Westerhout, (1976) Maryland-Bonn Galactic 21-cm Line Survey, University of Maryland, College Park

[112] W. B. Burton & M. A. Gordon, Astron. Astrophys. **63** (1978) 7

[113] D. P. Clemens, ApJ, **295** (1985) 422

[114] M. Fich, L. Blitz & A. A. Stark, ApJ **342** (1989) 272

[115] J. Brand & L. Blitz, Astron. Astrophys. **275** (1993) 67

[116] F. Pont, M. Mayor, & G. Burki, Astron. Astrophys. **285** (1994) 415

[117] W. J. Maciel & L.G. Lago, Revista Mexicana de Astronomia y Astrofisica **41** (2005) 383

[118] W. J. Maciel, Astron. Astrophys. Supplement Series **55** (1984) 253

[119] S. Durand, A. Acker, & A. Zijlstra, Astron. Astrophys. Supplement Series **132** (1998) 13

[120] P. M. Frinchaboy & S. R. Majewski, Astron. J. **136** (2008) 118

[121] W. S. Dias, et al., Astron. Astrophys. **389** (2002) 871

[122] L. G. Hou, J. L. Han, & W. B. Shi, Astron. Astrophys. **499** (2009) 473

[123] J. S. Urquhart, et al., MNRAS **420** (2012) 1656

[124] S. Demers & P. Battinelli, Astron. Astrophys. **473** (2007) 143

[125] P. Battinelli, et al., Astrophysics **56** (2013) 68

[126] M. J. Reid, Ann. Rev. of Astron. Astrophys. **31** (1993) 345

[127] R. P. Olling & M. R. Merrifield, MNRAS **297** (1998) 943

[128] A. M. Ghez, et al., ApJ **689** (2008) 1044

[129] M. J. Reid, et al., ApJ **700** (2009) 137

[130] P. J. McMillan & J. Binney, MNRAS **402** (2010) 934

[131] Y. Sofue, et al., PASJ **63** (2011) 867

[132] A. Brunthaler, et al., Astron. Nach. **332** (2011) 461

[133] R. Schönrich, MNRAS **427** (2012) 274

[134] M. J. Reid & A. Brunthaler, ApJ **616** (2004) 872

[135] P. R. Bevington & D. K. Robinson, 2003, Data reduction and error analysis for the physical sciences, 3rd Ed. (New York, NY: McGraw-Hill)

[136] Susmita Kundu, Ph.D. thesis submitted to Homi Bhaba National Institute, Mumbai, India (2014)

[137] M. Perryman, et al., Astron. Astrophys. **369** (2001) 339;
L. Eyer, et al. (2013), *Proceedings of the XIth Hvar Astrophysical Colloquium*, **arXiv**: 1303.0303

[138] J. C. Kapteyn, ApJ. **55** (1922) 302 [1]

[139] J. H. Jeans, MNRAS **82** (1922) 122

[140] J. H. Oort, Bull. Astron. Inst. Netherlands **6** (1932) 249

[141] E. R. Hill, Bull. Astron. Inst. Netherlands **15** (1960) 1

[142] J. H. Oort, Bull. Astron. Inst. Netherlands **15** (1960) 45

[143] J. N. Bahcall, ApJ **287** (1984) 926

[144] O. Bienayme, A. C. Robin, & M. Creze, Astron. Astrophys. **180** (1987) 94

[145] K. Kuijken & G. Gilmore, ApJ **367** (1991) L9

[146] J. N. Bahcall, C. Flynn, & A. Gould, ApJ **389** (1992) 234

[1] All Journal References are in order: Journal name **Volume** (Year) Starting Page Number

[147] M. Creze, et al., Astron. Astrophys. **329** (1998) 920

[148] Holmberg J., Flynn C., MNRAS **313** (2000) 209

[149] Holmberg J., Flynn C., MNRAS **352** (2004) 440

[150] O. Bienayme, et al., Astron. Astrophys. **446** (2006) 933

[151] J. I. Read, J. Phys. G **41** (2014) 063101

[152] A. Putze, L. Derome, D. Maurin, L. Perotto, & R. Taillet, Astron. Astrophys. **497** (2009) 991;
A. Heavens, **arXiv**: 0906.0664

[153] F. Hammer, et al., ApJ **662** (2007) 322

[154] J. F. Navarro, C. S. Frenk, & S. D. M. White, MNRAS **275** (1995) 720

[155] J. F. Navarro, C. S. Frenk, & S. D. M. White, ApJ **462** (1996) 563

[156] J.F. Navarro, C.S. Frenk, & S. D. M. White, ApJ **490** (1997) 493

[157] L. Hernquist, ApJ **356** (1990) 359

[158] L. Hernquist, ApJS **86** (1993) 389

[159] J. F. Navarro et al., MNRAS **349** (2004) 1039

[160] A. W. Graham, et al., Astron. J. **132** (2006) 2701

[161] J. F. Navarro et al., MNRAS **402** (2010) 21

[162] A. Burkert, ApJ **447** (1995) L25.

[163] N. Metropolis, et al., J. Chem. Phys. **21** (1953) 1087

[164] W. K. Hastings, Biometrika **57** (1970) 97

[165] *http://cosmologist.info/cosmomc/*

[166] Y. Y. Mao, et al., ApJ **764** (2013) 35

[167] A. S. Eddington, MNRAS **76** (1916) 572

[168] P. Bhattacharjee, S. Chaudhury, S. Kundu, & S. Majumdar, PRD **87** (2013) 083525

[169] L. Ciotti & S. Pellegrini, MNRAS **255** (1992) 561

[170] A. Meza & N. Zamorano, ApJ **490** (1997) 136

[171] L. M. Widrow, ApJS **131** (2000) 39

[172] P. Ullio & M. Kamionkowski, JHEP **03** (2001) 049

[173] R. Catena, JCAP **05** (2012) 005

[174] N. Bozorgnia, R. Catena, & T. Schwetz, JCAP, **12** (2013) 050

[175] P. Cuddeford, MNRAS **253** (1991) 414

[176] L. Ciotti & L. Morganti, MNRAS **401** (2010) 1091

[177] E. V. Hese , M. Baes, & H. Dejhonge, ApJ **690** (2009) 1280

[178] M. Fornasa & A. Green, PRD **89** (2014) 063531

[179] R. Wojtak, et al., MNRAS **388** (2008) 815